The Pennsylvania State University

The Graduate School

MICROFLUIDIC MOLECULAR AND CELLULAR DETECTION OF MALARIA TOWARDS ELIMINATION

A Dissertation in

Electrical Engineering

by

Gihoon Choi

© 2020 by Gihoon Choi

Submitted in Partial Fulfillment
of the Requirements
for the Degree of

Doctor of Philosophy

August 2020

The dissertation of Gihoon Choi was reviewed and approved by the following:

Weihua Guan

Assistant Professor of Electrical Engineering

Dissertation Advisor

Chair of Committee

Aida Ebrahimi

Assistant Professor of Electrical Engineering

Zhiwen Liu

Professor of Electrical Engineering

Pak Kin Wong

Professor of Biomedical Engineering

Kultegin Aydin

Professor of Electrical Engineering

Head of the Department of Electrical Engineering

ABSTRACT

Malaria is a mosquito-borne disease caused by *Plasmodium* parasites, predominately in resource-limiting areas. With the significant progress in malaria controls during the past decade, WHO endorsed the ambitious goal of achieving malaria elimination. Since low-level malaria infection is highly distributed in the elimination-phase countries, the elimination strategy involves (1) identification of asymptomatic carriers to reduce the parasite reservoir and (2) interruption of the malaria transmission vector.

The work presents the microfluidic tools that facilitate point-of-care nucleic acid testing (NAT) and cell mechanotyping (*i.e.*, label-free cell deformability sensor and deformability-activated cell sorting) towards the malaria elimination. While point-of-care NAT opens up extensive remote diagnostic opportunities in resource-limited regions, cell mechanotyping can be used to explore the underlying mechanism of the transmission vector.

The thesis will describe the single- and quad-plex point-of-care NAT systems, which deliver highly sensitive molecular answers within 40 minutes from raw whole blood samples. Scalable parasite DNA sample preparation and subsequent real-time loop-mediate isothermal amplification (LAMP) were seamlessly integrated on a single microfluidic reagent compact disc. The combination of the sensitivity, specificity, cost, and scalable sample preparation suggests effective and accurate malaria screening in the field.

To provide tools for a microfluidic cell mechanotyping study, we developed a constriction-based cell deformability sensor. Cell deformability is an excellent label-free biomarker for cell abnormalities. The sensor indirectly measures the cell deformability by probing the transit time during cell translocation events at micro-constriction. We successfully evaluated the sensor

performance by achieving the high-throughput parasitemia measurement and parasite stage determination and demonstrated cell deformability is an excellent label-free biomarker for malaria infection. Using this biophysical marker, we demonstrated a single-cell-resolved, cytometry-like deformability-activated cell sorting in the continuous flow to enrich the gametocytes from the crude blood samples. Finally, we demonstrated the constriction-based multichannel resistive pulse sensor, integrated with time-division multiplexing accessing (TDMA) methodology to further improve deformability measurement and deformability-activated sorting throughput with maintaining the scalability.

We envision that point-of-care NAT and microfluidic cell mechanotyping devices will provide early and accurate malaria screening in the field and in-depth of understanding of overall malaria pathophysiology and underlying mechanism of the malaria transmission vector.

TABLE OF CONTENTS

LIST OF FIGURES

LIST OF TABLES

ACKNOWLEDGEMENTS

First of all, I would like to express my sincere gratitude to my research advisor, Dr. Weihua Guan, for allowing me to conduct research and providing priceless guidance throughout my Ph.D. program. He has taught me the methodology to carry out the research and to present the research works as clearly as possible. It was a great privilege and honor to work and study under his guidance as his first Ph.D. student. I am incredibly thankful for what he has offered me.

For this dissertation, I would like to thank my defense committee members: Dr. Zhewen Liu, Dr. Aida Ebrahimi, and Dr. Pak Kin Wong for their time, guidance, and constructive comments. I also would like to acknowledge Dr. Liwang Cui, Dr. Jun Miao, Dr. Sony Shrestha, and Xiaolian Li in the department of entomology for sharing their knowledge and skills, that are required for malaria-related research. I have appreciated their collaboration. In regards to the hydrogel bead fabrication, I thank Dr. Lauren Zarzar, who shared her knowledge and helpful tips.

The work presented in this dissertation was supported in part by the National Institutes of Health (NIH) under Grant U19AI089672 and National Science Foundation (NSF) under grant No. ECCS-171083, 1710831, 1902503, and 1912410. Also, Penn State Award 'Materials Matter at the Human Level' was also acknowledged. The views and opinions of the author expressed herein do not state or reflect those of federal fundings, and shall not be used for advertising or product endorsement purposes.

Finally, I am incredibly grateful to my family for their love, prayers, caring, and sacrifices. I am very much thankful to my wife, Jina, for her love, understanding, prayers, and continuing support to complete this research work.

Gihoon Choi

Chapter 1 Introduction and Overview

1.1. Background

Malaria is a mosquito-borne disease caused by *Plasmodium* parasites, predominately in resource-limiting areas of low- and middle-income countries. According to the World Health Organization (WHO), there were 216 million new cases, and 445,000 deaths in 2016 and approximately 2.7 billion people remain at risk globally, with most of the disease burden falling on resource-constrained countries in Africa and sub-Saharan Africa [20]. Among five parasite species, *P. falciparum* (*Pf*) and *P. vivax* (*Pv*) pose the greatest threat to the human. *Pf* is the most prevalent malaria parasite on the African continent. *Pv* is the dominant malaria parasite in most countries outside of sub-Saharan Africa. Increased malaria control efforts have resulted in a dramatic reduction (40%) in the global malaria incidence over the past decade [20]. The WHO thus endorsed the ambitious goal of achieving worldwide malaria elimination and eradication [20].

Malaria is caused by the infection of protozoan parasites of the *Plasmodium* species. During the malaria life cycle, parasites invade red blood cells (RBCs) and undergo asexual replication. This proliferation phase leads to a significant fraction of infected RBCs, which is the primary cause of the pathology of malaria. Therefore, accurate and timely diagnosis and antimalarial treatment can deter parasite growth and proliferation. After the asexual stage, only a small percentage of parasites undergo sexual conversion to form gametocytes. Therefore, the detection of circulating gametocytes in the bloodstream is quite challenging [21]. Although gametocytes do not cause any clinical symptoms, they are responsible for malaria transmission to the mosquito [22, 23].

Consequently, the restriction of gametocyte maturation provides unique opportunities for malaria intervention [23].

The low-level malaria infection is highly distributed in the malaria elimination-phase countries (low prevalence setting) [20, 21]; thus, the malaria elimination strategy involves (1) identification and treatment of asymptomatic carriers to reduce the parasite reservoir and (2) interruption of the malaria transmission. To this end, the effectiveness of elimination strategies highly depends on low-cost access to sensitive and specific malaria screening tests. More specifically, diagnostic devices require detection limit lower than 2 parasites/μl for identifying asymptomatic carriers and sexual stage gametocytes [20, 21]. However, current field-deployable technologies are limited to achieve this level of sensitivity [24-26]. Besides, the underlying mechanism of the transmission vector is unclear yet due to the rarity of gametocytes in the bloodstream [21, 23].

This thesis mainly focuses on microfluidic technologies that can resolve the aforementioned unmet requirements and expedite the global efforts towards malaria elimination. The main contribution of this thesis is as follows.

First, we provide a point-of-care nucleic acid testing (NAT) device to bring highly sensitive malaria diagnosis to the field. While NAT has been extensively used for identifying low-level infection, it is often inaccessible in remote settings due to the complicated steps of the nucleic acid sample process. To bring the nucleic acid testing to the field, we integrated an energy-efficient magnetic interaction-based streamlined sample process on a lab-on-a-disc platform. Unprecedently integrated system has attributes of excellent sensitivity, specificity, cost, and scalability, suggesting a useful and accurate detection of asymptomatic carriers in the field.

Second, we offer microfluidic cell mechanotyping tools (*i.e.*, cell deformability sensor, and deformability-activated cell sorting), which enable careful study on the pathophysiology of

malaria-infected red blood cells. We demonstrated that the cell deformability could be used as a potential label-free biomarker to probe cell abnormalities and infection status. The transit time-based cell deformability measurement facilitates rapid parasitemia analysis and parasite stage determination. We also demonstrated the single-cell-resolved, cytometry-like deformability-activated sorting (DACS) in the continuous flow to enrich the cells of a particular deformability property from a heterogeneous sample. We envision that the DACS device will allow enriching gametocytes based on their mechanical biomarker. Furthermore, it will promote biologists to understand the underlying mechanism of the malaria transmission vector.

1.2. Overview of work presented

The first part of the thesis (Chapter 2 and Chapter 3) discusses the efforts to develop a fully integrated "sample-to-answer" mobile NAT platform for highly sensitive and specific malaria diagnosis in the field. Chapter 2 describes the initial version of the NAT platform as a proof-of-concept. The novel strategy for the streamlined sample process, including nucleic acid extraction, purification, amplification, and real-time fluorescence detection is discussed. It is demonstrated that the system has a superior detection limit with whole blood samples. This is promising for identifying asymptomatic carriers in the field. Chapter 3 describes the 4-plex NAT device that can perform species-specific tests in parallel. The system is particularly useful for tracking malaria transmission profile and their species. The second part of the work (Chapter 4 to Chapter 6) discusses the efforts to provide microfluidic cell mechanotyping tools to explore the underlying mechanism of malaria diseases and progression. Chapter 4 presents a rapid and label-free microfluidic cell deformability sensor. The device uses cell deformability as a promising label-free biomarker to quantify parasitemia and to differentiate the parasite development stage in the bloodstream. Chapter 5 describes the "first-of-its-kind" microfluidic Deformability-Activated Cell

Sorting (DACS) device to collect the cells of interest based on their biophysical properties. One of the grand challenges of a constriction-based cell deformability sensor is channel clogging. Besides, we have explored that speed of cell deformability characterization is a rate-limiting factor for the high-throughput deformability-activated cell sorting. Chapter 6 presents a novel scalable Time-Division Multiplexing Accessing (TDMA) microfluidic deformability sensor array as a solution to address the rate-limiting factor for high-throughput deformability-activated cell sorting. Finally, Chapter 7 offers conclusions based on the work presented in the preceding chapters and perspectives for future development.

Chapter 2 Singleplex Highly Sensitive and Field-deployable Malaria Nucleic Acid Testing for Low-density Detection

In this chapter, we demonstrated a standalone, "sample-in-answer-out" molecular diagnostic system (AnyMDx) to enable a highly sensitive and quantitative molecular analysis of blood-born malaria in low resource areas. The system consists of a durable battery-powered analyzer and a disposable microfluidic compact cartridge loaded with reagents ready for use. A low power thermal module and a novel fluorescence-sensing module are integrated into the analyzer for real-time monitoring of loop-mediated isothermal nucleic acid amplification (LAMP) of target parasite DNA. With 10 µl of a raw blood sample, the AnyMDx system automates the nucleic acid sample preparation and subsequent LAMP and real-time detection. Under the laboratory conditions with whole-blood samples spiked with cultured *Plasmodium falciparum*, we achieved a detection limit of ~0.6 parasites/µl, much lower than those for the conventional microscopy and rapid diagnostic tests (~50-100 parasites/µl). The turnaround time from the sample to the answer is less than 40 minutes. The AnyMDx is user-friendly, requiring minimal technological training. The analyzer and the disposable reagent cartridge are cost-effective, making AnyMDx a potential tool for malaria molecular diagnosis under field settings for malaria elimination.

2.1. Introduction to point-of-care nucleic acid testing

Toward effective malaria control, rapid, accurate, and highly sensitive diagnosis is essential for delivering effective chemotherapies. Currently, malaria diagnosis under field settings relies exclusively on traditional microscopy (thin and thick blood smears) and immunological rapid diagnostic tests (RDTs, detecting antigens in human blood) with a detection limit of 50 – 100 parasites/μL [25, 27, 28]. Such a detection limit would inevitably miss malaria cases with much lower parasitemias, which are especially common in asymptomatic parasite carriers [29-32]. Thus, malaria diagnostic tools with significantly improved sensitivity are urgently needed for endemic settings, especially for regions planning for malaria elimination.

Modern nucleic acid testing (NAT) methods of malaria detection enable much higher sensitivity with a detection limit of <1 parasite/μL depending on the assay type [28, 31, 33-35], which is highly desirable for identifying asymptomatic infections [27, 31, 36]. Sensitive detections of malaria parasites in these subpopulations, which are considered as essential reservoirs of transmission, are particularly important for malaria elimination [31, 37]. Among various molecular amplification assays (recombinase polymerase amplification [38, 39], helicase dependent amplification [40]), loop-mediated isothermal DNA amplification (LAMP) has emerged as a promising technology for field use due to its simplicity, rapidness, sensitivity, and specificity [28, 41-54]. The major advantages of using LAMP include its high specificity, robustness against inhibitors, and fast amplification [55-57]. Unfortunately, most LAMP-based diagnosis still involves bulky and costly peripheral equipment, and skilled technicians are often required for manually operating the instrument [28, 58] and performing multiple steps of sample preparation [59-62]. Moreover, necessary infrastructures such as electricity for powering instruments are often limited in remote malaria clinical settings [63-65]. Therefore, there is a strong desire to develop a molecular diagnostic system that can be more easily deployed to remote malaria-endemic areas. Although

extensive efforts have been undertaken towards this goal [66, 67], a true "sample-in-answer-out" NAT system with real-time quantitative capability has yet to be developed.

A field-deployable molecular malaria diagnostic platform should possess the following attributes: i) standalone and portable for field applications; ii) true sample-in-answer-out without much user intervention; iii) seamlessly integrated and automated DNA sample preparation, iv) real-time quantitative fluorescence detection; v) rapid and suitable for diagnosis in clinical settings, and vi) much higher sensitivity allowing detection at low parasitemias.

Here we report the design of a molecular diagnostic system for malaria, named AnyMDx, which consists of a small-footprint analyzer and disposable microfluidic compact cartridge that are preloaded with molecular reagents for the LAMP assay. With minimal manual work, the AnyMDx could deliver sensitive molecular diagnostic results directly from a small volume of blood samples within 40 minutes without any requirement of laboratory infrastructures. The standalone and user-friendly AnyMDx instrument is highly promising for sensitive malaria diagnosis in field settings.

2.2. Loop-mediated isotherm amplification assay development

2.2.1. LAMP master mix

The LAMP reaction mix consists of isothermal buffer (20 mM Tris-HCl, 10 mM $(NH_4)_2SO_4$, 50 mM KCl, 2 mM $MgSO_4$, 0.1% Tween 20, pH 8.8), species-specific primer set (5 pmol F3 and B3, 40 pmol FIP and BIP, 20 pmol LF and LB, Table 2-1), $MgSO_4$, calcein, MnCl2, deoxyribonucleotide triphosphates (dNTPs), Bst 2.0 DNA polymerase, DNA template, and PCR grade H_2O (Table 2-2). The LAMP assay was performed at a constant temperature (65°C maintained by the analyzer) (see Figure 2-8). Six target-specific primers targeting the mitochondrial

gene were synthesized (Integrated DNA Technologies) to specifically amplify the 213-bp region of the *P. falciparum* DNA (Figure 2-1 and Table 2-1) [68, 69]. For pan-*Plasmodium* detection, we adopted a primer set targeting the mitochondrial gene common to all *Plasmodium* species [68]. For *Pv*-specific detection, we used a primer set targeting the *cox1* gene of *Pv* [70]. All primer sets were listed in Table 2-1. It is noteworthy the *Pv* primers used here could also cross-react with *P. knowlesi* species [70]. The primer set we used in this study is the same as those reported previously [68] [70].

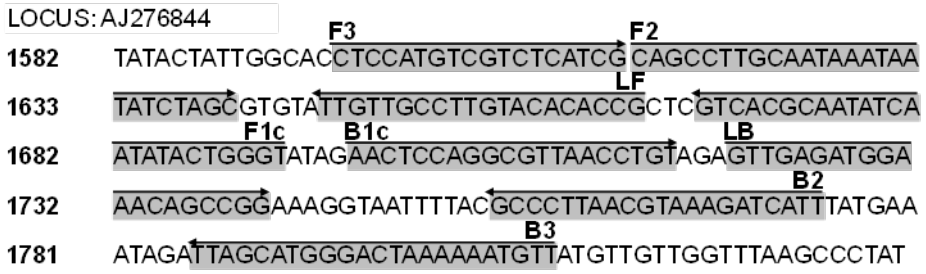

Figure 2-1: Location of the LAMP target sequence and priming sites of *Plasmodium falciparum* (*Pf*: Genbank accession no. AJ276844). The core priming sites of inner/outer primers (F3/B3, F2/B2, and F1c/B1c) with additional priming sites of loop primers (LF/LB) are marked on the sequence.

Table 2-1: Primer sets for the genus-, *P. falciparum*-, and *P. vivax*-specific LAMP amplification

Species	**Primer**	**Sequence (5' → 3')**
	F3	TCGCTTCTAACGGTGAACT
	B3c	AATTGATAGTATCAGCTATCCATAG
Plasmodium genus	FIP (F1c – F2)	GGTGGAACACATTGTTTCATTTGATCTCATTCCAATGGAACCTTG
[68]	BIP (B1 – B2c)	GTTTGCTTCTAACATTCCACTTGCCCGTTTTGACCGGTCATT
	LF	CACTATACCTTACCAATCTATTTGAACTTG
	LB	TGGACGTAACCTCCAGGC

	F3	CTCCATGTCGTCTCATCGC
	B3c	AACATTTTTTAGTCCCATGCTAA
P. falciparum	FIP (F1c – F2)	ACCCAGTATATTGATATTGCGTGACAGCCTTGCAATAAATAATATCTAGC
[68]	BIP (B1 – B2c)	AACTCCAGGCGTTAACCTGTAATGATCTTTACGTTAAGGGC
	LF	CGGTGTGTACAAGGCAACAA
	LB	GTTGAGATGGAAACAGCCGG
	F3	GGTACTGGATGGACTTTATAT
	B3c	GGTAATGTTAATAATAGCATTACAG
P. vivax	FIP (F1c – F2)	CCAGATACTAAAAGACCAACCCACCATTAAGTACATCACT
[70]	BIP (B1 – B2c)	GCTAGTATTATGTCTTCTTTCACTTAATATACCAAGTGTTAAACC
	LF	GATAACATCTACTGCAACAGG
	LB	CTACTGTAATGCATCTAAGATC

Table 2-2: Reagent setup of the LAMP master mix.

Component	**Concentration**	**Volume**
PCR grade water	1 x	7.25 µl
Primer sets	-	6.50 µl
Isothermal buffer	1 x	2.50 µl
$MgSO_4$	7.00 mM	1.75 µl
Calcein	25.00 µM	0.63 µl
$MnCl_2$	0.75 mM	1.88 µl
dNTP mix	1.40 mM	3.50 µl
Bst DNA polymerase	0.32 Unit/µl	1.00 µl

2.2.2. Validation of LAMP assays for *P. falciparum*, *P. vivax*, and pan-*plasmodium*

To validate the LAMP primer sets for specifically detecting *Pf*, *Pv,* and pan-*Plasmodium*, we performed a cross-reactivity test using extracted *Pf* and *Pv* genomic DNA on a benchtop real-time PCR instrument (Bio-Rad CFX96). *Pf* genomic DNA is obtained from *P. falciparum* cultured blood sample. *Pv*-infected blood samples were obtained from BEI Resources Repository (MRA-369 *Pv* strain Achiote, and MRA-383 *Pv* strain Chesson). Each analysis was performed with triplicates. As shown in Figure 2-2A, *P. falciparum*- and *P. vivax*- specific assays can pick up the corresponding genomic sample specifically without cross-reactivity. In contrast, the pan-*Plasmodium* assays can pick up any *Plasmodium* species (*P. falciparum* and *P. vivax*). No amplification was observed with the negative control (PCR grade water). We performed gel electrophoresis in 2% agarose gel to further evaluate each amplicon (Figure 2-2B). A clear ladder-like pattern with multiple bands of different molecular sizes was observed due to the stem-loop DNA structures with several inverted repeats within LAMP amplicons [71]. The length of the bands showed confirmative agreement with the length of the target sequence (213-, 127-, and 220-bp bands were expected from *P. falciparum*, *P. vivax*, and pan-*Plasmodium* products respectively) [68].

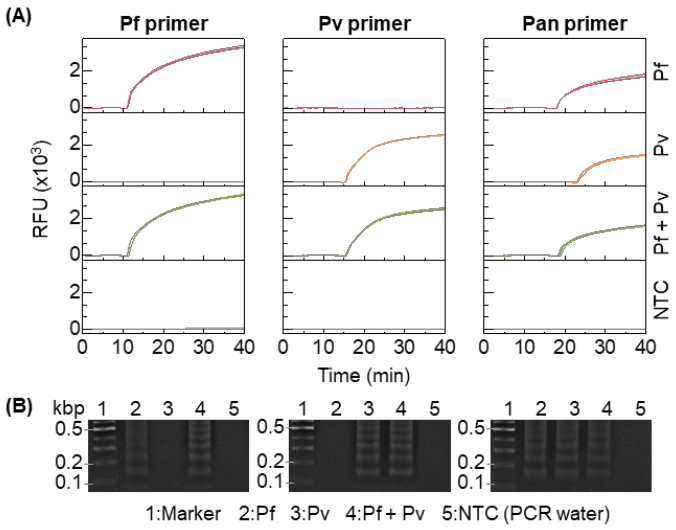

Figure 2-2: Validation of the species- and genus-specific LAMP assays using laboratory purified *Pf* and *Pv* genomic DNA. (A) Amplification curves obtained from real-time PCR. PCR grade water was used as a no template control (NTC). (B) Gel electrophoresis image (2% agarose gel). Ladder-like bands in the gel image confirm the amplicons from species- and genus-specific LAMP reactions.

2.2.3. Thermostability of LAMP reagents

Although most of our experiments used liquid phase reagents loaded into the disc immediately before use, the reagents could also be preloaded before use. We studied the thermostability of LAMP reagents (especially *Bst* 2.0 DNA polymerase) when stored at 25 ºC (ambient temperature) and at 4 ºC (refrigerator temperature) to evaluate their applicability for field use. During a week-long test, LAMP reagents stored at 25 ºC and 4 ºC were assessed every 24 hours to detect the model *Pf* genomic DNA. These experiments were done in 3 repetitions. As shown in Figure 2-3, the enzymes and reagents were found to retain sufficient activity to achieve successful DNA amplification when stored at 4°C for a week. There was no significant shift in the average threshold time for reagents stored at 4°C for one week. In contrast, when stored at 25 ºC, although the

enzymes and reagents were active and could efficiently amplify DNA in less than 50 min for 3 days (no activity afterward), the threshold time (T_t) needed to obtain the positive/negative results were delayed (Figure 2-3B). These results indicate that a qualitative yes/no amplification could be achievable for reagents storage at room temperature. However, for a consistent real-time quantitative LAMP detection, cold-chain transport and storage of the prefilled microfluidic reagent disc would be preferred. The stability issue could also be addressed by using reagent lyophilization. It was found the lyophilized reagents could remain stable for 24 months when stored at 4 °C, 28 days at 25 °C, and 2 days at 37 °C [72].

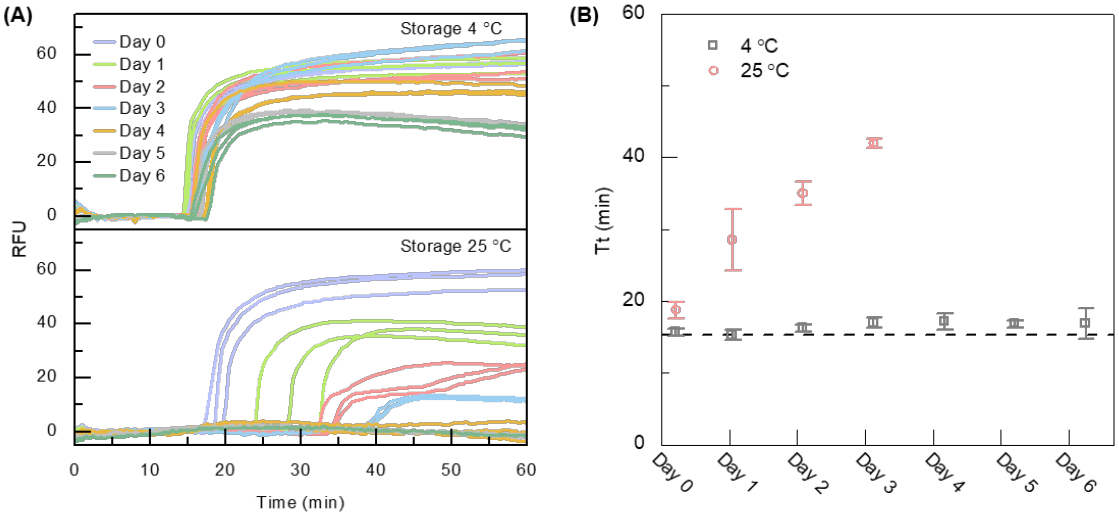

Figure 2-3: LAMP reagent thermostability test. (A) The real-time amplification curve for LAMP reagent stored at 4 °C and 25 °C. (B) Extracted amplification threshold time (T_t). At 4 °C storage temperature, the reagent shows a negligible threshold time drift for a week. At 25 °C storage, the reagent shows a drift towards higher T_t (decreased activity) over time, and no amplification is seen after day 3. The dashed line denotes the freshly prepared LAMP reagent.

2.3. Charge-switchable magnetic bead-based parasite DNA preparation

The common challenges for most point-of-care nucleic acid testing device stemmed from high-quality and scalable nucleic acid sample preparation. In our preliminary study, we explored charge switchable magnetic bead-based method for DNA extraction (Figure 2-4). We first performed a reference experiment to confirm compatibility of ChargeSwitch forensic DNA extraction/purification kit in the tube. Since the surface charge polarity of the magnetic beads is pH dependent, and the surface charge polarity of DNA is negative for a wide range of pH values, the magnetic beads can attract or repel the nucleic acids by the different pH values of the preloaded buffer solution (Figure 2-4B).

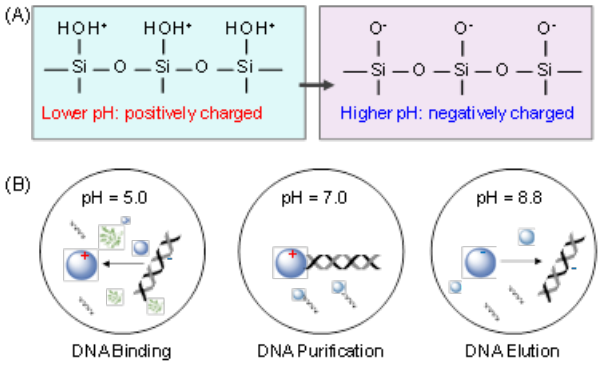

Figure 2-4: Charge switchable magnetic bead-based method for DNA isolation. (A) pH switchable surface charge of silanol groups at silica surface. (B) DNA binding, purification and elution process on silica surface can be actuated by surrounding pH values.

2.4. Singleplex instrumentation integration

2.4.1. Analyzer

The assembled and exploded views of the AnyMDx system are shown in Figure 2-5. The instrument was designed in SolidWorks and can be quickly prototyped in-house with a 3D printer. The whole system is of a small footprint (12×13×13 cm). It is powered by a rechargeable lithium-ion battery allowing for 14 hours of continuous operation before recharging. The functional modules inside the AnyMDx system are illustrated in the block diagram (Figure 2-6).

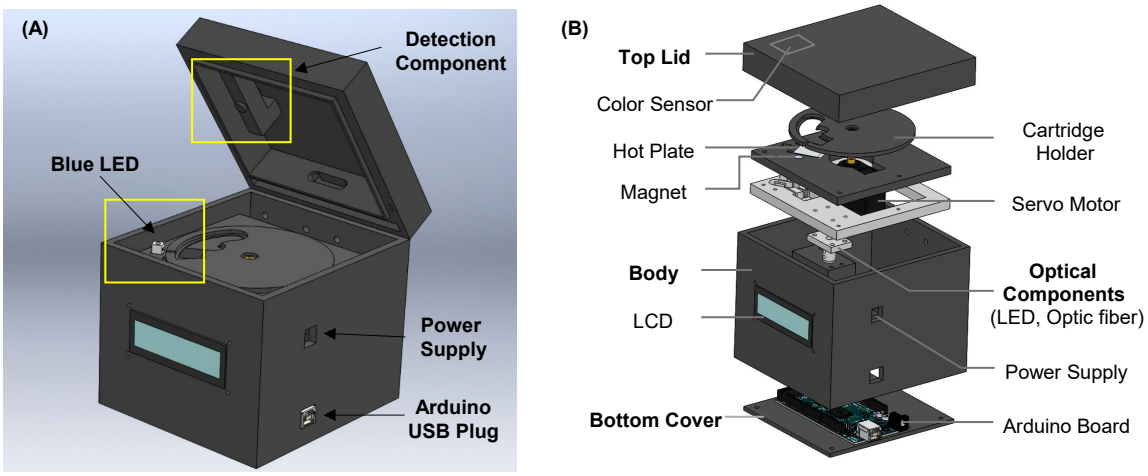

Figure 2-5: Overview of the standalone and mobile nucleic acid testing system (AnyMDx). (A) Schematic diagram of the assembled AnyMDx with the reagent compact cartridge. The whole platform is of a small footprint (12×13×13 cm). The reagent compact cartridge was secured on the rotatable spindle platter. (B) Schematic diagram of functional parts in an exploded view.

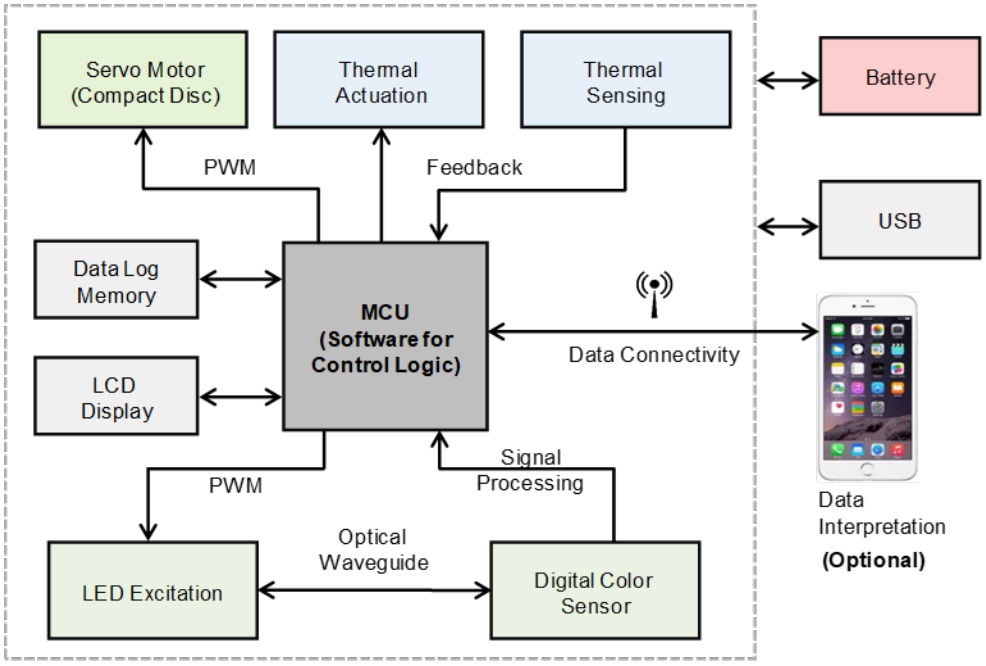

Figure 2-6**:** Block diagram of the AnyMDx modules. The platform consists of four main functional modules: mechanical modules (servo motor/spindle platter/compact cartridge), optical modules (LED/optical sensor), thermal modules (Peltier heater/thermal sensor), and data connectivity modules (Bluetooth). Each module was controlled by a microprocessor on a customized PCB board. The diagnostic results can be optionally reported to a smartphone user interface.

Real-time optical subsystem. On the excitation side, the LED light source (λ= 488 nm, C503B-BCN-CV0Z0461, Newark) was guided towards the reaction chamber through a polymer optical fiber (#02-538, Edmund). The optical fiber and LED were self-aligned by a customized adapter to achieve optimal light coupling efficiency. On the detection side, the emission light from the LAMP reaction chamber was coupled to the optical sensor (TCS34725, Digi-Key) by the optical fiber. The incidence of the excitation LED light is perpendicular to the optical sensor to minimize the diffracted excitation light into the optical sensor and thus increasing the signal-to-noise ratio. During the amplification process, the fluorescence readings were acquired every 2.5 seconds. The first 5 min of the signal was averaged to obtain the background noise level, which was then subtracted from the raw fluorescence readings to form a processed signal. The processed signal was further smoothed by averaging a fixed number of consecutive data points. We defined a threshold

time (T_t) at the time when the slope of measured RFU (d*RFU*/d*t*) reached the peak (Figure 2-7). The threshold RFU value was experimentally determined at 400 for positive/negative decision.

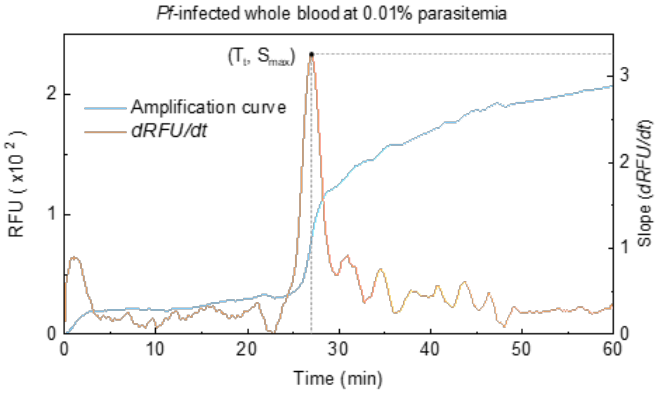

Figure 2-7: Determination of the threshold time (T_t). A real-time amplification curve (blue) and its differential profile (*dRFU/dt*, orange). The threshold time (T_t) was determined at the maximum slope of RFU. (T_t: threshold time, t: time, S_{max}: maximum value of the slope)

Thermal subsystem. For the feedback thermal control system, a Peltier heater was bonded to the backside of the aluminum heating plate by thermal paste. A micro-thermistor was embedded inside of the aluminum heating plate for real-time temperature monitoring. The desired reaction temperature was maintained by the feedback control during the DNA amplification process to maintain a desired constant temperature. To evaluate the temperature fluctuation, the temperature was monitored for 60 minutes by an external independent thermocouple module (NI-9211, National Instruments). Figure 2-8 shows the temperature on the aluminum heating plate can reach the set temperature (65 °C) within 40 seconds and continuously maintain a temperature between 64.5 °C to 66.5°C.

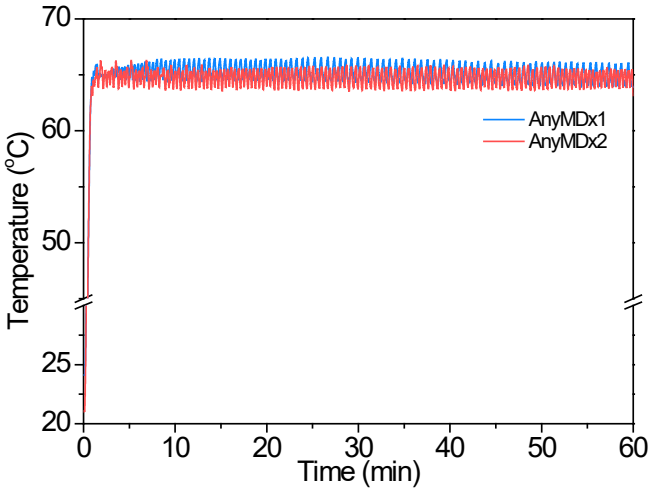

Figure 2-8: The feedback-controlled reaction temperature profiles as a function of time. (blue curve: AnyMDx 1, red curve: AnyMDx 2)

Mechanical and interfacing subsystems. An embedded microcontroller unit (MCU) operates the whole system to perform all necessary isothermal assay steps, including automated sample preparation, nucleic acid amplification, and real-time detection. An LCD provides a user-friendly interface for instrument status and data display. Besides, a low power Bluetooth module was incorporated for easy data connectivity.

2.4.2. Microfluidic reagent compact cartridge design and fabrication

The microfluidic compact cartridge consists of the top (0.8 mm thick), spacer (1.6 mm thick), and bottom (0.8 mm thick) poly (methyl methacrylate) (PMMA) layers laminated with adhesive solvent (Figure 2-9). Each layer was designed in AutoCAD (diameter of 9.6 cm) and patterned by a CO_2 laser cutter (Epilog Helix 24 Laser System) with a power of 100%, a speed of 30% (for the top/bottom of 0.8 mm thick) and 60% (for the spacer of 0.8 mm thick), and a frequency of 5000 Hz. The patterned top, spacer, and bottom polymethyl methacrylate (PMMA) layers were initially

washed with detergent to remove residues from laser cutting, then laminated with adhesive solvent. The assembled cartridge was cleaned twice with 2% sodium hypochlorite (NaOCl) and distilled water, respectively, to eliminate inhibitory substances, which could cause chemical interference.

Each assembled cartridge accommodates three independent testing units. Each unit consists of five chambers: a DNA binding chamber (with an inlet for sample input), a washing chamber, a reaction chamber, and two valving chambers (Figure 2-9). The valving chambers were filled with FC-40 oil or air. The FC-40 oil, which seals the LAMP reaction chamber, helped prevent master mix evaporation during the thermal process. The air-filled valve was surface treated with water-oil repellent to create a barrier for the amphiphilic lysis buffer. The inlets for sample input were sealed by pressure-sensitive adhesive (PSA) tapes (3M Scotch 3650).

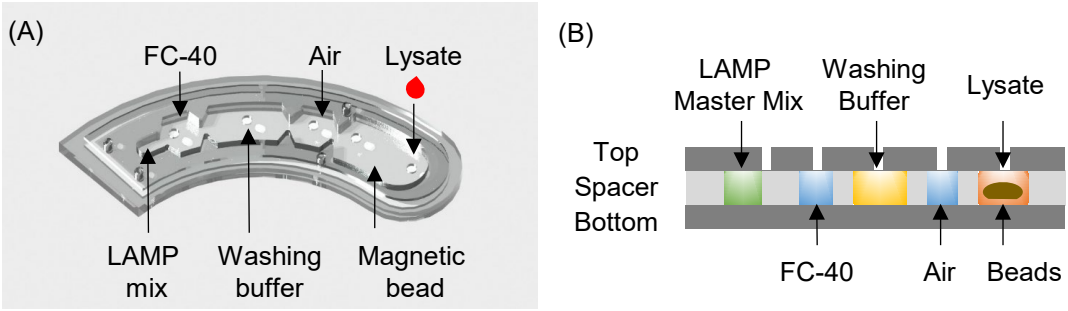

Figure 2-9: Illustration of reagent compact cartridge. (A) Assembled view of the reagent cartridge. A test unit consists of five chambers: a DNA binding chamber (binding buffer pH 5.0), a washing chamber (washing buffer pH 7.0), a LAMP reaction chamber (master mix, pH 8.8), and two valving chambers. The lysate was prepared by collecting 10 µl of malaria-infected blood into 1 ml of lysis buffer in a microcentrifuge tube. (B) Cross-sectional view of the reagent cartridge showing. All reagents are preloaded on the reagent cartridge in a ready-to-use format.

2.5. Working principle of streamlined DNA sample preparation on the cartridge

We used a commercially available DNA purification kit (Invitrogen ChargeSwitch® forensic DNA purification kit) for isolating *P. falciparum* DNA from whole blood lysates. The lysis buffer, binding buffer, and washing buffer were used as received. The LAMP master mix was prepared before running the experiments. All reagents were in the liquid phase when loaded onto the cartridge. The reagents-loaded cartridge was stored in the fridge at 4°C. The reagents were stable for at least 3 days under this storage condition. The 10 µl of human whole blood samples spiked with cultured *P. falciparum* were collected into a 1.5 ml microcentrifuge tube containing 1000 µl of lysis buffer and 10 µl proteinase K. After incubating at room temperature for 2 min, 180 µl lysates were introduced into the binding chamber through the inlet hole. There are three independent testing units on the compact cartridge. Each testing unit on the compact cartridge consists of (1) 30 µl binding buffer and 10 µl magnetic beads in the binding chamber, (2) 150 µl washing buffer in the washing chamber, and (3) 25 µl LAMP master mix in the reaction chamber (Figure 2-9A). Since the surface charge polarity of the magnetic beads is pH-dependent, and the surface charge polarity of DNA is negative for a wide range of pH values [73], the magnetic beads can attract or repel the nucleic acids by the different pH values of the preloaded buffer solution (Figure 2-4 and Figure 2-10). The magnetic beads were actuated by rotating the compact cartridge against a stationary magnet. In a control sequence, the DNA-carrying beads were directed into the different chambers until the target DNAs were eluted in the reaction chamber (Figure 2-10). The optimal rotation speed is experimentally determined by monitoring the magnetic bead motion. Although a faster rotation is preferred to reduce the whole processing time, the DNA-carrying magnetic beads might be lost from chamber to chamber if the rotation speed is too high. There is a tradeoff between the sample preparation efficiency and the whole process time. The whole process

can automatically prepare high-quality DNA samples from the human whole blood in less than 10 minutes.

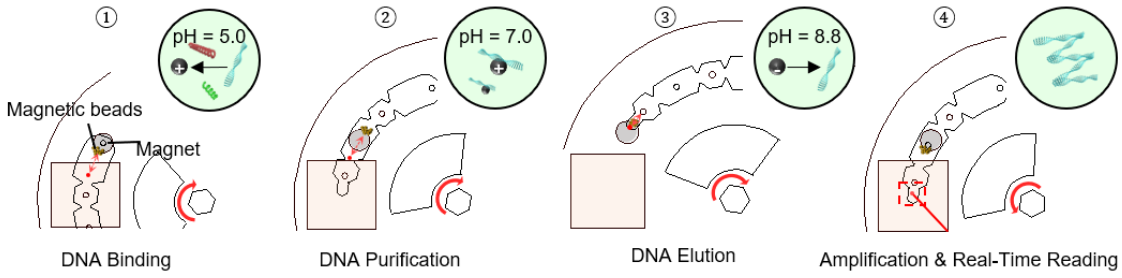

Figure 2-10: Illustration of integrated sample preparation and amplification steps on the reagent cartridge. By rotating the reagent cartridge against a stationary magnet in a specifically designed control sequence (steps 1-4), the pH-dependent charge switchable magnetic beads were directed from chamber to chamber, which allows for seamlessly integrated DNA binding, purification, elution, and amplification on the reagent cartridge.

2.6. Magnetic bead-based *P. falciparum* gDNA sample preparation on tube

We performed a reference experiment to confirm the compatibility of the ChargeSwitch forensic DNA extraction/purification kit. To validate the magnetic bead-based DNA extraction/purification method, we manually carried out tube-level sample preparation by pipetting (Figure 2-11A). In step 1, 20 µl of the cultured malaria-infected blood sample was initially dispensed to the tube, which contains 1 ml of lysis buffer and 10 µl of Proteinase K. This mixture was incubated at room temperature for 2 minutes to lyse the malaria parasites and RBCs. In step 2, 200 µl of purification buffer and 20 µl of magnetic beads were introduced by pipetting. In this step, the negatively charged target DNA bind to the positively charged magnetic beads (pH 5.0). In step 3, the DNA-carrying magnetic beads were enriched by a permanent magnet, and the remaining supernatant was removed.

Then 500 µl of washing buffer was introduced to remove possible inhibitors. In step 4, 150 µl of elution buffer was used to unbind the DNA from the magnetic beads due to charge repulsion (pH 8.8). In step 5, 1 µl of purified DNA was introduced to the LAMP master mix, which was transferred to the reagent cartridge and was run on the AnyMDx instrument for real-time amplification. All amplification curves of infected RBC samples showed clear exponential DNA amplification between 25 to 35 minutes (Figure 2-11B). This result confirms the success of the magnetic bead-based method for malaria DNA extraction and purification.

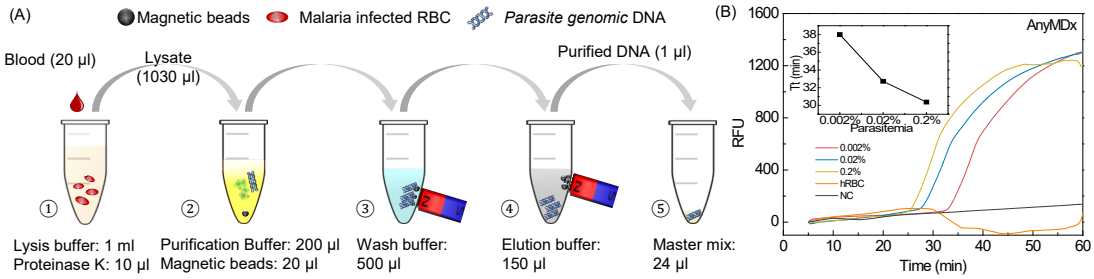

Figure 2-11: Illustration of the manual parasite genomic DNA extraction and purification procedures in a microcentrifuge tube. (B) The amplification curve for the manually extracted DNA sample on the AnyMDx instrument. The successful amplification of the tube-extracted DNA samples validates the effectiveness of the magnetic bead-based method.

2.7. LAMP assay test on the cartridge using purified *P. falciparum* gDNA

To validate the designed LAMP assay and the module level function (fluidic, thermal, mechanical, optical) of the AnyMDx instrument, the LAMP assay in the microfluidic reagent cartridge on the AnyMDx system was compared side-by-side with a real-time PCR using purified *P. falciparum* genomic DNA sample. To this end, purified *P. falciparum* genomic DNA (gDNA) was 10-fold serially diluted with Tris-EDTA buffer. LAMP master mix without *P. falciparum* gDNA was used

as a no template control (NTC). As shown in Figure 2-12A, the assay was firstly validated by a benchtop real-time PCR machine (MJ Research DNA Engine Opticon). A sharp increase in RFU values was observed from three diluted DNA samples, while the negative control showed no increase in RFU values (Figure 2-12A). The real-time performance of AnyMDx on the same sample sets is shown in Figure 2-12B, which demonstrated a distinguishable fluorescence threshold between positive and negative samples within 30 minutes. Besides, the result of the AnyMDx system was quantitative though the standard deviations are higher for low concentration samples. An inversely proportional relationship between the threshold time and the DNA concentrations (R^2 = 0.9998) was observed (Figure 2-12B inset). Note that AnyMDx has a linear region from 0.01 x to 1 x while the real-time PCR machine saturates at 1x concentration. This discrepancy might occur due to the dynamic range differences in the optical detectors and the thermal coupling efficiency in these two systems.

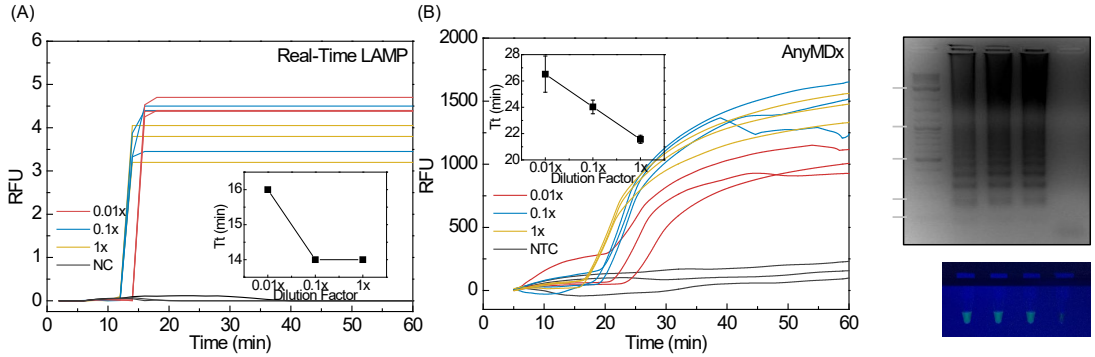

Figure 2-12: Validation of the LAMP assay and the AnyMDx instrument with laboratory purified DNA samples. (A) Benchmarking amplification curves obtained from the real-time PCR machine. 1x, 0.1x, and 0.01x denotes the dilution factors of the *P. falciparum* DNA samples (NTC: No template controls, T_t: Threshold time). (B) The amplification profiles acquired from the AnyMDx instrument. (C) Gel-electrophoresis analysis on a 2% agarose gel. The amplicons show a clear ladder-like pattern, the length of which verifies the LAMP assay's specificity against *P. falciparum*. (D) Emission visualized under the blue LED (λ=488 nm) illumination for various positive and negative samples.

To further evaluate if the amplicons were specifically from the designed targets, we performed gel electrophoresis analysis of the amplicons in 2% agarose gel. As shown in Figure 2-12C, the LAMP amplicons showed a clear ladder-like pattern with multiple bands of different molecular sizes due to its inverted-repeat structures [74]. More specifically, the length of the observed bands corresponds to the integral times of the target sequence (213 bp), indicating the amplified products were specific for the target sequence. Also, strong green emission (implying positive reactions) can be easily recognized by the naked eyes in the PCR tube under blue LED illumination in the dark environment (Figure 2-12D). From these results, we successfully verified the LAMP assay against *P. falciparum* genomic DNA and the modular function of the AnyMDx system.

2.8. Validation of streamlined sample process using *Pf*-infected whole blood

High-quality nucleic acid sample preparation is the bottleneck for most "sample-in-answer-out" molecular analysis.[75] Before we prepared the sample on the reagent cartridge, the pH-switchable magnetic beads-based method for DNA isolation was validated first in test tubes from the blood sample using the same reagents as on the reagent compact cartridge. Successful amplification of the tube-extracted DNA samples confirmed the effectiveness of the magnetic bead-based method (Figure 2-11). Afterward, we evaluated sample preparation in the reagent compact cartridge and the compatibility of the purified DNA with the subsequent LAMP assay. To test the DNA extraction efficiency on the reagent compact cartridge, we examined *P. falciparum*-infected blood samples of different parasitemia (0.2%, 0.02%, and 0.002%, prepared by dilution with healthy blood at 45% hematocrit), which were assessed by Giemsa-stained blood smears test prior to experiment. The infected blood samples were directly lysed in the collection tubes before loading into the reagent compact cartridge (Figure 2-10B). The following DNA binding, purification, elution, and the amplification were automatically carried out by the AnyMDx system (Figure

2-10C). As shown in Figure 2-13, the real-time amplification data for various parasitemia showed a clear quantitative trend, as compared to the lack of amplification signals in the negative control. Though quantitative analysis is not always required for point-of-care applications, it is valuable in many situations, for example, in determining the effectiveness of antimalarial therapy for malaria patients.[76] These results fully verified that the AnyMDx system could work in a "sample-in-answer-out" fashion by seamlessly integrating high-quality DNA preparation and real-time amplification on a single reagent compact cartridge.

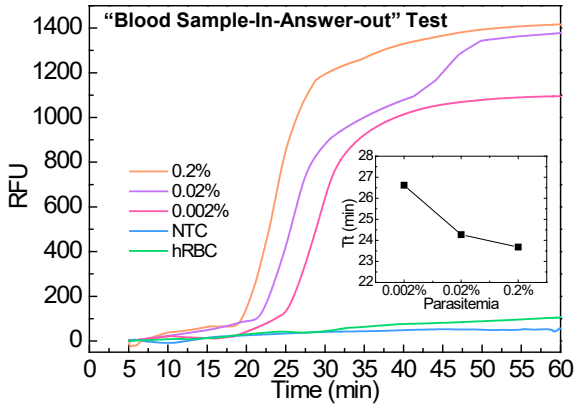

Figure 2-13: Validation of the AnyMDx system from the whole blood sample to the amplification result with integrated sample preparation on the reagent cartridge. The % value represents the parasitemia of the infected RBCs. (hRBC: healthy RBCs, NTC: No template controls, T_t: Threshold time)

2.9. Sensitivity estimation with whole blood

To evaluate the analytical sensitivity of our device in the real-world settings, we 10-fold diluted the *Pf*-infected whole blood with healthy blood to create mock samples with 10^{-6}% to 1% parasitemia. The parasite DNA samples were automatically prepared on the compact disc. Each parasitemia

sample was performed in triplicates, together with negative control on a single disc (four reactions per run). As shown in Figure 2-14A, a whole blood sample with parasitemia higher than 10^{-5}% could be identified. Since parasitemia is the ratio of the parasitized RBCs to the total RBCs, 10^{-5} % parasitemia would correspond to 0.5 parasites/μl (normal RBC count is ~5×10^6 cells/μl [26]). Although a rigorous report of the limit of detection (*i.e.*, analytical sensitivity) requires a statistical comparison with the analytical blank and should be expressed as a probability with confidence intervals [77], a quick eyeball of the data shown in Figure 2-14A suggests the whole blood sensitivity is around 0.5 parasites/μl. WHO estimates that analytical sensitivity needs to be lower than 2 parasites/μl for identifying low-level infection in a pre-elimination setting [78]. This sensitivity achieved in our device is comparable to other NAT methods (1-5 parasites/μl) [79] and suitable for detecting low-level asymptomatic carriers [25, 27, 80]. No amplification was observed for the healthy whole blood sample, which suggests the background human genomic DNA has negligible interferences. The amplification threshold time (T_t) was extracted for each parasitemia, and the results were shown in Figure 2-14B. The inversely proportional relationship between T_t and parasitemia confirmed that the quantitative ability is still valid with whole blood samples. It is interesting to note that the calibration curve shown in Figure 2-14B is not exactly linear which is likely because the DNA extraction efficiency is nonlinear for different cell numbers [81].

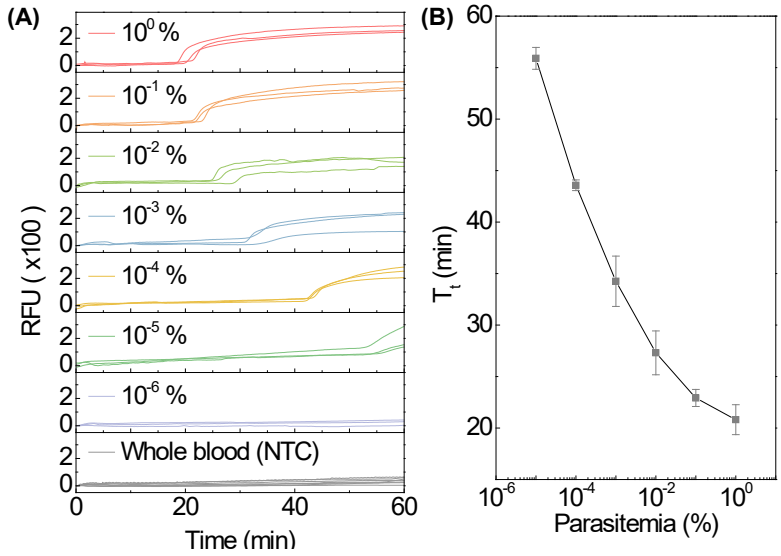

Figure 2-14: Sensitivity test with *Pf*-infected whole blood sample (A) Amplification curves for 10-fold serially diluted *Pf*-infected whole blood samples. Healthy human blood was used as an NTC. (B) The resulting calibration curve for the whole blood sample. Standard deviation values are from triplicates.

2.10. Cost analysis

The most significant advantage of the molecular test is their ability to detect extremely low-level malaria infections, which are often challenging for microscopy and RDTs. Nevertheless, the greatest hurdle for deploying a molecular analysis in resource-limited areas is its relatively high cost and the infrastructure investment. The AnyMDx system aimed to address this issue by delivering a sensitive malaria molecular test cost-effectively. The prototype AnyMDx instrument presented in this work could be built for a total amount of ~$176 (see Table 2-3 for cost breakdown). The disposable reagent compact cartridge (including the sample preparation and the amplification reagents) costs ~$1.14 per each test (see Table 2-4). Note that this cost analysis is only to provide a ballpark figure to the interested researchers to replicate the system. Reduced cost for scaled

manufacturing, increased cost for medical device regulation, and licensing cost is not included in this analysis since this is beyond the scope of this study. The low cost of this sensitive molecular test provides an excellent opportunity for the field applications of this mobile molecular diagnostic system. Moreover, the manufacturing of the AnyMDx instrument is highly scalable in a cost-effective way. The AnyMDx system could be easily reproduced within a day in ordinary lab settings.

Table 2-3: Cost breakdown for the AnyMDx instrument

System	Vendor	Description	Part#	Function	Unit Cost ($)	Unit Qty.	Ext Cost ($)
Bluetooth	Adafruit	Bluetooth Low Energy (BLE 4.0)	1697	Bluetooth	19.95	1	19.95
Electronics	Adafruit	Arduino Mega 2560 R3	DEV-1106	Microcontroller	45.95	1	45.95
Electronics	Adafruit	36-pin stripe male header	392	Headpins	4.95	0.083	0.41
Electronics	Newark	Detector Switch	83T2715	Switch	0.27	1	0.27
Electronics	Sparkfun	DC Barrel Power Jack/Connector	PRT-00119	Power Connector	1.25	1	1.25
Electronics	Newark	Through-Hole Resistor, 10 kΩ	38K0328	Temperature control	0.09	3	0.26
Electronics	Adafruit	Shield Stacking Headers for Arduino	85	Wire Sockets	1.95	0.33	0.64
Electronics	Newark	Through-Hole Resistor, 100 Ω	38K0326	Resistors for LED	0.09	2	0.18
Electronics	Adafruit	Premium Male/Male Jumper Wires	758	Wires	3.95	0.75	2.96
Electronics	Newark	Diode, Standard, 1A, 50A	78K2043	Diode	0.07	1	0.07
Electronics	Newark	Trimmer Potentiometer, 10kΩ	16F7158	LCD adjustment	1.65	1	1.65
Enclosure	Mcmaster	Adjustable-Friction Hinge	1791A44	Hinge	6.72	2	13.44
Enclosure	Amazon	FLASHFORGE ABS Filament	90003001	3D platform material	18.50	0.3	5.55
Enclosure	Sparkfun	Metric Pan Head Machine Screws	92005A033	For holding LCD	3.67	0.04	0.15
Enclosure	Mcmaster	Acrylic Sheet, 1/8" Thick, 12" x 24"	8505K12	Holding plates	13.46	0.375	5.05
Enclosure	Thorlabs	Screws (M4 cap screw)	W8S038	For holding hinge	3.25	0.04	0.13
Enclosure	Thorlabs	Screws (M3 set screw)	SS3M6	For holding color sensor	9.25	0.0006	0.01
Enclosure	Home Depot	Screw Assortment Kit	800934	Hold plates	6.50	0.034	0.22
LCD	Sparkfun	Basic 16x2 Character LCD	LCD-00709	LCD	15.95	1	15.95
Magnets	Mcmaster	Neodymium Disc Magnet Nickel	58605K33	Holding magnetic beads	2.69	1	2.69

Optics	Adafruit	Color Sensor	1334	Detection	7.95	1	7.95
Optics	Edmund	Optical Plastic Light Guide2	#02-538	Guiding light	2.55	0.06	0.15
Optics	Newark	CREE LED, Blue, T-1 3/4 (5mm)	04R6674	Fluorescence excitation	0.21	1	0.21
Optics	Mcmaster	Dispensing Needle	75165A551	Holding optic fiber	13.00	0.02	0.26
Servo	Adafruit	Standard Size - High Torque Servo	1142	Actuation of spindle platter	19.95	1	19.95
Thermal	Thermoelectric	Cold Plate	CP-0.91-0.91	Heating Stage	5.75	1	5.75
Thermal	Digikey	Peltier Heater	102-1667-ND	Heater	16.00	1	16.00
Thermal	Newark	N Channel Power MOSFET	63J7707	Switch for Peltier heater	1.66	1	1.66
Thermal	Newark	Thermistor	95C0606	Temperature sensing	7.34	1	7.34
Thermal	Newark	Capacitor 470uF	65R3137	Power Stabilizing	0.11	1	0.11
				Total Cost			**$ 176.16**

Table 2-4: Disposable reagent compact disc cost per test.

Reagents	Vendor	Function	Stock Vol (ml)	Unit Cost ($)	Vol. (μl)/rxn	Ext Cost/rxn
NEB Isothermal Buffer	NEB	LAMP master mix	6	24.00	2.5	0.010
F3	IDT	LAMP master mix	1.4	9.22	0.25	0.002
B3	IDT	LAMP master mix	1.5	10.22	0.25	0.002
FIP	IDT	LAMP master mix	1.0	7.14	2.00	0.013
BIP	IDT	LAMP master mix	1.4	9.18	2.00	0.013
LF	IDT	LAMP master mix	1.7	11.86	1.00	0.007
LB	IDT	LAMP master mix	1.3	8.61	1.00	0.007
$MgSO_4$	NEB	LAMP master mix	6	20.00	1.75	0.006
Calcein	Sigma-Aldrich	LAMP master mix	8000	133.00	0.63	0.000
$MnCl_2$	Sigma-Aldrich	LAMP master mix	100	62.60	1.88	0.001
dNTP Mix	Thermo Fisher	LAMP master mix	3.2	107.00	3.50	0.117
2.0 Bst polymerase	NEB	LAMP master mix	1	264.00	1.00	0.264

UltraPure Water	VWR	LAMP master mix	20	91.88	7.25	0.033
Lysis Buffer	Invitrogen	Sample Prep.	800	142.00	1000.00	0.178
Purification Buffer	Invitrogen	Sample Prep.	20	28.97	30.00	0.043
Wash Buffer	Invitrogen	Sample Prep.	100	144.84	150.00	0.217
Proteinase K	Invitrogen	Sample Prep.	1	1.45	10.00	0.014
Magnetic Beads	Invitrogen	Sample Prep.	2	2.90	10.00	0.014
Acrylic Glue	ePlastics	Compact disc	118	9.69	1.5	0.041
1/32" Acrylic Sheet	ePlastics	Compact disc	-	14.98	-	0.098
1/16" Acrylic Sheet	ePlastics	Compact disc	-	17.72	-	0.058
					Total Cost	**$ 1.14**

The instrument-to-instrument variation was small enough to deliver the same quality of quantitative molecular analysis (Figure 2-15). As a result, we envision that the AnyMDx would enable cost-effective malaria molecular diagnosis in resource-limited regions by decreasing the cost, increasing the ease of use, and maintaining high sensitivity.

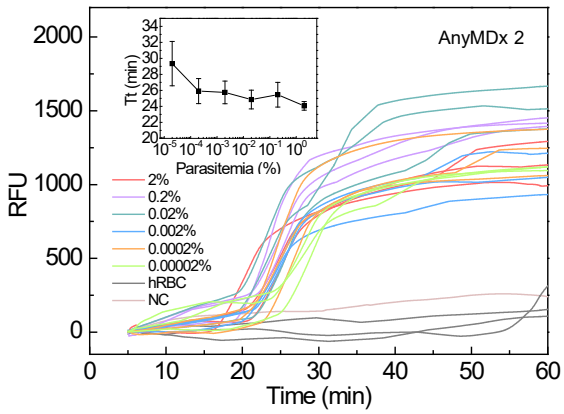

Figure 2-15: DNA amplification profiles of AnyMDx2. The manufacturing of the AnyMDx instrument is repeatable in a cost-effective way. We built the second instrument of AnyMDx (named AnyMDx2) and performed a similar sensitivity experiment (as described in the sensitivity section). Amplification curves from six different parasitemia samples show apparent exponential

increases of fluorescence, while that of the negative controls (master mix and hRBC) shows no amplification. (RFU: relative fluorescence unit, hRBC: healthy RBCs, NC: negative control)

2.11. Summary

In summary, we developed a field-deployable mobile molecular diagnostic system for rapid and accurate diagnosis of malaria infection in resource-limited areas at the point of need. The AnyMDx system seamlessly integrated all nucleic acid testing steps from sample preparation to real-time amplification and detection. The standalone and user-friendly system works in an "insert-and-test" fashion and could specifically detect *P. falciparum* species in 40 minutes from a whole blood sample. The sensitivity against *P. falciparum* was ~0.6 parasites/μl, which is important for identifying asymptomatic parasite carriers who will otherwise be missed by microscopy or RDT [25, 31, 82]. The cost-effective system allows for the deployment of a benchtop-quality malaria nucleic acid testing into the remote areas for malaria elimination. Moreover, the modular design of a separate reagent compact cartridge and a durable analyzer makes the system versatile. As a platform technology, the AnyMDx design should create a new paradigm of molecular diagnosis towards a variety of infectious diseases at the point of care.

Chapter 3 Multiplex Real-time Fluorescence Nucleic Acid Testing For High-throughput Malaria Screening

In Chapter 2, I have discussed the singleplex field-deployable mobile nucleic acid testing device for sensitive malaria detection. Although the singleplex system allows excellent diagnostic performance, throughput is still limited for field use. This chapter will present a multiplexed real-time fluorescence nucleic acid testing device for high-throughput malaria detection. The 4-plex device consists of a compact analyzer and a disposable microfluidic reagent compact disc. The parasite DNA sample preparation and subsequent real-time LAMP detection were seamlessly integrated on a single microfluidic compact disc, driven by energy-efficient, non-centrifuge based magnetic field interactions. Each disc contains four parallel testing units, which could be configured either as four identical tests or as four species-specific tests. When configured as species-specific tests, it could identify two of the most life-threatening malaria species (*P. falciparum* and *P. vivax*). The NAT device is capable of processing four samples simultaneously within 50 min turnaround time. The combination of the sensitivity, specificity, cost, and scalable sample preparation suggests the multiplexed real-time fluorescence LAMP device could be particularly useful for malaria screening in the field settings.

3.1. Introduction to high-throughput nucleic acid testing in the field

Malaria elimination program requires a diagnostic device that can facilitate case management, active community surveillance, and parasite screening of asymptomatic carriers [21, 83]. Due to its excellent sensitivity, NATs have been considered as a strong candidate for malaria diagnosis. However, the turnaround time for most NATs requires hours to several days from sample collection to test results [84]. Although most NAT assay takes less than an hour, the primary reason for slow turnaround time is blood sample transport from a clinical site to a centralized laboratory where NATs are available [84].

Modification to make NATs more appropriate for low-resource point-of-care setting have been reported to reduce turnaround time by eliminating the sample transfer time [85]. For instance, recently described illumigene Malaria LAMP assay showed 'sample-to-answer' turnaround time in less than an hour with a throughput of 10 test/run using a manual blood sample preparation step with an incubator reader [86]. Despite significant effort and progress towards field deployment of malaria NATs assays, test throughput is still restricted by the manual nucleic acid sample preparation from raw peripheral blood [79, 87]. Current sample preparation usually involves lengthy or error-prone manual processes such as gravity-driven filtration [86], centrifugation [88]. For the promising NAT technologies to be used as high-throughput malaria screening tests in the field, the DNA extraction method should be simple, rapid, scalable, fully automated, free of cross-contamination, and seamlessly integrated with the amplification for immediate analysis.

In this chapter, we present a multiplexed real-time fluorescence LAMP device suitable for high-throughput field detection of *Pf* and *Pv* with automated and scalable sample preparation capability. The device uses a non-centrifugal method for solid-phase DNA extraction by actuating the DNA-carrying magnetic beads against the stationary reagent droplets. The device consists of a palm-sized

analyzer and an enclosed microfluidic reagent compact disc. The reagents were preloaded and separated on the microfluidic reagent disk by teeth-shaped passive valves. The preloaded and ready-to-use microfluidic reagent disc contains four parallel testing units. It could be configured either as four identical tests to increase the testing throughput or as four species-specific tests to distinguish *Plasmodium* genus, *Pf* and *Pv* species. Each test unit automatically performs the parasite DNA binding, washing, elution, and immediate real-time isothermal amplification and fluorescence detection. This seamless integration from the sample to result on a single microfluidic reagent compact disc significantly minimized the manual workload needed for performing the NATs. The device could deliver sensitive (~0.5 parasites/μl) NAT results directly from a small volume of whole blood samples within 50 minutes for a material cost around $1/test.

3.2. Multiplexed instrumentation integration

3.2.1. 4-plex analyzer

Figure 3-1A shows an exploded view of the real-time fluorescence LAMP device. The mobile platform was designed in SolidWorks and prototyped by a 3D printer. The device has four parallel testing units and has a small footprint of 10×12×12 cm^3 (Figure 3-1B). The fully integrated device consists of thermal, optical, electromechanical, and data subsystems.

Thermal subsystem. Four resistive-heating elements were connected in series to maintain the uniform temperature in each testing unit. Each power resistor was bonded to the backside of an aluminum heating plate by thermal paste. A micro-thermistor was embedded in each heating plate for real-time temperature monitoring. Negative thermal feedback was used to maintain the desired temperature during the DNA amplification.

Optical subsystem. For real-time tracking of the DNA amplification, we used four LED light sources (λ=488nm). Each of them was directed towards individual reaction chambers through polymer optical fibers. Each LED was connected with a potentiometer to ensure the uniformity of the excitation light. The incidence of the excitation LED lights was perpendicular to the optical sensors to minimize the excitation interference (zoomed illustration in Figure 3-1B).

Electromechanical subsystem. A customized printed circuit board (PCB) with an embedded microcontroller unit (MCU) operates the whole device from sample preparation to the result report. A rechargeable 9V portable Lithium-ion battery powers the entire system and could last for >15 hours before recharging.

Data subsystem. The fluorescence intensity from four optical sensing units was sampled at a constant interval and displayed on the LCD touchscreen in real-time. A built-in moving average algorithm smoothed the signal with background noise removed. The threshold time (*Tt*) was obtained when the slope of RFU (*dRFU/dt*) reached the peak (Figure 2-7).

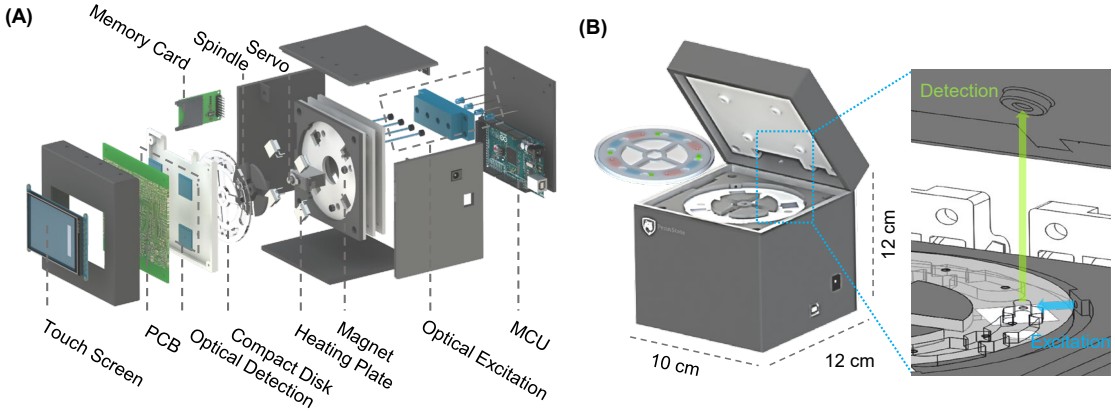

Figure 3-1: Overview of the device. (A) Exploded view of the device, showing the assembly of various components. (B) Schematic of the assembled device and the quadplex microfluidic reagent

compact disc. The form factor of the analyzer is palm-sized. The reagent compact disc is secured to the spindle platter. A real-time fluorescence sensing scheme is integrated on the analyzer.

3.2.2. 4-plex microfluidic reagent compact disc

The microfluidic reagent compact disc has a diameter of 9.6 cm and a thickness of 3.2 mm. The top, spacer, and bottom polymethyl methacrylate (PMMA) layers were designed using AutoCAD and patterned by a CO_2 laser cutting machine (Epilog Helix 24 Laser System). All three layers were aligned using the alignment hole and permanently laminated with adhesive solvent. The assembled disc has four testing units, and each unit contains three working chambers (Figure 3-2): binding (210 µl), washing (150 µl), and reaction chambers (25 µl). Liquid phase reagents (beads, washing buffer, and master mix) were loaded into the disc immediately before use. The reagents could also be preloaded into the disc and would last for at least 1 week if stored at 4 ºC.

Each chamber was isolated by a valve chamber (80 µl) to prevent the reagent mixing. The valving chambers were filled with FC-40 oil or air. The FC-40 oil, which seals the LAMP reaction chamber, helped prevent master mix evaporation during the thermal process. The air-filled valve was surface treated with water-oil repellent to create a barrier for the amphiphilic lysis buffer. After the sample loading, the whole disc was sealed with a PMMA cap to avoid potential cross-contamination.

3.3. Overall testing workflow

The workflow of the device consists of four steps (Figure 3-2). The 20 µl of finger-prick blood was collected using a capillary tube and lysed in the collection tube filled with 1000 µl of lysis buffer. 180 µl of blood lysate was transferred into each binding chamber of the testing units on the reagent

compact disc. After loading the sample, the disc was sealed with PSA tape and inserted into the mobile analyzer for a streamlined nucleic acid sample preparation and amplification process (enlarged view of step 3 in Figure 3-2). During the amplification, the fluorescence intensity data were recorded on a non-volatile memory card and displayed on the LCD screen in real-time. Users also have an option to receive the results using a smartphone.

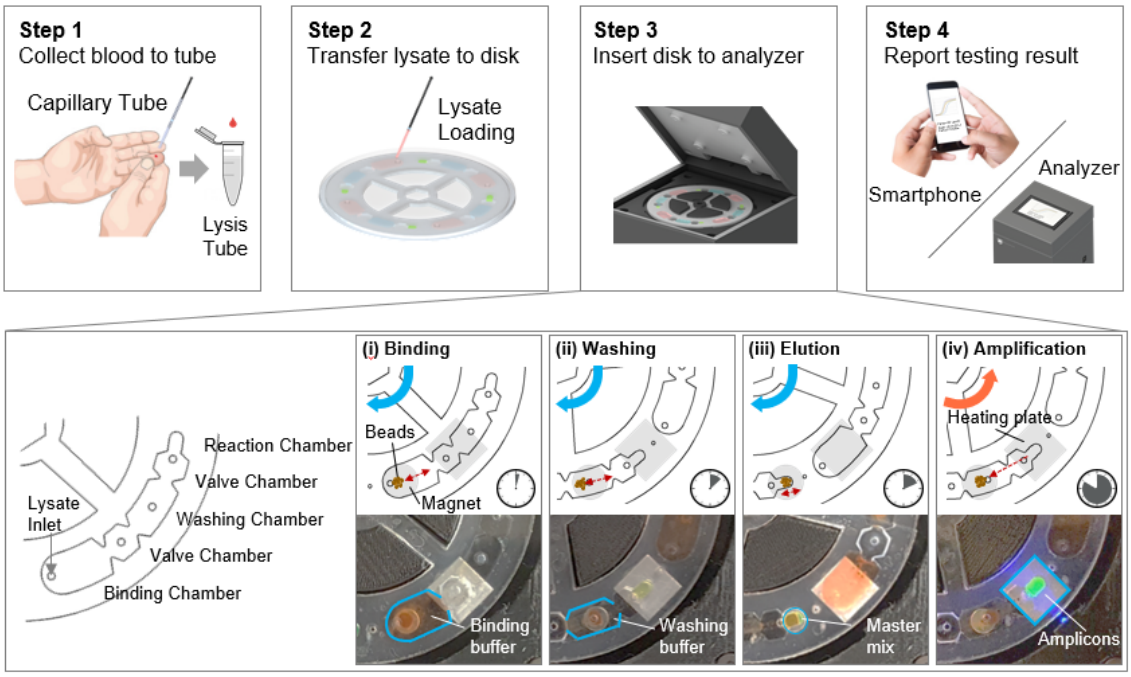

Figure 3-2: Workflow of the device. In step 1, whole blood is collected into the lysis buffer by the capillary tube. In step 2, the lysate is loaded into the binding chamber of the four testing units. In step 3, the disc is sealed and inserted into the analyzer, which then performs automated sample preparation and amplification. This automated process consists of four steps: binding (3 min), washing (4 min), elution (3 min), and amplification (40 min). During the amplification process, the real-time fluorescence signal from each testing unit was recorded and analyzed. Finally, in step 4, the testing results are reported.

3.4. Robustness of the passive valve on the microfluidic compact disc

One major challenge in applying microfluidics towards point-of-care testing is the need for peripheral tubing and pumping systems to drive the liquid movement [89, 90]. One exception is the centrifugal-type microfluidic platform, where the reagent can be preloaded and driven by centrifugal forces[91]. The preloaded reagents rely on passive valves to prevent mixing[92, 93]. However, fluid control and separation in the centrifugal platform were challenging because an identical centrifugal force field is applied to all of the liquids on the disc within which a different flow rate is needed [90, 94]. In addition, centrifugal force is non-linear and requires rotational frequencies in the range of several thousand revolutions per minute (RPM).[91] The electrical power needed to drive this motion is tremendous.

The microfluidic reagent disc used in the system does not rely on the centrifugal force to move the liquid. Instead, we actuate the DNA-carrying magnetic beads against the stationary reagent droplets. The reagents were preloaded and separated on the microfluidic reagent disc by teeth-shaped passive valves (Figure 2-10). Structural pinning effect [95, 96] and modified surface tension are the underlying principles that enable the teeth-shaped valves to securely hold the liquid in each chamber. The pinning effect refers to the fact that a sharp bending angle (α) of the teeth structure radically increases the liquid/vapor interface area and raises the activation energy, which prevents fluid from overcoming the barrier (Figure 3-3A) [95]. The enhanced surface tension is another important aspect of our passive valve structure. The valve surface was treated with water-oil repellent to increase the activation barrier by introducing a higher surface tension [95], which also helps circumvent cross-contamination during sample preparation.

To demonstrate the robustness of the passive valve for preventing the reagents from mixing under the harsh mechanical vibration, we performed a drop test on the microfluidic compact disc. Three different colors of food dyes were preloaded into each reagent chamber for visualization of any liquid movement. Each reagent-loading hole was sealed with pressure-sensitive adhesive (PSA) to prevent leakage. The disc was dropped from a height of 20 cm along a guiding rod towards a rigid surface for 25 times. The disc was inspected every five drops with naked eyes to confirm the functionality of the valve. The result showed that the teeth-shaped valve endured 25 consecutive drops without reagents mixing (Figure 3-3). Besides, the robustness of the passive valve was also validated through hand agitation to the microfluidic disc.

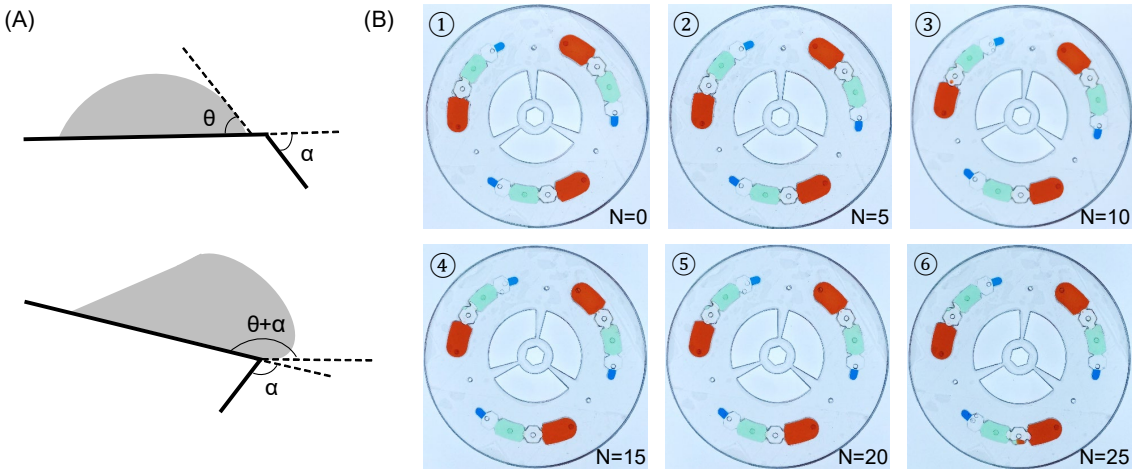

Figure 3-3: Illustration of the pinning effect and photo images of the drop test results. (A) A droplet on a solid surface with a contact angle of θ, which will be increased up to $\theta+\alpha$ when moving towards a three-phase edge, where α is a bending angle[1]. This implies that larger α allows a higher activation barrier for the passive valve. (B) The drop test to evaluate the robustness of the teeth-shaped passive valves on the reagent compact disc under the harsh mechanical vibration. (N denotes the number of drops)

3.5. Scalable streamlined sample preparation

One of the significant challenges for NATs at the point of care is related to the front end of the assays - nucleic acid extraction from raw samples [87]. For malaria mass screening applications, the ideal sample preparation should be simple, scalable, and easy-to-operate. We realized a streamlined process for preparing four samples in parallel on a single enclosed microfluidic disc. In contrast to the conventional lab-on-a-disk devices that rely on energy-hungry centrifugal forces [91, 97] [98], our device operates with a non-centrifugal and energy-efficient magnetic interaction method. The process for each sample consists of the following three steps: binding, washing, and elution (step 3 of Figure 3-2). The negatively charged parasite DNAs first bind to the pH-sensitive charge-switchable magnetic beads (ChargeSwitch® Forensic DNA Purification Kits, Invitrogen) at pH 5. During the binding process (~3 min), the reagent compact disc was rotated back and forth slowly to ensure thorough mixing of the beads and the lysate. The DNA-binding magnetic beads were then transferred to the washing chamber by magnetic actuation. The washing process lasts for about 4 min, and the magnetic beads with purified DNAs were further transferred to the reaction chamber (LAMP master mix). The LAMP master mix has a pH of 8.8, which switches the surface charge of the magnetic beads towards negative. The negatively charged DNAs were therefore repelled off from the magnetic beads and eluted into the master mix. After that, the residual magnetic beads were removed from the reaction chamber before initiating the LAMP reaction. The entire sample preparation was multiplexed for four samples and could be finished in less than 10 minutes with minimal user intervention. The sample numbers could be easily scaled up if needed in the future.

3.6. Multiplex parallel fluorescence sensing

Uniformity. For the quadruplex parallel NAT device, the fluorescence sensing consistency among different channels is essential for quantitative measurement. We tested fluorescent calcein dye at various known concentrations. At each concentration, identical calcein aliquots were loaded into the four reaction chambers for fluorescence intensity measurement. Figure 3-4A shows the relative fluorescence unit (RFU) distribution from each optical channel at different concentrations. The quantitative uniformity among the four channels is excellent, as seen by the small standard deviation for the RFU values. Moreover, as expected, the mean fluorescence intensity was proportional to the calcein concentration, and a 2-fold calcein concentration difference could be discriminated (inset in Figure 3-4A). To further validate the fluorescence sensing uniformity during the real-time LAMP process, four identical 1 μl of *Pf* genomic DNA was directly loaded into each reaction chamber, and the real-time amplification curve was monitored (Figure 3-4B). We repeated each test three times. As shown in the inset of Figure 3-4B, the variation of threshold time (T_t) among different fluorescence sensing channels was ~1.5 minutes. These results validate the fluorescence sensing uniformity among different optical channels.

Quantitative. A series of 10-fold dilutions of *Pf* genomic DNA in Tris-EDTA buffer was used to validate the quantitative ability of the device. For each concentration, a set of three identical *Pf* genomic DNA samples and one internal negative control were loaded into each of the four reaction chambers on the disc. The DNA sample volume is 1 μl, and the LAMP master mix is 24 μl. Figure 3-4C shows real-time amplification results from various concentrations of *Pf* genomic DNA. The mean and standard deviation of the amplification threshold time (T_t) was obtained from the triplicates for each concentration. As shown in the bottom subplot of Figure 3-4C, a clear linear relationship was observed between T_t and the dilution factor, which could be used as a reference

curve for quantification. The quantitative ability is important for assessing parasite load in the blood, a useful indicator for determining the proper antimalarial drug dosage [99].

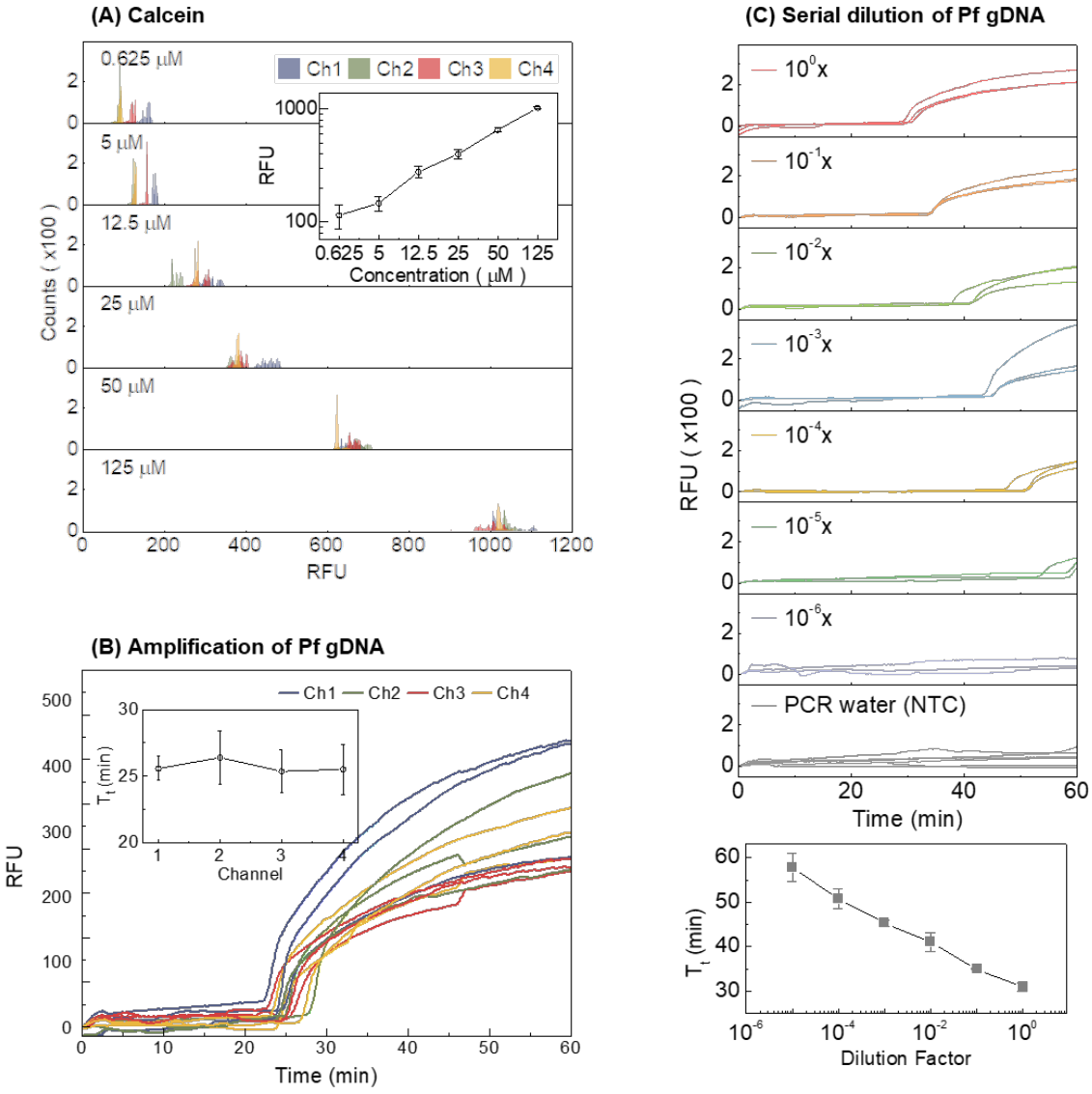

Figure 3-4: Validation of the optical sensing uniformity. (A) With fluorescent calcein dye, the RFU distribution for the four optical channels was evaluated at a series of calcein concentration. A linear dependence of the RFU on the calcein concentration was observed in the range of 0.625-125 μM. The RFU variation from the four channels is small. (B) With *Pf* genomic DNA at constant concertation, the variations of the amplification threshold time (T_t) obtained from the real-time curve is ~1.5 min. (C) Amplification curves for 10-fold serially diluted *Pf* genomic DNA samples.

The bottom plot shows the calibration curve for the *Pf* genomic DNA. Standard deviation values are from triplicates.

3.7. Whole blood-based *Pf*, *Pv* and *Pan-Plasmodium* identification

To evaluate the specificity of the device, we prepared whole blood samples spiked randomly with *Pf* and *Pv*. Those sample's species information is recorded but blinded to the tester. The reagent compact disc was configured as species-specific tests, as shown in Figure 3-5**A**. Each test disc incorporates an internal negative control unit to monitor the test quality. A threshold of 100 RFU is experimentally determined to differentiate positive and negative results. Figure 3-5**B** shows the result from a representative set of samples (*i.e.*, *Pf*, *Pv*, mixed, and healthy). The species information for a particular infected whole blood sample can be derived from four qualitative results on the single microfluidic disc. For example, the *Pf*-infected sample (first row of Figure 3-5**B**) can be identified by the *Pf*-specific assay as well as the genus-specific assay. In contrast, the mixed infection sample can be detected when *Pf*-, *Pv*-, and genus-specific assays all show positive. Since *Pf* and *Pv* are the two most prevalent species that pose the greatest threat to the human, identification of these major malaria parasite species in the field could provide the malaria transmission profile to the healthcare workers and enable the effective malaria eradication strategy [79].

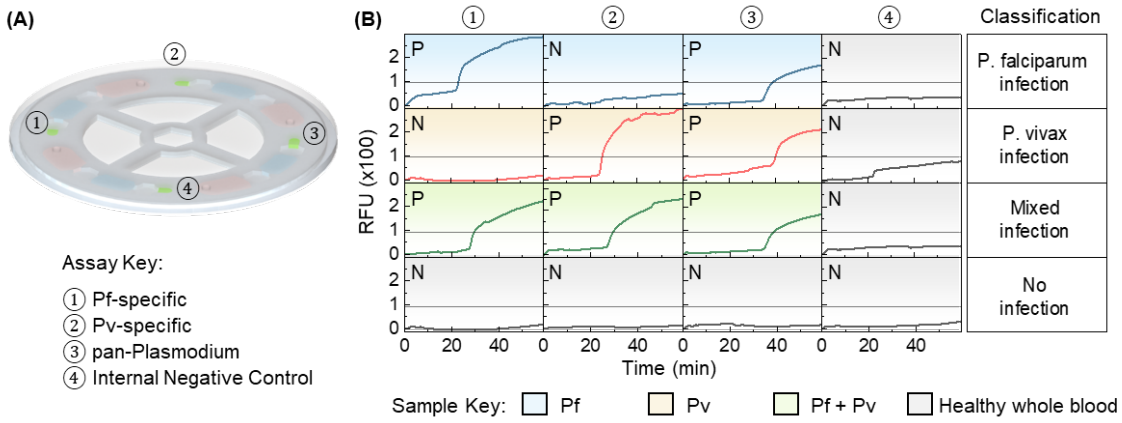

Figure 3-5: Species- and genus-specific tests using spiked whole blood samples. (A) The reagent compact disc was configured as species-specific tests. The testing unit 1 and 2 contains *Pf*- and *Pv*-specific primer sets, respectively. The testing unit 3 has a genus-specific primer set. Testing unit 4 is for internal negative control. (B) The result from a representative set of samples (*i.e.*, *Pf*, *Pv*, mixed, and healthy). A threshold of 100 RFU (dashed line) is experimentally determined for positive and negative differentiation. The species information for a particular infected whole blood sample can be derived from four qualitative results on the single microfluidic disc (each row).

3.8. Summary

The palm-sized nucleic acid testing device with quadruplex parallel reactions was developed and validated towards a low-cost malaria screening test. The device could perform the integrated and automatic sample preparation for parasite DNA extraction and streamlined real-time amplification on a single microfluidic reagent disc. The quadplex device could be configured either as four identical tests to increase the throughput or as four species-specific tests. The parallelization could be easily scaled up if needed in the future. The quantitative ability of the device could enable parasite load assessment for prescribing a correct dose of antimalarial drugs. The analytical sensitivity against *Pf*-infected whole blood samples is ~0.5 parasites/µl, adequate for detecting asymptomatic parasite carriers. The combination of the sensitivity, specificity, cost, and scalable sample preparation suggests the real-time fluorescence LAMP device could be particularly useful

for malaria screening in the field settings. Considering the limited reagent lifetime at room temperature, the challenge of storage and transport of the liquid phase on the microfluidic reagent disc needs to be addressed in our future studies, preferably with reagent lyophilization.

Chapter 4 High-throughput And Label-free Parasitemia Quantification For Malaria-infected Red Blood Cells

As a potential label-free mechanical biomarker [100-105], the RBC deformability is highly relevant to the malaria infection status, thus it can be used as an indicator for understanding malaria pathophysiology. Although precise cell deformability at single cell level can be achieved using conventional methods (e.g., micropipette aspiration [106], optical stretching [107], atomic force microscopy (AFM) [108], and magnetic bead-based rheology [109]), widespread use of cell mechanotyping in cell screening and medical diagnosis is still hampered by the low throughput ($10\text{-}10^2$ cells/hour).

In Chapter 4, we will discuss a high throughput and label-free cell deformability microfluidic sensor for quantitative parasitemia measurement and stage determination of *Plasmodium falciparum*-infected red blood cells (*Pf*-iRBCs). The cell deformability is measured by evaluating the translocation time when each cell squeezes through a microscale constriction. More than 30,000 RBCs can be analyzed for parasitemia quantification in under 1 min with a throughput ~500 cells/s. Moreover, the device can also differentiate various malaria stages (ring, trophozoite, and schizont stage) due to their varied deformability. As compared to the microscopy and flow cytometry, this microfluidic deformability sensor would allow for label-free and rapid malaria parasitemia quantification and stage determination at a low-cost.

4.1. Introduction to high-throughput parasitemia quantification by *pf*-iRBC deformability characterization

Parasitemia is a critical parameter for quantifying the parasite load in the organism and indicates the degree of an active parasitic infection. Quantitative measurement of parasitemia and stage determination is important in many phases of malaria assessment, such as the diagnosis and the therapy follow-up, particularly in the chronic phase [110].

The microscopy-based morphology analysis remains the gold standard for parasitemia quantification. Although this approach can identify parasitemia as low as 0.001% [111], it has several drawbacks, including the reliance of an expert reading Giemsa-stained blood smears, subjectivity, low reproducibility and relatively low speed (5 mins/slide) [112]. The flow cytometry was developed to overcome the speed limitation of the microscopy. However, the high cost of the instrumentation and the labeling process limits its widespread usage [113]. Besides, both microscopy and flow cytometry would require a time-consuming staining process for labeling.

It is well known that *Pf*-iRBCs become increasingly rigid (less deformable) as they mature [114], thus the deformability has the potential to be used as a mechanical biomarker to distinguish the healthy and the infected RBCs at various stages. To date, various microfluidic-based methods have been developed to interrogate cell deformability. For example, non-physical constraint-based interrogation (hydrodynamic pressure, *e.g.*, inertial microfluidics [115], and real-time deformability cytometry [116]), and physical constraint-based interrogation (e.g., single micropore [117], single microchannel [118, 119], and arrayed microchannels [120-122]). Despite success in the qualitative measurement of *Pf*-iRBCs deformability properties, a high throughput quantitative parasitemia measurement has yet to be developed.

In this chapter, we discuss a novel a label-free strategy for quantitative and high-throughput parasitemia measurement and stage determination for *Pf*-iRBCs using microfluidic cell deformability sensor. The microfluidic sensor is capable of analyzing more than 30,000 RBCs within 1 min (throughput ~ 500 cells/s). Moreover, the device is able to differentiate various malaria stages among the ring, trophozoite, and schizont stage. We envision that the deformability sensor will enable careful study on the pathophysiology of malaria-infected red blood cells.

Table 4-1: Summary of the microfluidic deformability characterization devices.

	DC	**RT-DC**	**iMCS**	**SMR**	**Deformability Sensor**
Cell Compression	Hydrodynamic Stretching	Hydrodynamic Stretching	Collision	Constriction	Constriction
Deformability Index	Aspectio ratio	Circularity	Aspect ratio	(Passage time)$^{-1}$	Transit time
Detection	Imaging	Imaging	Imaging	Cantilever	Electrical
Analysis	Offline	Real-time	Real-time	Offline	Offline
Throughput (cell/s)	2,000 – 65,000	100	450	1	500
Physical Contact	No	No	Yes	Yes	Yes
Ref.	[115, 123]	[116, 124]	[125]	[126]	[127]

4.2. Cell deformability sensing principle

Figure 4-1a shows the schematic and the corresponding equivalent circuit model for the microfluidic deformability sensor. The device consists of a well-engineered micropore constriction (5×5 μm^2) for the cell to squeeze through. The loading channel's cross-sectional area (1000×25 μm^2) is much larger than that of the micropore to reduce the hydrodynamic and electrical resistance. The electrical resistance of the microfluidic sensor is mainly dominated by the micropore constriction (*i.e.*, R_{gap} is much larger than other resistances in Figure 4-1b. For a reason, significant ionic current drop occurs during a single cell translocation event due to the reduced conductance at the constriction.

For electrical measurement, we typically applied a constant voltage (600 mV DC) across the micropore constriction. The ionic current was monitored as each single individual RBC translocating through the micropore. The ionic current traces were recorded by an amplifier (Axopatch 200B, Molecular Devices, USA). The analog output of the amplifier was sampled with a 16-bit DAQ card (NI PCI-6363, National Instruments, USA) and a data acquisition software (LabVIEW) (Figure 4-1a). The sampling rate for the measurement was 100 kHz. A custom-built MATLAB (MathWorks) program was developed to analyze the data off-line. The translocation time (dwell time) was extracted from each cell when translocating the micropore. The time threshold to differentiate the hRBC and the *Pf*-iRBCs was set by the mean value plus three times sigma of the hRBC dwell time (a Gaussian distribution).

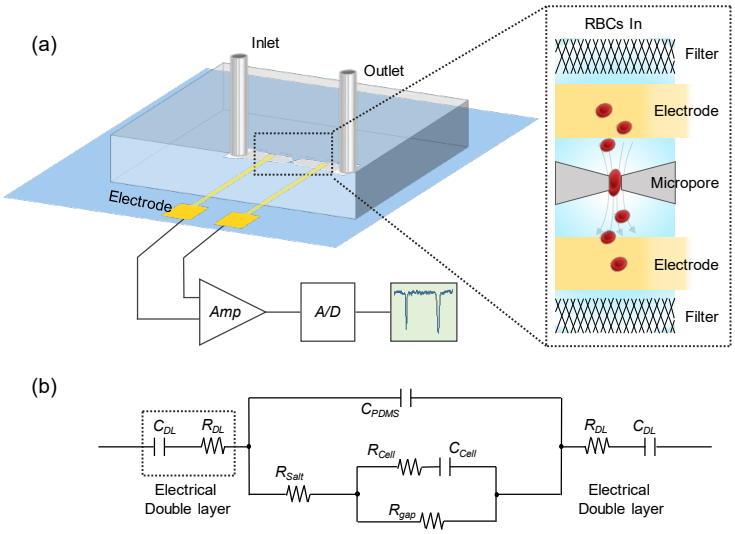

Figure 4-1: Deformability sensor for highly-throughput and label-free parasitemia quantification. (b) The equivalent circuit model for the sensor.

The micropore has a slightly smaller size than that of the RBCs, RBCs have to squeeze through the micro-constrictions. As a cell pass through a micropore, the friction, which is a normal force to the channel, determines the velocity of cell at micropore [128]. This normal force depends on cell deformability. The higher normal force causes higher friction and slows down the cell transit velocity, leading to a longer translocation time for stiff cells. Therefore, the cell translocation time can be considered as an indirect indicator for the cell deformability. For example, the rigid Pf-iRBCs will spend more time (on average) squeezing through the micro-constriction than the more deformable healthy RBCs (hRBCs). The applied pressure, cell size, deformability, elastic modulus, pore size, and the surface properties of PDMS and cells are all friction factors [129]. Parameters other than the cell deformability remain constant for a given experimental setup for consistency.

4.3. Microfluidic deformability sensor fabrication

The cell deformability sensor was designed in a layout editor and printed on a transparent mask. The polydimethylsiloxane (PDMS) replica was cast out from the SU8 mold. The casting mold was fabricated by a standard double layer lithography process on a 4-inch silicon wafer. SU8 photoresist with a thickness of 5 μm and 25 μm were used for the micropore area and loading channel area, respectively.

The Au/Cr electrodes (20 nm adhesive Cr layer and 80 nm Au layer) were evaporated on cover glass (thickness ~ 130 μm, Ted Pella) through a laser machined Polymethylmethacrylate (PMMA) shadow mask. To enhance the signal-to-noise ratio, the microelectrodes were positioned close to the micropore area. The PDMS replica was permanently bonded to the cover glass through oxygen plasma treatment.

4.4. Device characterization

A mixture of polystyrene microbeads with diameters of 5 µm and 10 µm (with a concentration of 1×10^5/ml and 3×10^4/ml, respectively) were used to validate the microfluidic device and the testing apparatus (Figure 4-1). Figure 4-2a shows the current trace for the mixed microbeads. Figure 4-2b shows the scatter plot and the histogram of the dwell time versus current dip amplitude (*ΔI*). Two separate populations can be clearly observed, representing the two different sized microbeads. The percentage of each polystyrene beads measured from the device was consistent with the pre-mixed ratio. This confirmed the functionality of the microfluidic device and the testing apparatus.

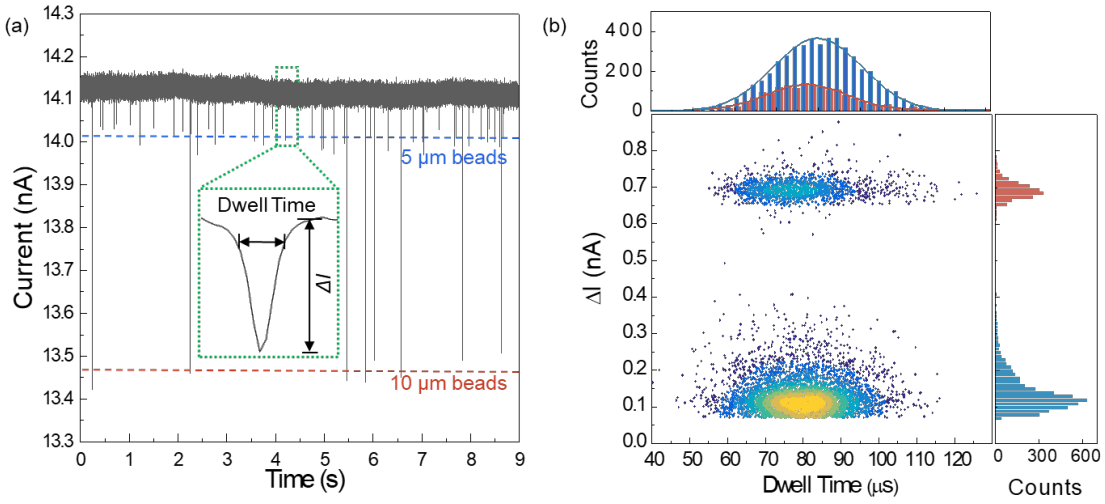

Figure 4-2: (a) Current traces measured with the mixed microbeads of 5 µm and 10 µm in diameters. (b) The scattering plot and the corresponding histogram for the measurement.

4.5. Differentiating ring stage *Pf-iRBCs* and *hRBCs*

To validate the microfluidic sensor for differentiating ring stage *Pf*-iRBCs and hRBCs, the ring stage *Pf*-iRBCs at 12% parasitemia and the control pure hRBCs were tested. To prepare the *Pf*-iRBCs, we synchronized the cultured parasite with 5% D-sorbitol to ensure the ring-stage. Prior to the electrical sensing measurement, 12% parasitemia was confirmed by standard Giemsa staining thin smear microscopy method. A mixture of *Pf*-iRBCs and uninfected RBCs were mixed with 1× phosphate buffer saline (PBS) for electrical measurement. The sample loading pressure applied to the microfluidic device was 1-1.5 psi (corresponding to a flow rate of ~180 μm/ms), leading to a measurement throughput ~500 cells /s in our devices.

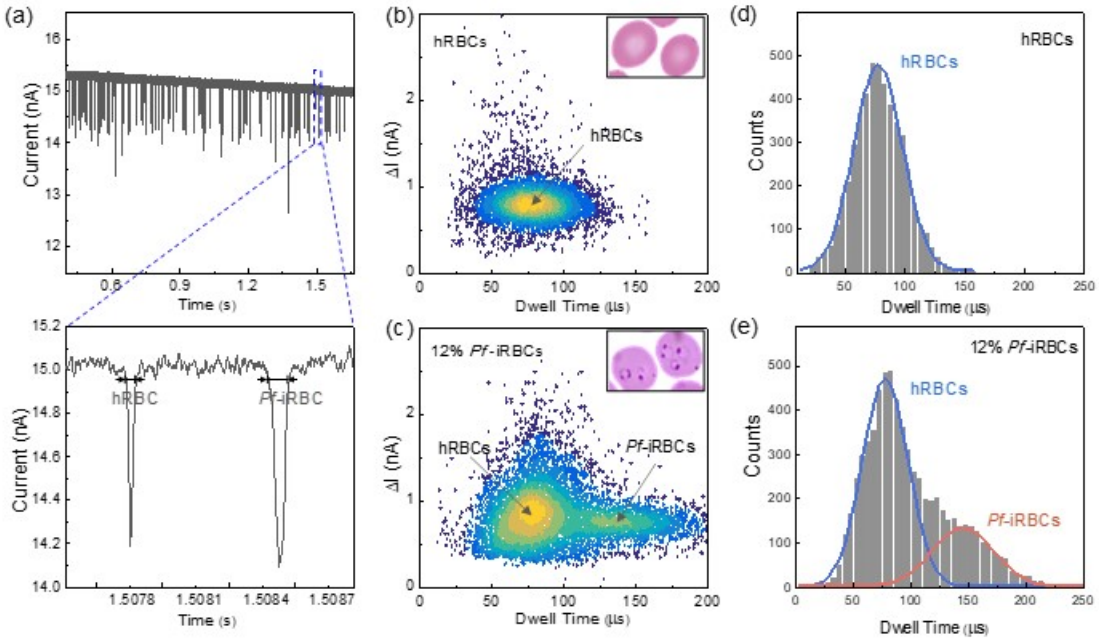

Figure 4-3: The current trace for the *Pf*-iRBC sample at 12% parasitemia. (b)-(c) The scattering plot of dwell time and current dip for the pure RBC sample (b) and the *Pf*-iRBC sample at 12% parasitemia (c). (d-e) Histogram plot of dwell time for the pure RBC sample (d) and the *Pf*-iRBC sample at 12% parasitemia (e).

Figure 4-3a shows a typical current trace, where the translocation time and the current dip for every single cell can be extracted. Figure 4-3b shows the scattering plot of the dwell time and current dip for the pure RBCs (100% hRBCs), while Figure 4-3c shows the case for the sample at 12% parasitemia (i.e., ~12% *Pf*-iRBCs and ~88% hRBCs). A clear two populations were shown in Figure 4-3c, representing the *Pf*-iRBCs and hRBCs in samples at 12% parasitemia.

4.6. Parasitemia quantification

The microfluidic cell deformability sensor can not only qualitatively differentiate ring stage *Pf*-iRBCs and hRBCs, but also quantitatively determine the parasitemia. With 2× serial dilution of the *Pf*-iRBCs sample at 12% parasitemia, parasitemias of 12%, of 6%, 3%, 1.5%, 0.75%, 0.375%, and 0.1875% were prepared. These samples were tested with the microfluidic cell deformability sensor, and translocation time for each parasitemia sample exhibited a similar two-peaked normal distribution.

Figure 4-4 shows the scattering plot of the transit time and current dips for ring *Pf*-iRBCs samples' translocation events. A decreasing population with larger translocation time was observed when the sample parasitemia was reduced (Figure 4-4a). The percentage of the *Pf*-iRBC population in each sample was obtained by counting the cells of translocation time below a certain threshold. The threshold was determined by the mean value plus three times sigma of the control sample with pure hRBC (a Gaussian distribution). The parasitemia determined by this method was benchmarked with that determined by the microscopy (Figure 4-4b). The agreement between these two methods demonstrates the microfluidic cell deformability sensor can be used for parasitemia quantification. More than 30,000 RBCs can be analyzed within 1 min. As a comparison, the microfluidic cell deformability sensor is much faster than the microscopy with speed ~ 5 mins/slide [112].

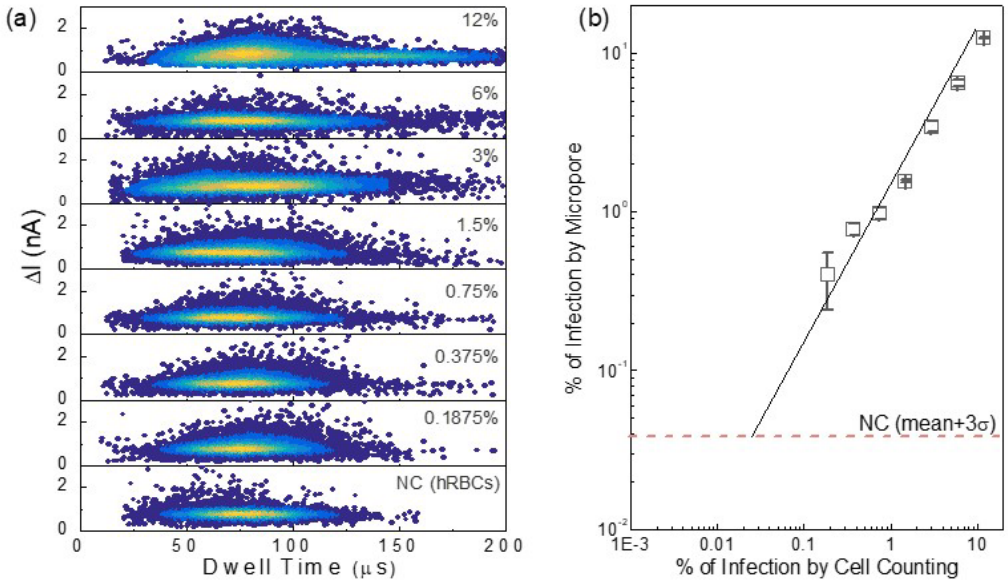

Figure 4-4: (a) Scattering plot of dwell time versus ΔI for RBCs with parasitemia of 12%, of 6%, 3%, 1.5%, 0.75%, 0.375%, 0.1875% and the healthy RBCs. (b) Parasitemia determined by the microfluidic deformability sensor versus the parasitemia determined by the microscopy.

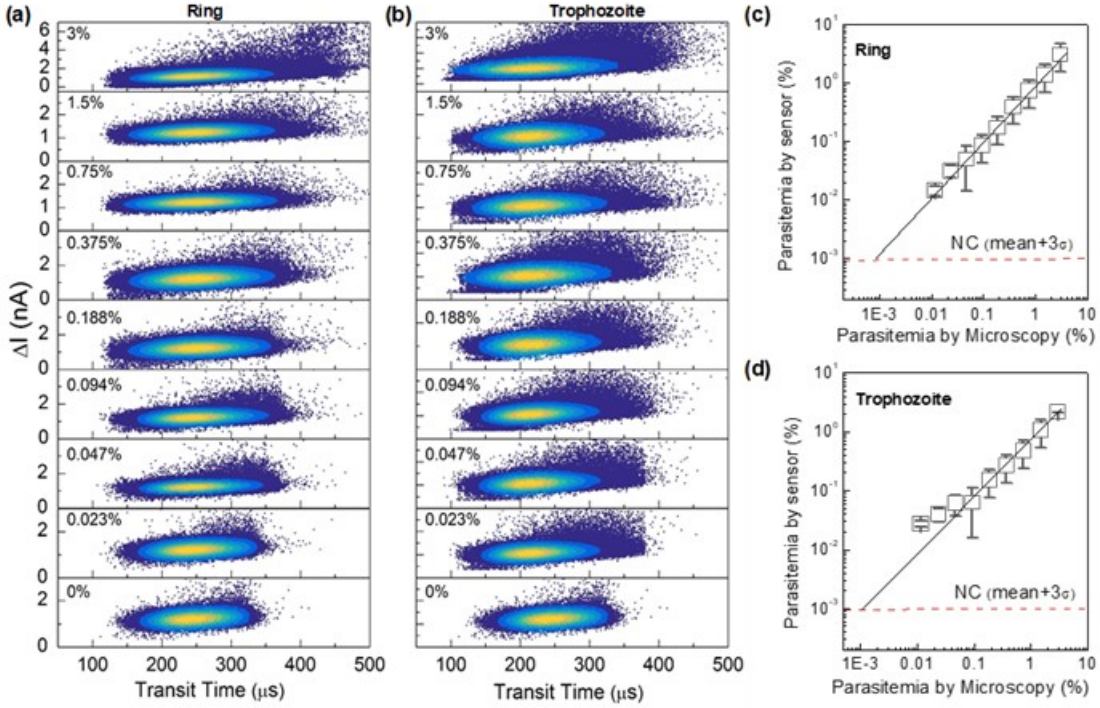

Figure 4-5: Scattering plot of transit time versus ionic current dip for the *Pf*-RBCs with various parasitemia for (a) ring and (b) trophozoite *Pf*-iRBC. Corresponding parasitemia determined by the microfluidic deformability sensor and the microscopy method for (c) ring and (d) trophozoite *Pf*-iRBC. Reprinted from ref. [127], Copyright 2017, with permission from Elsevier.

Yang et al. further explored the qualitative ability of the deformability sensor with trophozoite stage *Pf*-iRBC [127]. The more population with longer transit time was observed as parasitemia increases (Figure 4-5b). The parasitemia determined by deformability sensor and microscopy agreed to each other with excellent linearity (R^2>98%, Figure 4-5c & d). Such results further confirm the parasitemia quantification ability with the trophozoite stage *Pf*-iRBC.

4.7. The ability for malaria stage differentiation

In the intraerythrocytic cycle, the *P. falciparum* parasites evolve from the ring stage to the trophozoite and finally to the schizont stage. During this process, the stiffness of the red blood cells increases monotonically from 8 μN/m to 16 μN/m at the ring stage and finally to 53 μN/m at the schizont stage [114]. Therefore, the dwell time of the *Pf*-iRBCs is expected to increase as parasites develop into late stages. We performed the translocation time analysis for the *Pf*-iRBCs at different stages using the microfluidic sensors. Figure 4-6 shows the dwell time for three different samples, (1) the healthy RBCs (Figure 4-6a-b), (2) the mixture of healthy and ring-stage-only *Pf*-iRBCs (Figure 4-6c-d), and (3) the mixture of healthy and ring, trophozoite, and schizont stage *Pf*-iRBCs (Figure 4-6e-f). A clear right-shift of the dwell time can be observed from Figure 4-6a to Figure 4-6e. Sub-populations of *Pf*-iRBCs at different stages were distinguishable by multi-peak Gaussian fitting of the dwell time distribution. This observation is consistent with the fact that *Pf*-iRBCs become stiffer as parasites develop into late stages. As a result, the red blood cell deformability could be used as a potential mechanical biomarker to differentiate malaria at different stages.

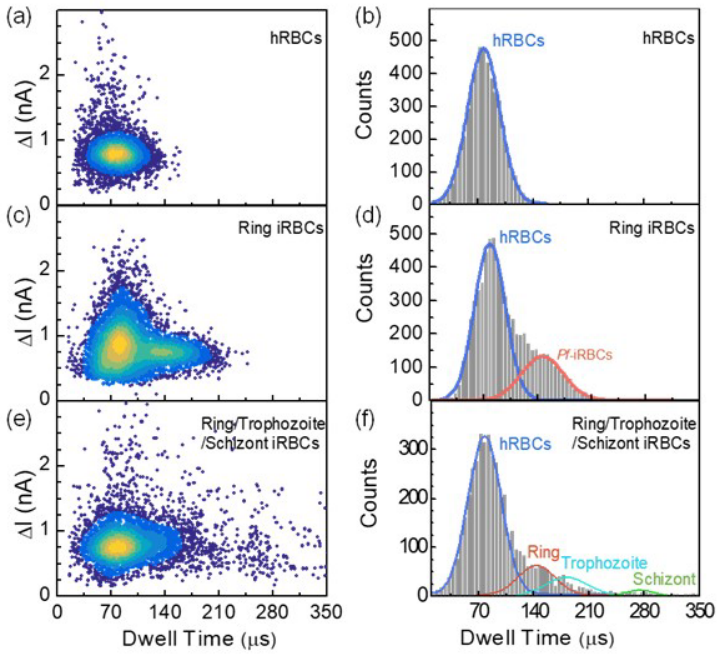

Figure 4-6: Scattering plot of the current dip versus the translocation time and the corresponding histograms for (a) healthy RBCs, (b) 12% infected ring stage iRBCs, and (c) a mixture of the ring, trophozoite, and schizont stage parasites in RBCs.

To further evaluate the sensor's stability to monitoring the stiffness change during an intraerythrocytic cycle (~ 48 hours), Yang et al. continuously monitored the 2% *P. falciparum* parasites with the interval of 5~8 hours [127]. The collected transit time data was used to analyze the iRBCs deformability and parasitemia evolution and to benchmark with the microscopy method. A right-shift of the transit time can be observed as culture time increases, implying the parasite evolution from the ring stage and to the late stage of trophozoite and schizont (Figure 4-7**a**). The result is again consistent with the fact that *Pf*-iRBCs become stiffer as parasites grow during the intraerythrocytic cycle. However, the clear turning point from stage to stage was not observed during the intraerythrocytic period (Figure 4-7**a**). This is probably because the asynchronous *Pf*-iRBCs contained various stages of *Pf*-iRBCs at a specific time [130]. This also explains the gradual parasitemia increase during the intraerythrocytic cycle (Figure 4-7**b**). Ideally, parasitemia would

not increase for one proliferation cycle (~48 hr). However, increases in parasitemia were also observed with thin smear microscopy with high linearity (R^2>96%, Figure 4-7**c**) because the asynchronous *Pf*-iRBCs already completed the first proliferation cycle and infected more hRBCs [130].

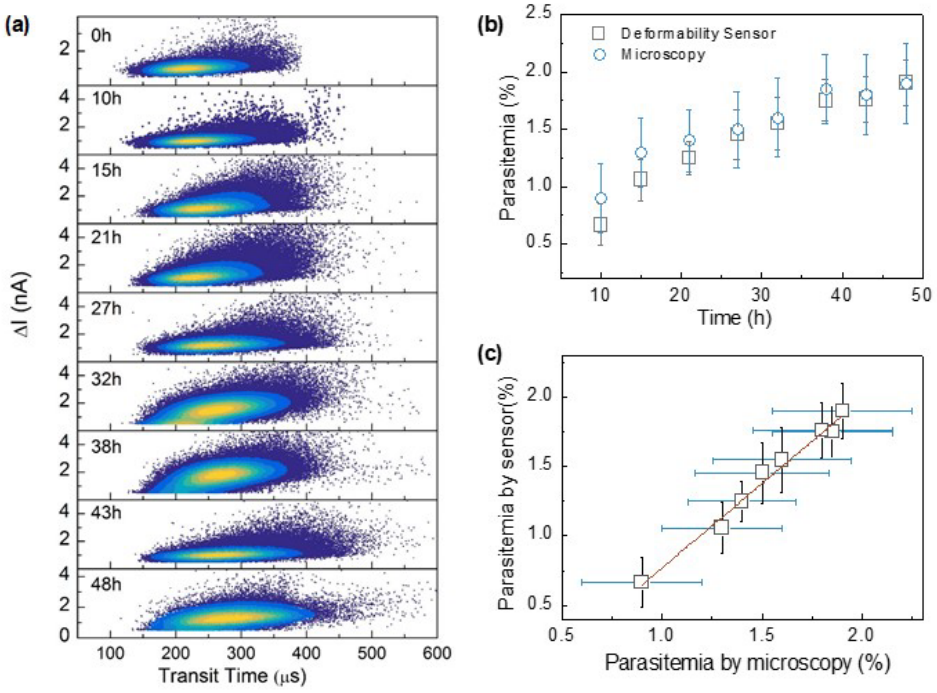

Figure 4-7: The analysis for the *Pf*-iRBCs at different stages during the intraerythrocytic cycles. (a) Scattering plot of transit time versus ionic current dip for the *Pf*-iRBC during the intraerythrocytic cycle at various time spots. (b) The parasitemia quantified by the deformability sensor and microscope during the intraerythrocytic cycles. (c) Comparison of parasitemia between the deformability sensor and the microscope. Reprinted from ref. [127], Copyright 2017, with permission from Elsevier.

4.8. Summary

This work demonstrated an electrofluidic sensor for accurate and quantitative parasitemia measurements. This microfluidic device uses the deformability as the mechanical biomarker to differentiate the healthy RBCs and *P. falciparum*-infected RBCs. The electrofluidic sensor was able to quantify the parasitemia in a very short amount of time (<1 min) by analyzing a large population of red blood cells (>30 k) in high throughput (~ 500 cells/s) manner. Moreover, the electrofluidic sensor is able to differentiate various malaria stages. As compared to the microscopy and flow cytometry, this microfluidic device would allow for label-free, rapid, and low-cost malaria parasitemia quantification and stage determination.

Chapter 5 Deformability-Activated Cell Sorting (DACS)

Gametocyte maturation in *P. falciparum* is a critical step in the transmission of malaria [21, 22], thus realizing gametocytes in the bloodstream would be a powerful tool for surveillance in malaria elimination setting [21]. However, one of the biggest challenges to recognize gametocyte in the blood is its rarity.

In Chapter 4, we demonstrated that mechanical properties could be an excellent label-free biomarker for recognizing malaria-infected RBCs. However, the current deformability measurement device has not been integrated with deformability-based cell sorting, which is essential for concentrating gametocytes. In this chapter, we will discuss the first single-particle-resolved cytometry-like deformability-activated cell sorting (DACS) in the continuous flow on a microfluidic chip. Compared with existing deformability-based sorting techniques, the microfluidic device presented in this work measures the deformability and immediately sorts the cells one-by-one in real-time. It integrates the transit-time-based deformability measurement and active hydrodynamic sorting onto a single chip. We identified the critical factors that affect the sorting dynamics by modeling and experimental approaches. We found that the device throughput is determined by the summation of sensing, buffering, and sorting time. The total time of ~100 ms is used for analyzing and sorting a single particle, leading to a throughput of 600 particles/min. We synthesized poly (ethylene glycol) diacrylate (PEGDA) hydrogel beads as the deformability model for device validation and performance evaluation. A deformability-activated sorting purity of 88% and an average efficiency of 73% were achieved.

5.1. Introduction to deformability-based sorting

Gametocyte concentration is informative for predicting parasite transmission potential to mosquito [131]. Assessing the number of parasite present in the bloodstream is of interest to identify the source of gametocyte carriers and to disrupt malaria transmission [132]. While molecular detection of gametocytes could be a possible approach, genetic characterization is often limited because gametocytes comprise a small fraction of the total parasites in the bloodstream [21]. Realizing a fraction of gametocytes in the blood requires separation from asexual parasites and enrichment. In addition to gametocyte density, gametocyte production time and their lifespan are critical factors affecting malaria transmission [133]. Therefore, a reliable biomarker that can sort gametocyte, as well as monitor gametocyte production, is urgently needed.

Several studies reported that matured stage gametocytes are more deformable than the asexual stage parasites-invaded RBCs [134, 135]. This implies that cell deformability can be used as a label-free biomarker for gametocyte separation and enrichment. Various microfluidic deformability-based passive particle separation devices have reported (e.g., inertial microfluidics [7], pinch flow fractionation [136, 137], acoustofluidics [138], and deterministic lateral displacement [114, 139, 140]). While these passive methods are effective and have good throughput, the quantitative deformability information of an individual cell is inaccessible (see Table 5-2). A fluorescence-activated cell sorting (FACS)-like device that measures the single particle deformability in real-time and actively sorts the particles with a particular deformability property is highly desirable and has yet to be developed. In recognition of this critical need, we here demonstrated a microfluidic single-particle-resolved, cytometry-like deformability-activated sorting device. The device seamlessly integrates single-particle deformability sensing and active hydrodynamic sorting into a single microfluidic chip.

Table 5-1: Summary of the microfluidic deformability-based cell sorting devices.

	Micro-filtration	**Diagonal Ridge**	**DLD***	**Inertial**	**RCT***	**Ratchets**	**Opto-fluidics**	**Acousto-fluidics**	**Hydro-dynamics**
Separation type	Bulk	Bulk	Bulk	Bulk	Bulk	Bulk	Active	Active	Active
Separation mechanism	size exclusion	cell compression	streamline around micropost array	lift forces, secondary flows	trapping	Irreversible ratchet mechanism	optical force (refractive index difference)	acoustic radiation force	Hydro-dynamic push-pull
Separation criteria	size, deformability	size, deformability	size, deformability	size, deformability	size, deformability	size, deformability	Deform-ability	Deform-ability	Deform-ability
Throughput (cells/min)	10^4	10^4	10^7	10^6	10^5	10^3	1	10^3	600
Purity (%)	80 - 99	65 – 99	90 - 98	80	-	62 – 95	73 – 75	50.3 - 91.3	~ 88
Enrichment (fold)	140 - 232	185	-	100 - 300	183	210	~3	~10	~8
Ref.	[1-3]	[4, 5]	[6]	[7, 8]	[9-12]	[13-16]	[17]	[18]	[19]

DLD: deterministic lateral displacement
RCT: resettable cell trapping

Compared to existing deformability-based sorting techniques, the demonstrated microfluidic device measures the deformability and immediately sorts the deformable particles one-by-one in real-time. The deformability is measured by evaluating the transit time during which an individual particle squeezes through a microscale constriction [141], while the active particle sorting is implemented by hydrodynamic flow control. We studied the factors affecting the sorting dynamics in a continuous flow by carrying out both modeling and experiments. To validate the device and evaluate its performance, we synthesized PEGDA hydrogel beads as the deformability model cells. We demonstrated a sorting purity of 88% and an efficiency of 73%. We achieved single-particle processing (analyzing and sorting) time of 100 ms, corresponding to a throughput of 600 particles/min. We envision that the real-time deformability-activated cell sorting (DACS) can be used to increase parasite detectability on gametocytes that commonly circulate at low densities.

5.2. Working principle

Figure 5-1A shows the schematic of a device that integrates single-particle deformability sensing and sorting into a continuous-flow microfluidic chip. A buffering region was included to reduce the crosstalk between the consecutive sensing and sorting. The deformability sensing was indirectly performed by the previously validated constriction-based transit time measurement [118, 141-144]. Briefly, soft particles take less time to squeeze through the sensing pore, while rigid particles take more time (Figure 5-1B). Therefore, the transit time is an indicative measurement of the particle deformability. Immediately after measuring the particle transit time, a threshold-based triggering signal was used for sorting.

The sorting was achieved by a hydrodynamic push-pull mechanism through pneumatic control. Hydrodynamic sorting minimizes the potential damage to cell viability and requires no specific

buffer solutions [145, 146]. Two identical sorting channels (S1 and S2) were filled with buffer solutions and connected to two independently controlled high-speed solenoid valves (V1 and V2, response time ~8 ms). Both valves were connected to the same pressure source (typically approximately 0.3 psi). The pressure that drives each sorting channel was mediated by a solenoid valve to generate digital V1-V2 combinations of 00, 01, 10, and 11 (note that 00 is not used since the residue pressure is not well defined when the valve is off). Both valves were normally on (case of 11); thus, the default flow in the sorting region was focused on the middle of the channel and directed to the waste outlet (middle case in Figure 5-1C). If the transit time was shorter than the sorting threshold (soft particle), V1 was activated (turned off, status 0) by a voltage pulse to temporally direct the streamlines towards outlet 1 (top case in Figure 5-1C). The opposite action was taken for rigid particles (bottom case in Figure 5-1C).

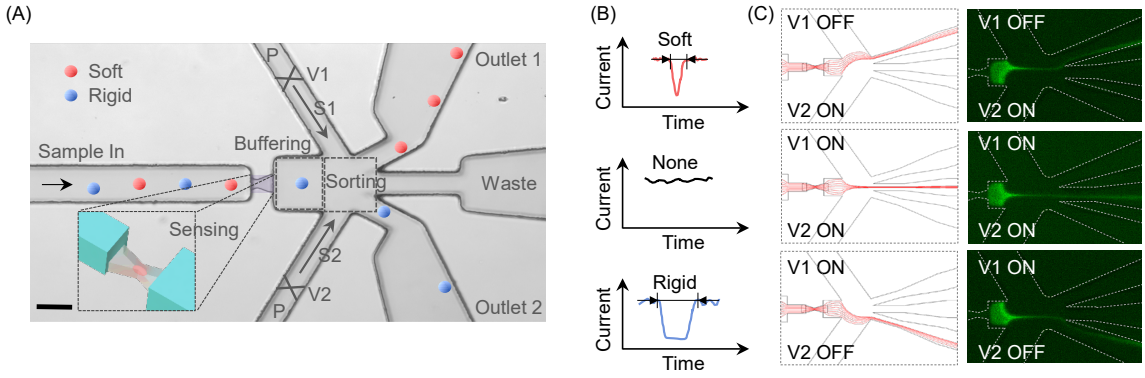

Figure 5-1: Deformability-activated particle sorting device principle. (A) A top-down image of the microfluidic chip with various functional parts (scale bar: 50 μm). Two sorting flows (S1 and S2) were connected to the same pressure source and independently controlled by fast-response solenoid valves (V1 and V2). The inset illustrates the micro-constriction structure for deformability sensing. (B) Transit time-based deformability measurement. (C) Hydrodynamic sorting mechanism by programming the solenoid valves V1 and V2. The left and right columns are the simulated streamlines and the observed fluorescent dye (1 mM calcein) under different combinations of pneumatic valve status.

5.3. DACS instrumentation

5.3.1. Microfluidic DACS device fabrication

The photomask was designed using CAD software and printed on a transparent film. The SU-8 mold was fabricated by a two-step lithography process on a 4-inch silicon wafer. The regions with heights of 80 μm (loading/buffer/sorting area) and 15 μm (constriction micropore area) were created using SU-8 2050 and 2010, respectively, and confirmed with a profilometer. The designed constriction pore width was 14 μm, optimized for our synthesized Poly(ethylene glycol) diacrylate particles (diameter of ~14 μm). A 10:1 w/w mixture of base and curing agent for polydimethylsiloxane (PDMS) (Sylgard, Dow Corning, USA) was prepared. It was optional to add Triton X-100 (EMD Millipore) with a volume ratio of 0.5% to increase the wettability of the microfluidic channels [147]. Before bonding, fluidic inlets and outlets were punched using a stainless needle (diameter of 0.75 mm). The resulting PDMS stamps were permanently bonded to glass slides (100 μm thickness, Ted Pella) by oxygen plasma treatment.

To avoid the double-layer capacitance effect, we used custom-built Ag/AgCl electrodes to measure electrical signal. Ag/AgCl electrodes were fabricated by chloriding 0.375 mm Ag wires (Warner Instruments, Hamden, USA) in a 1 M KCl solution. A small hole was punched from the outside wall of the tygon tubing, and Ag/AgCl electrodes were threaded through this hole into the inside of the tube, followed by epoxy sealing. This customized tubing provides both electrical and fluidic access to the microfluidic device.

5.3.2. Testing Apparatus

Transit-time-based deformability sensing. The electrical measurement was performed inside a customized Faraday cage to provide shielding from environmental noise. A syringe pump (Harvard Apparatus PHD 2000) was used to introduce the sample into the microfluidic chip. A total of 500 mV was applied across the sensing pore, and the ionic current was continuously monitored by a trans-impedance amplifier (DHPCA-100, FEMTO, Germany). The analog output of the amplifier was sampled at 1 MHz with a 16-bit DAQ card (NI PCIe-6351, National Instruments). The data were processed online using a real-time algorithm (LabVIEW) to extract the particle transit time and the current dip when individual particles translocate the micropore (Figure 5-2).

Deformability triggered sorting. Electrically activated 3-way normally open solenoid valves (S10MM-31-24-2, Pneumadyne) were used for pneumatic control. Both solenoid valves were connected to a piezoelectric micropump (Elveflow AF1, France) with constant pressure (usually from 0.3 to 0.5 psi). The solenoid valves were turned off through a DAQ-generated pulse, triggered by comparing the transit time against a gating threshold time. The pulse duration was set to 40 ms. Note that sensing and sorting occurred in real-time through custom-built LabVIEW pr(Figure 5-2).

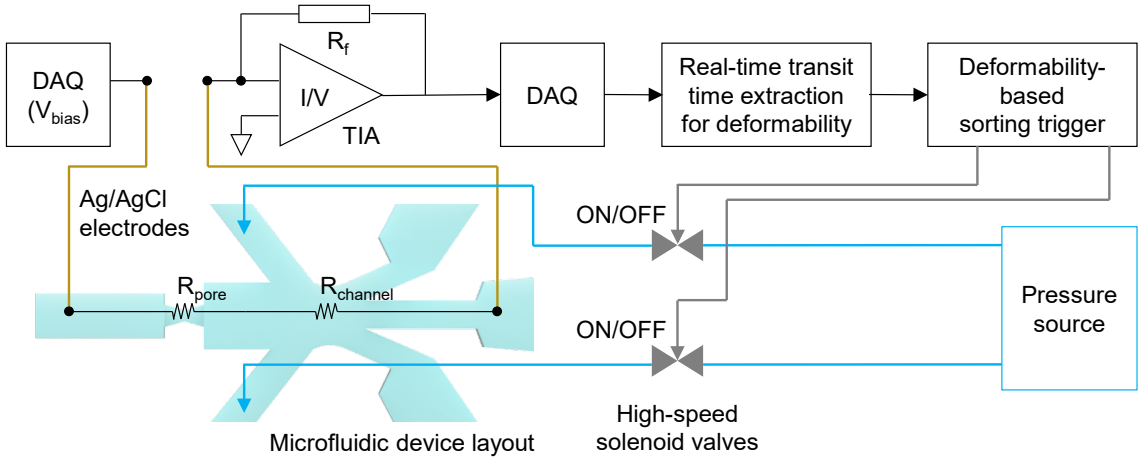

Figure 5-2: Detailed system diagram for the deformability activated sorting device. The real-time deformability sensing algorithm detects the particle transit time within a rolling sampling window, which is used to trigger a fast-switching solenoid valve for sorting.

5.4. Numerical simulation

5.4.1. Computational domain of the simulation model

A two-dimensional computational domain (Figure 5-3A) was used to explore the effect of the parameters (*e.g.*, sample flow rate, sorting pressure, the spacing between particles, and pressure relaxation time) on the sorting performance. The Navier-Stokes equations (Eq. 1) and particle tracing equations (Eq. 2) were used to model the particle motion in the microfluidic channel network during the hydrodynamic actuation.

$$\rho_f \frac{\partial U}{\partial t} = \nabla \cdot \left[-pI + \mu\left(\nabla \mathrm{U} + (\nabla \mathrm{U})^{\mathrm{T}}\right)\right]$$

$$\nabla \cdot U = 0 \text{ (Incompressible flow)} \qquad \text{(Eq. 1)}$$

where ρ_f is the fluid density, μ is dynamic viscosity, t is time, U is the fluid velocity, p is applied pressure, and I is identity tensor. Constant volume flow rate boundary condition was used at the sample inlet. The time-dependent pressure was applied in parallel sorting flows based on the sorting configuration. To include hydrodynamic impedance (resistance and capacitance) in the model, a characteristic time τ (pressure relaxation time) was added in the time-dependent pressure profile. The atmospheric pressure is applied as the outlet boundary condition.

The particle motion was explained by the drag force exerted on the particle. The governing equation for particle tracing is as follows:

$$m_p \frac{dv_p}{dt} = F_D$$

$$F_D = \frac{1}{\tau_p} m_p (U - v_p)\,,\ \tau_p = \frac{\rho_p d_p^2}{18\mu} \qquad \text{(Eq. 2)}$$

where F_D is the drag force, v_p is particle velocity, m_p is particle mass, ρ_p is particle density, and d_p is particle diameter. The particles were assumed to be a circular shape with a density of 1050 kg/m^3 and a diameter of 5 µm.

The particle spacing time T_s is related to the sample concentration as $C = 1/WLH$, where W is the width, L is length, and H is the height of the channel (Figure 5-3B). The velocity of the particle V_p is $V_p = L/T_s$, where T_s is time spacing between adjacent particles. V_p can also be expressed in terms of volume flow rate as $V_p = \dot{V}/(WH)$, where $\dot{V}$ is the volume flow rate. Therefore, the particle spacing time T_s can be written as $T_s = 1/(C\dot{V})$.

Table 5-1 summarizes all parameters and boundary conditions used in this study.

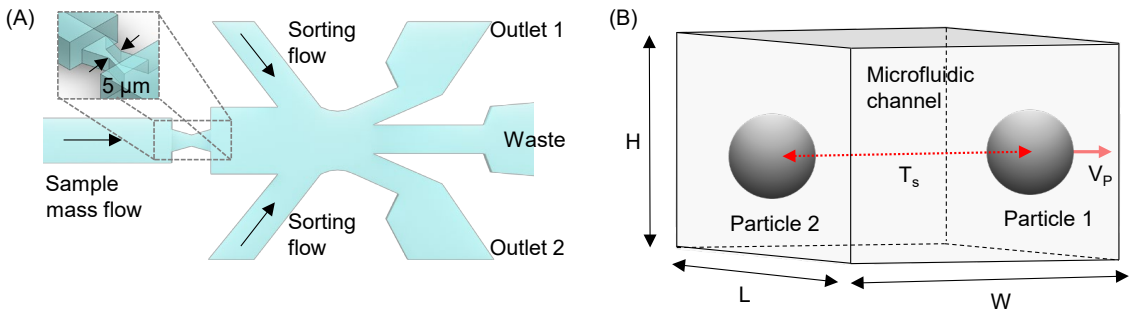

Figure 5-3: (A) Computational domain of the simulation, (B) Illustration of two adjacent particles in a continuous flow. Ts represents time spacing between particles, V_p is the particle velocity in the microfluidic channel. The minimum Ts (T_{smin}) determines the maximum sorting throughput ($1/T_{smin}$). The constant Vp is assumed for the particles traveling on the identical streamline. H, L, and W are height, length, and width of the fluidic channel in the sorting area.

Table 5-2: Effective sorting parameters used in the numerical simulation.

Symbol	Parameter	Value	Unit
μ_f	Fluid dynamic viscosity	8.90 × 10−4	Pa.s
ρ_f	Fluid density	997	Kg/m^3
ρ_p	Particle density	1050	Kg/m^3
D_p	Particle diameter	5	µm
$\dot{V}$	Volume flow rate	Variable	µl/h
p	Pressure for sorting flow	Variable	psi
T_s	Time interval between particles	Variable	Sec
T_{smin}	Minimum T_s	Variable	Sec
T_{valve}	Valve response time	Variable	Sec
T_{sens}	Sensing time window	Variable	Sec
τ	Pressure relaxation time	Variable	Sec

5.4.2. Factors affecting consecutive sensing and sorting under the worst-case scenario

While the device principle is straightforward, it involves many coupled processes that need to be synchronized in the continuous flow. To gain deep insight into the proper experimental setup and ensure device reliability, we set out to study the device sorting dynamics when operated under the worst-case scenario. The worst-case scenario is defined as the case in which consecutive particles are alternately directed to two sorting outlets, that is, the 1st and 3rd particles are directed to outlet 1, while the 2nd and 4th particles are directed to outlet 2, and so on. In this case, it takes the longest time to deflect the flow to achieve correct sorting.

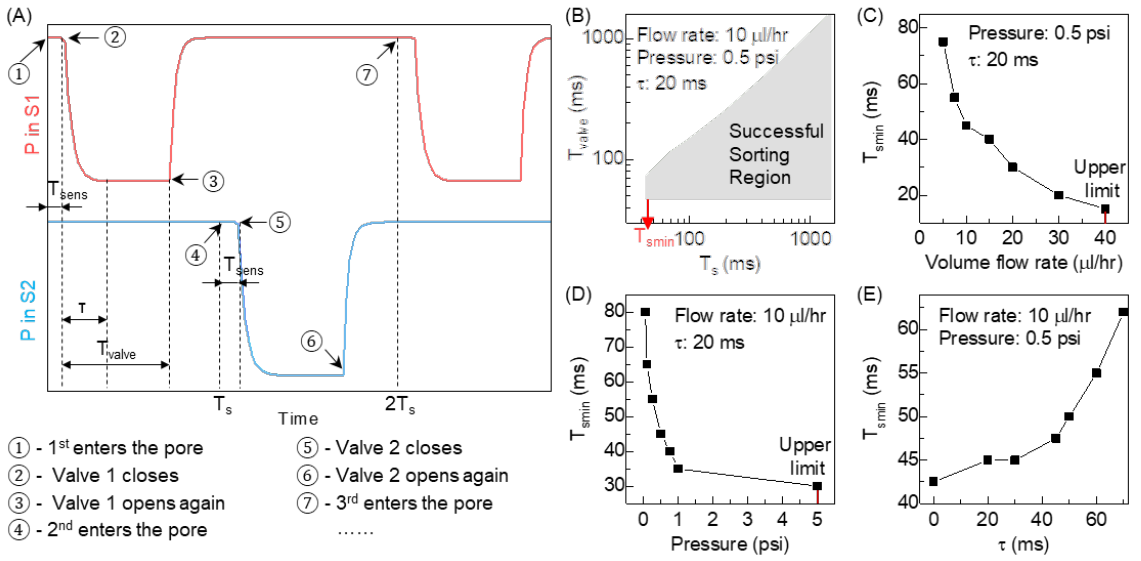

Figure 5-4: Factors affecting consecutive sensing and sorting under the worst-case scenario. (A) Time sequence of the pressure profile for driving the two sorting flows (red for S1 and blue for S2) under the worst-case scenario. T_{sens}: sensing time, τ: system relaxation time, T_{valve}: valve pulse off time, and T_s: particle spacing time. (B) Successful sorting regions in the T_{valve} - T_s plot. Successful sorting is defined as the case when the device can handle the worst-case scenario, that is when consecutive particles are alternately directed into different outlets. $1/T_{smin}$ corresponds to the highest sorting throughput. (C) T_{smin} as a function of the sample flow rate. (D) T_{smin} as a function of the sorting pressure. (E) T_{smin} as a function of the system relaxation time.

Figure 5-4A shows the time-dependent pressure that drives the flow in the sorting channels S1 and S2. In this schematic, it was assumed that successive particles arrive at the sensing pore with a periodic interval T_s (time 1, 4, and 7). Specifically, at time 1, the first particle enters the sensing pore. It then takes a time span of T_{sens} to complete the deformability measurement. Note that T_{sens} should be longer than the intrinsic particle transit time to achieve a reliable measurement. At the end of the deformability sensing (time spot 2), V1 is pulsed off with a duration T_{valve}. This off-duration can be programmed by the triggering voltage pulse. Note that the pressure that drives the S1 channel does not immediately drop to zero when the valve is turned off. A relaxation time τ is always needed for the transition. This relaxation time comes from the hydrodynamic capacitance

in the system and the solenoid valve response time. At time 3, V1 resumes normal 'on' status. Again, the pressure that drives the S1 channel does not immediately jump to full pressure when the valve is turned on. After another relaxation time τ, the device is ready for the next particle. At time 4, the second particle enters the sensing pore, and similarly, V2 is closed off by the triggering pulse to direct this particle into the opposite outlet.

With the sequence shown in Figure 5-4A, we varied the simulation parameters and evaluated whether consecutive sorting could be successfully performed under the worst-case scenario (Figure 5-5). We examined different combinations of valve actuation time T_{valve} and particle spacing time T_s. Figure 5-4B illustrates the successful parameter region on the T_s - T_{valve} map with a sample flow rate of 10 μl/hr, sorting pressure of 0.5 psi, and τ of 20 ms. As shown in Figure 5-4B, there is a lower limit of T_{valve} for correct sorting regardless of the particle spacing time T_s. This lower limit of the valve pulse time is determined by the system relaxation time τ (usually 10-20 ms). This can be easily understood by the fact that T_{valve} shorter than τ will not lead to the required stable 'off' pressure for flow deflection. Figure 5-4B also shows that there is a lower limit of T_s (denoted by T_{smin}). This means that two successive particles cannot be too close to each other for sorting under the worst-case scenario. In addition, it is clear from Figure 5-4B that the upper limit of T_{valve} is dependent on T_s. This is not surprising since keeping the valve actuated longer than the particle interarrival time would lead to the particle being incorrectly sorted.

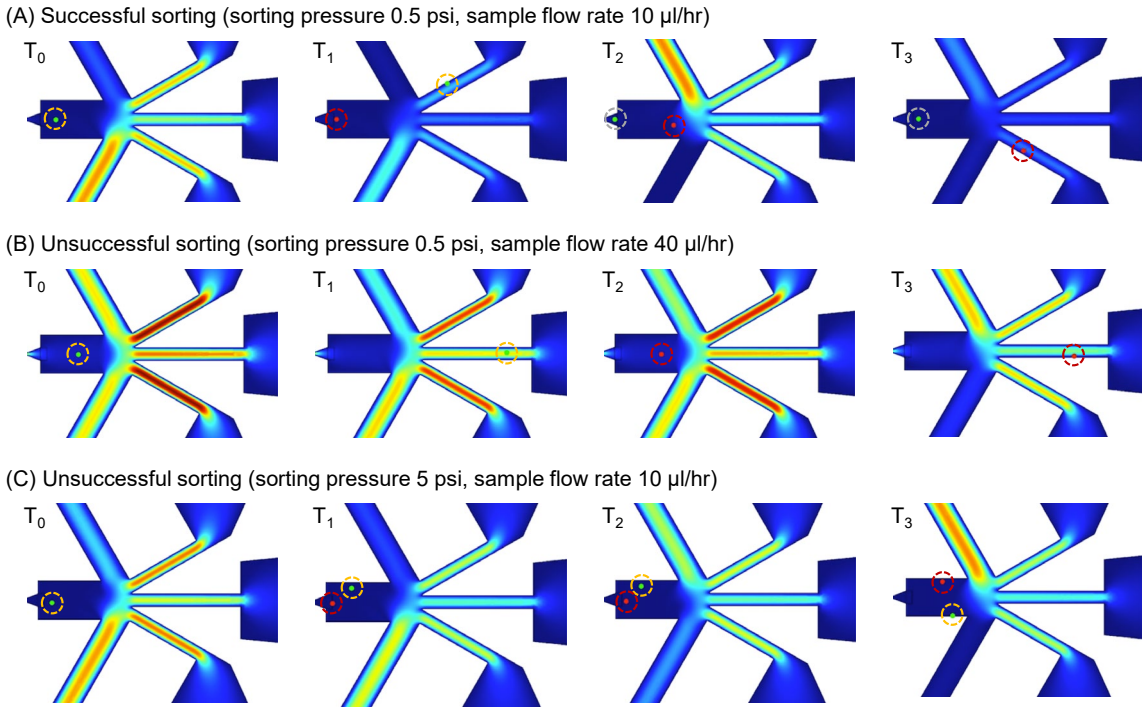

Figure 5-5: Simulation results of consecutive sorting with varying parameters. (A) Successful sorting of consecutive particles. (B) Unsuccessful sorting occurs because sorting cannot catch up with the fast appearing particles. (C) Unsuccessful sorting happens because excessive sorting pressure causes backflow.

The T_{smin} annotated in Figure 5-4B essentially determines the sorting throughput (*i.e.*, $1/T_{smin}$ is the highest achievable throughput). With the aim of improving the operation throughput, we studied the effect of the sample flow rate, sorting pressure, and system relaxation time on T_{smin}. Figure 5-4C shows that the throughput can be enhanced with a higher sample flow rate. However, the sample flow rate cannot be arbitrarily high since the sorting cannot catch up with the fast-appearing individual particles (Figure 5-5B). In our experiment, the sample flow rate was set to 10-20 µl/hr. Figure 5-4D shows that the throughput can also be enhanced by using a high sorting pressure. This is because the high pressure leads to high flow velocity in the sorting channel, which can deflect the particle faster at the sorting junction. However, there is an upper limit of the sorting pressure, beyond which particle backflow occurs (Figure 5-5C). In our experiment, the sorting pressure was

set to 0.3-0.5 psi. Figure 5-4E shows that a smaller system relaxation time τ can help enhance the throughput. Therefore, use of a fast-response solenoid valve and reduction of the system capacitance are preferred. Our system has a relaxation time of approximately 10-20 ms.

5.5. Validation of hydrodynamic sorting by order

To experimentally validate the simulation results, we prepared a polystyrene bead (Polyscience) sample of concentration 10^6/ml with 1 mM calcein and 0.05% Tween-20 added and buffered in 1× PBS. The calcein dye was added for flow streamline visualization. The sorting algorithm was modified such that the beads were sequentially sorted to the opposite outlets based on their passing order in the sensing region. For example, the 1st, 3rd, and 5th would be directed to outlet 1, while the 2nd, 4th, and 6th would be directed to outlet 2. The sample flow rate was 10 μl/hr, the sorting pressure was 0.5 psi, and the trigger pulse was set to 40 ms for the solenoid valve (T_{valve}=40 ms). The sorting dynamics were recorded using a high-speed CCD camera with a frame rate of 125 fps. Figure 5-6 shows the sequential particle deflection in the intended sorting sequence. Under the default condition, the sorting flow pinched the sample flow (bright streamlines) into the center of the channel and was directed towards the waste outlet. To deflect the 1st and 3rd beads, V1 was closed, resulting in bead deflection towards outlet 1. Reversing the valve configuration drove the 2nd and 4th beads into outlet 2. This directional motion was described in the Zweifach-Fung effect [148], where the particle moved towards the branch with a higher flow rate at the bifurcation. Guided by the simulation results, this sorting-by-order experiment laid out the correct sorting parameter region and paved the way for the following deformability-activated particle sorting.

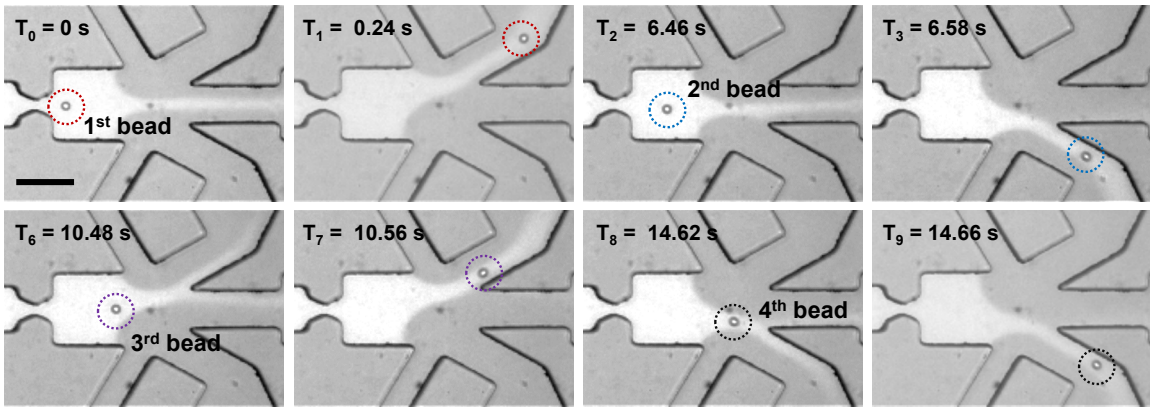

Figure 5-6: Validation of the hydrodynamic sorting by order. A single-layer microfluidic device (height and width at the constriction region are 40 and 18 µm, respectively) is used to test the particle deflection. The frames shown are in sequence. Fluorescent dye (bright area) was used to visualize the sample flow deflection (scale bar: 100 µm).

5.6. Synthesis of PEGDA hydrogel beads by droplet microfluidics

Poly(ethylene glycol) diacrylate (PEGDA, MW 700 Da) was first dissolved in deionized water to yield the desired concentration (w/w). The thermal initiator Ammonium persulfate (APS, VWR) was added to the PEGDA precursor solution at a 10% (w/v) concentration. The resulting solution was used as an aqueous phase to synthesize water-in-oil microdroplets (Figure 5-7). The oil phase consists of mineral oil (Sigma-Aldrich) and 1% Span 80 (w/w). The aqueous phase and oil phase were introduced using a piezoelectric micropump (AF1, Elveflow, France) with pressures set at 2.3 psi and 4.5 psi, respectively. The synthesized droplets were harvested into a 1.5 ml tube and incubated at 40 °C for 12 hours for polymerization. To remove the oil, we performed sequential washing steps, using PBS with 0.05% Tween-20. Finally, the bead-containing solution was filtered using a cell strainer with a mesh size of 15 µm (43-50015-03, pluriSelect, Germany). After filtration, the uniform-sized beads were confirmed with the microscope (Figure 5-8).

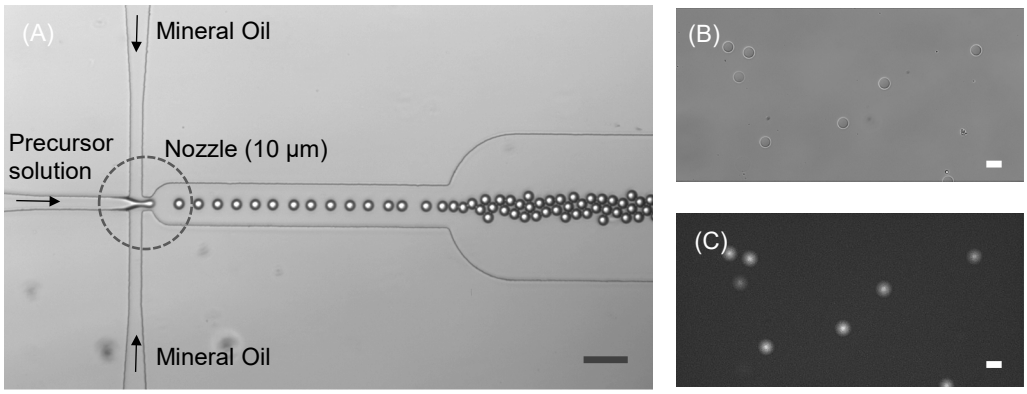

Figure 5-7: Synthesis of uniformly sized PEDGA hydrogel microbeads using microfluidic droplet generator. (A) Uniform-sized water-in-oil emulsion (scale bar: 50 μm). (B) Synthesized PEDGA hydrogel microbeads under bright-field microscopy (scale bar: 20 μm). (C) fluorescence image of PEDGA hydrogel microbeads (scale bar: 20 μm).

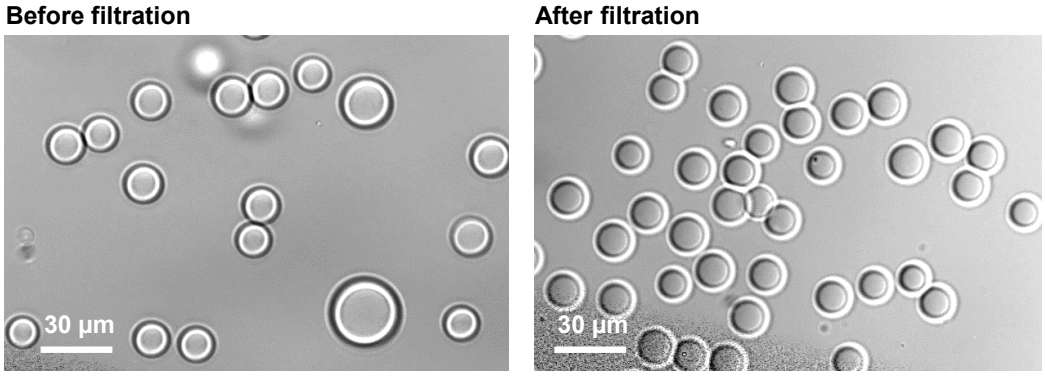

Figure 5-8: Microscope images of in-house fabricated 12.5% PEGDA hydrogel beads. The bead size variation before the filtration comes from the pressure variations in the microfluidic droplet generator chip. After the filtration, uniform beads with diameters of ~14 μm were obtained.

5.7. PEGDA hydrogel microbeads as deformable gametocyte models

For various deformability studies, a major challenge is the lack of model particles with defined deformability properties. While agarose beads were previously used for this purpose [149], we were not able to make stable agarose beads in PBS for long-term measurements (Figure 5-9). To address this issue, we switched to alternative materials. It is well known that the extent of polymeric network cross-linking is related to the material mechanical properties [150, 151]. Therefore, we manufactured customized deformable particles using PEGDA hydrogel microbeads as a gametocyte model at various PEGDA concentrations (7.5%, 10%, 12.5%, 15%, 17.5% (w/w)). These hydrogel beads were synthesized in-house using droplet microfluidics to ensure uniform size distributions (see Figure 5-7 and Figure 5-8). Prior to the experiment, synthesized PEGDA beads were filtered using a 15 μm mesh cell strainer for monodispersed samples in size. The bead size uniformity was also confirmed with optical imaging analysis (Figure 5-8). Our synthesized PEGDA beads were found to be very stable after months of storage.

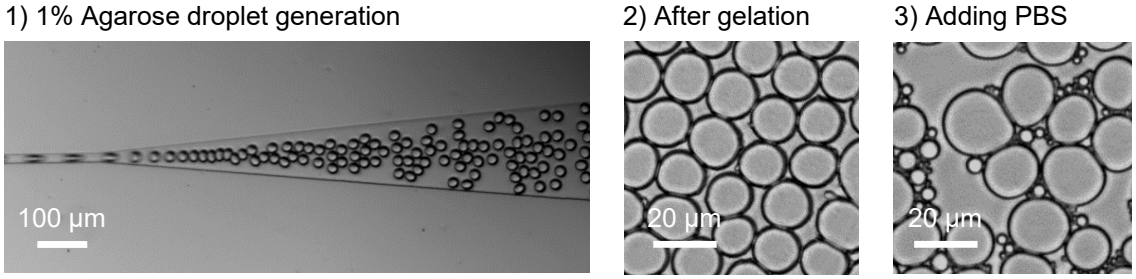

Figure 5-9: Agarose bead synthesis using a microfluidic droplet generator. (1) Generation of agarose beads in mineral oil, (2) Agarose beads after gelation, (3) Agarose beads after washing, and dispensed into PBS solution. We found the agarose beads start to coalesce with each other after washing and dispensed into PBS solution. After about 1 hour, these agarose beads were fully dissolved into the PBS at room temperature. This behavior is likely due to our agarose beads were not strongly cross-linked.

Figure 5-10 shows the results for the transit-time-based characterization of the model particles with different PEGDA concentrations. Figure 5-10A illustrates the representative current traces. Single-particle events were clearly observable. The transit time and current dip from each particle can be extracted. The right panels in Figure 5-10A show representative events at different PEGDA concentrations. Similar ionic current dips were observed for different PEGDA concentrations, expected from the uniform particle size (Figure 5-7 and Figure 5-8). On the other hand, the transit time becomes longer when increasing the PEGDA concentration (as can be clearly seen from the representative cases in Figure 5-10A). Figure 5-10B shows the transit time distribution for the model particles with different PEGDA concentrations. A clear right-shift of the transition time was visible when increasing the PEGDA concentration. To quantify the relationship, Figure 5-10C plots the transit time as a function of the PEGDA concentration. A linear relationship was observed, similar to observations made in previous studies using agarose gel beads [149]. This well-established relationship between the transit time and the PEGDA concentration confirms that the transit time could be used as an effective deformability marker. It is interesting to note that the transit time variance increases when increasing the PEGDA concentration (Figure 5-10C). This observation is in good agreement with previous results on direct mechanical characterization [152]. We believe that the PEGDA-based deformability model particles would find various applications in future cell-mechanotyping-related research [129].

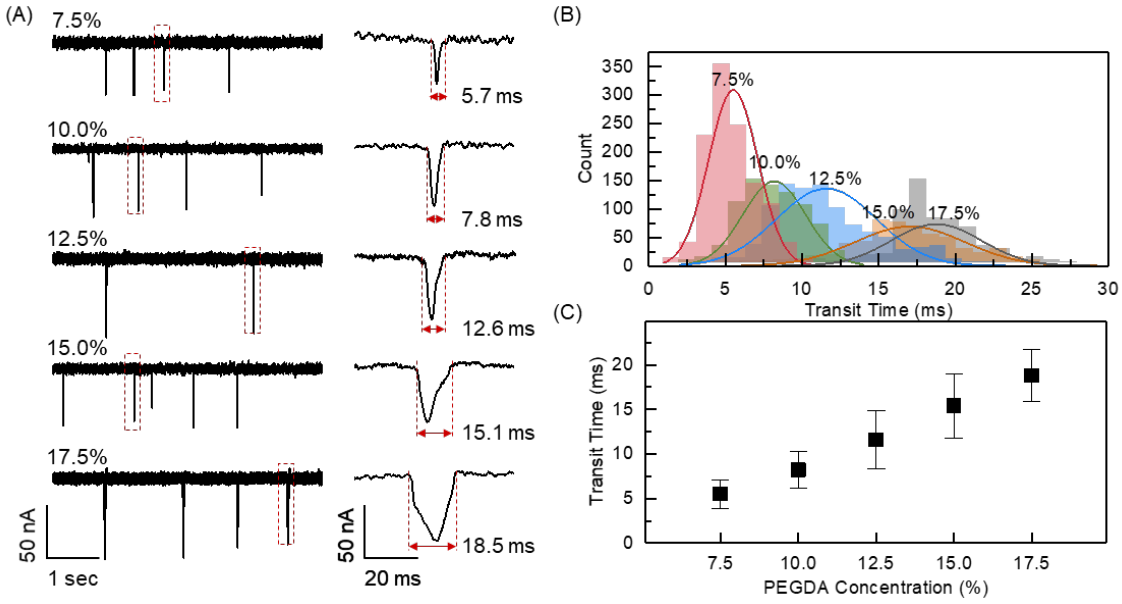

Figure 5-10: Characterization of the deformable PEGDA hydrogel beads. (A) Ionic current time traces (left), and the enlarged view of a single representative particle with the transit time denoted (right). (B) Distribution of the transit time of model deformability particles at different PEGDA concentrations (N= 1243 (7.5%), 1243 (10%), 604 (12.5%), 765 (15%), and 928 (17.5%)). The bin size is 1.1 ms. (C) Correlation between transit time and PEGDA concentration.

5.8. Deformability-activated sorting: throughput, purity, and efficiency

To evaluate our single-particle-resolved deformability-activated sorting, we used 7.5% and 14% PEGDA hydrogel microbeads to represent two populations of particles of different deformability. Both model particles have a mean diameter of 14 μm. To distinguish these two populations under the microscope, 1 mM calcein dye was added to the 14% PEGDA hydrogel microbeads (rigid particles, red dashed circles in Figure 5-11). Each model particle was independently adjusted to a concentration of 2×10^6/ml by adding PBS with 0.05% Tween-20. To prepare a mixed sample containing both populations, equal volumes from each model particle-containing solution were mixed thoroughly before loading to the microfluidic chip. The sensing window (T_{sens}) was set to 60

ms since the particles had a transit time range of 5-25 ms (Figure 5-11B). To enhance the sorting purity, the sorting algorithm was programmed to sort only particles with well-defined transit time signals. Once the transit time (*i.e.*, cell deformability) was measured, a corresponding solenoid valve was trigged with a pulse duration of 40 ms (T_{valve}) to actuate the sorting. The transit time threshold was set to 10 ms to distinguish between the soft and rigid populations.

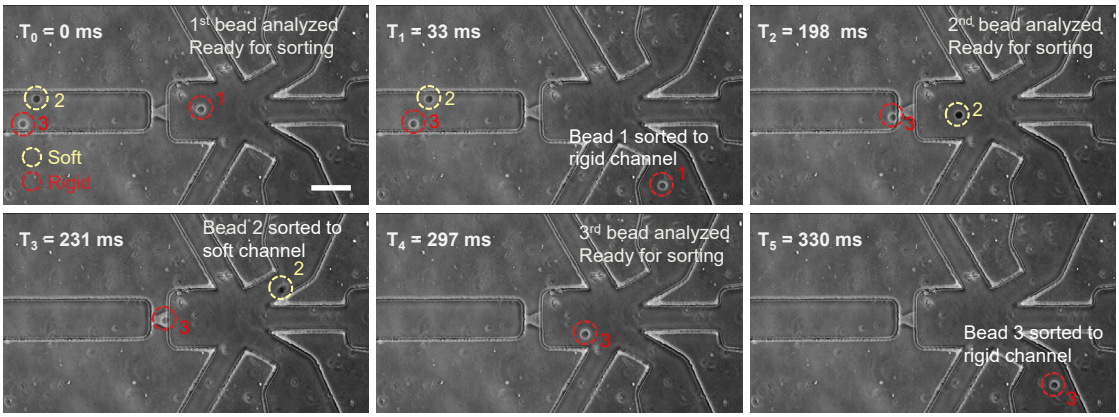

Figure 5-11: Device validation with deformability PEGDA hydrogel beads. The rigid particles (with the dye added, bright edge) and soft particles (dark) are marked with red and yellow circles, respectively. The pulse duration of the sorting signal was 40 ms in this experiment (scale bar: 100 μm).

Due to the fluorescent dye in the 14% PEGDA hydrogel beads, we were able to trace the particles by imaging to determine if the soft and rigid particles were correctly sorted. Figure 5-11 shows the representative images of three particles sequentially passing through the deformability sensing pore and then being sorted. As shown, it takes approximately 300 ms to correctly sort these three particles, leading to a throughput of approximately 600 particles/min.

Table 5-2 summarizes the sorting results. It was found that ~88% sorting purities were achieved for both soft and rigid particles. The incorrect sorting was mainly due to the insufficient time gap (T_s) between consecutive particles. Our system has a relaxation time of approximately 20 ms. It

takes approximately 40 ms for the sorting pressure to fully stabilize between high and low levels. Therefore, the minimal particle spacing time (T_{smin} annotated in Figure 5-4B) is 40 ms. Any two particles too close to each other could be sorted incorrectly. This observation matches the simulation results, which indicated that minimal T_s is required for successful sorting under the worst-case scenario.

Table 5-2 also shows the sorting efficiency for soft and rigid particles at 81.35% and 65.83%, respectively. The average sorting efficiency for both types is 73%. The sorting efficiency was mostly affected by the variations of the particle travel time between the buffering region and the sorting region (Figure 5-1A) due to the parabolic laminar flow velocity profiles. If the time it takes for a particle to travel from the buffering region to the sorting region is mismatched with the sorting pulse 'off' time, the corresponding particle will be directed to the waste channel. A straightforward solution to this issue is to decrease the channel width of the buffering region (and extend the length to produce a contact travel time). Another factor that affects the sorting efficiency is the accuracy of the transit time measurement since this is the basis for the trigging signal. When the transit time measurement is uncertain (*e.g.,* multiple or partial peaks within the sampling window), our algorithm ignores this particular particle, and no sorting action is taken. This contributes to some of the particles being directed into the waste channel, which reduces the sorting efficiency.

Table 5-3: Sorting performance metrics using model soft and rigid beads.

Outlet	Target	# of soft beads	# of rigid beads	Purity (%) [a]	Efficiency (%) [b]
Outlet 1	Soft	205	28	87.98	81.35
Waste	-	24	67	-	-
Outlet 2	Rigid	23	183	88.83	65.83

[a] Purity defined as the particle fraction appearing at each collection outlet where the particles were intended to be.

[b] Efficiency defined as the ratio of target particles at the desired outlets to those at the inlet.

5.9. Summary

In summary, we demonstrated a first-of-its-kind, single-particle-resolved, cytometry-like deformability-activated sorting in continuous flow on a microfluidic chip. Compared to the bulk-based deformability separation methods and traditional micropipette aspiration single-particle deformability measurement, the demonstrated device stands out in terms of the tradeoff between the throughput and the single-particle resolution. Both modeling and experimental results reveal that there is a lower limit of the particle spacing (and thus an upper limit of the throughput) for correct deformability-activated sorting. With the well-characterized PEGDA hydrogel beads, we demonstrated an operation throughput of ~600 particles/min, which can be further improved by reducing the system relaxation time. In addition, multiplexed channels could also be implemented in the future to further enhance sorting throughput. We demonstrated a sorting purity of ~88% and an efficiency of ~73%, which can be improved by introducing better particle spacing. For future validation with polydisperse biological cells, an on-chip size filtration should be incorporated to ensure that the cell size is suitable for squeeze-based deformability sensing.

Chapter 6 Time-division Multiplexing Accessing (TDMA) Microfluidic Device For High-throughput Resistive Pulse Sensing

We demonstrated “first-of-its-kind” deformability-activated cell sorting (DACS) for gametocyte enrichment in Chapter 5. While evaluating the sorting performance, we found that deformability-based sensing is a rate-limiting step for deformability-activated cell sorting. To address this limitation, multiple pore-based cell deformability sensing integrated with DACS can be considered. However, the scalability of deformability sensing array is often limited by the cost because each fluidic channel would require an independent measuring unit. An ideal multiplexed deformability sensor should have a single output to interface with the single-input instrument easily.

In Chapter 6, we present a microfluidic time-division multiplexing accessing (TDMA) resistive pulse sensing, in which the deformability of malaria-infected RBCs can be analyzed through a scalable number of microfluidic channels. With an eight-channel microfluidic device and polystyrene particles as a gametocyte model, we successfully demonstrated the single-end multiplexed resistive pulse sensing with excellent scalability. Besides, the availability of multiple sensing pores provides a robust mechanism to overcome the clogging issue, allowing the analysis to continue even when some of the pores are clogged. We envision this microfluidic TDMA approach could facilitate the future development of multiplexed deformability sensor and high-throughput DACS.

6.1. Introduction to microfluidic TDMA deformability sensing

High-throughput cell deformability sensing and deformability-activated sorting is essential for analysis of rare gametocyte in the bloodstream. In this regard, multichannel deformability sensing system have a clear advantage in terms of faster data collection and analysis throughput. The integration of multiple channels into the same device also enables the analysis of the same sample with different experimental parameters such as pore size. Besides, multiple pores also help to keep the analysis running even one or few of the pores are clogged, a grand challenge in pore-based resistive pulse sensors[153, 154]. In recognition of these benefits, efforts to simultaneously record multiple channels will address the rate-limiting factor of deformability-activated cell sorting (*i.e.*, deformability sensing, see section 5.8) and enable high-throughput and reliable sorting for gametocyte enrichment. However, the scalability of the channel numbers is limited by the cost because each fluidic channel would require an independent measuring unit. An ideal multiplexed resistive pulse sensor should have a single output to interface with the single-input instrument easily. To this end, one method employs the frequency division multiplexing for multichannel, single-output resistive pulse sensing. Signals from multiple channels are modulated by an AC signal with a single frequency and then recovered by digital bandpass filtering[155]. Another method emulates the radio communication technique of code-division multiple access (CDMA) to achieve an all-electronic, single-output interface[156]. As particles traverse encoding electrodes, orthogonal digital codes are generated. Software algorithms were used to decode the output signal to correlate each resistive pulse with its channel of origin.

Herein, we reported a microfluidic time-division multiplexing accessing (TDMA) single-end resistive pulse sensor, which can be used for multiplexed gametocyte deformability sensing. In the cellular communication field, TDMA allows multiple users to communicate with a base station over a common channel through time-sharing[157]. The microfluidic TDMA resistive pulse sensor

adopts a similar principle to multiplex the signal from many different fluidic channels. With a single-ended data acquisition, signals from each channel can be reconstructed for particle analysis in the corresponding channels. We successfully demonstrated a low-cost eight-channel resistive pulse sensor for detecting polystyrene particles as a model gametocyte. Further scaling up the multiplexity is straightforward and within reach. We also found that the multiplexed TDMA device is able to continue the analysis even when a few channels are clogged, solving one of the most significant challenges in pore-based resistive pulse sensor. We anticipate this single-ended time-shared approach would facilitate the future development of multiplexed deformability sensor and high-throughput deformability-activated cell sorting.

6.2. TDMA working principle

Figure 6-1a shows the block diagram of the microfluidic TDMA system designed to interface the *N*-channel microfluidic resistive pulse sensor. The integrated TDMA system consists of the trans-impedance amplifiers, an analog multiplexer, analog-to-digital converter (A/D), and demultiplexer. The multiplexer sequentially reads the amplified analog signals from each sensing channel with a switching frequency of f_s. In other words, each channel is sampled every N/f_s second (*i.e.,* the period of a single TDMA frame, the top panel in Figure 6-1b) and digitalized by an A/D for data acquisition. A demultiplexing algorithm reconstructs the signal for each channel using the scheme shown in Figure 6-1b. It is noteworthy that there is a tradeoff between the channel multiplexity N and the effective channel sampling frequency using a fixed switching frequency.

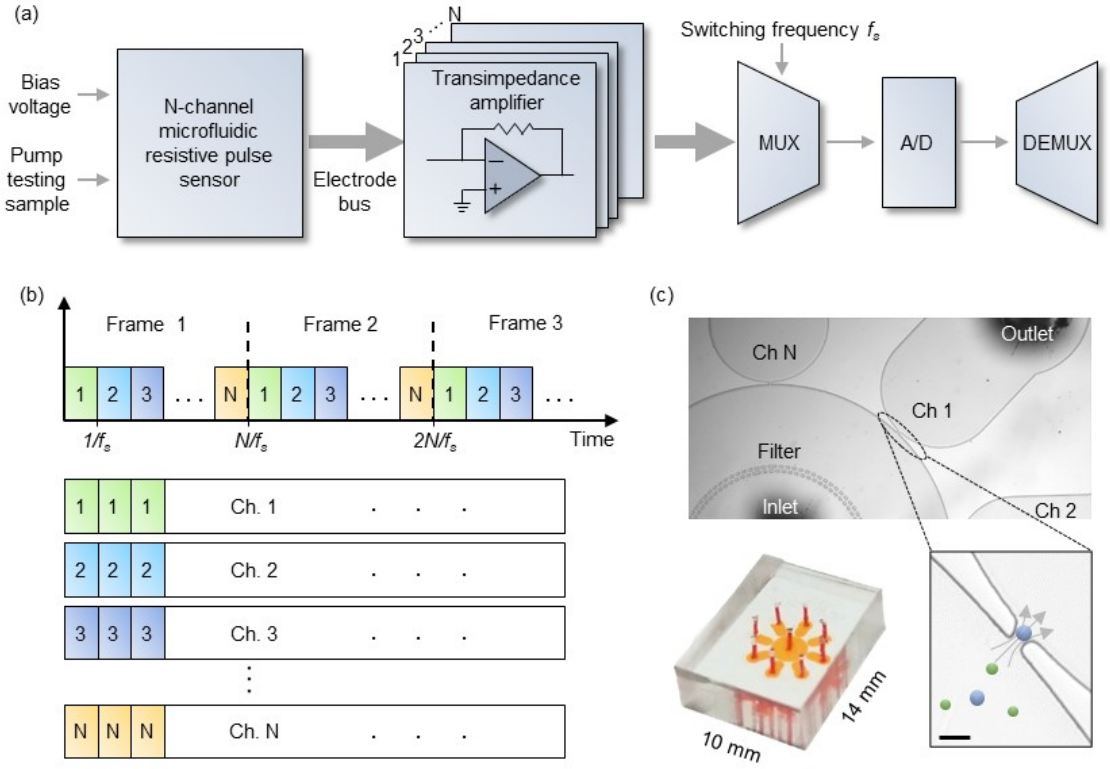

Figure 6-1: TDMA resistive pulse sensor working principles. (a) Time-division multiple access block diagrams. (b) Illustration of the demultiplexing algorithm. The serial signal from the multiplexer output was reconstructed for each channel. (c) Microscope images of the 8-plexed device. The enlarged image illustrates the particle translocation through the sensing pore. A micro-filter is placed upstream to reduce the potential debris.

6.3. Scalability of TDMA

In our proof-of-principle study, we implemented an eight-channel microfluidic device with a circular layout (Figure 6-1c**).** All eight channels have separated outlets, yet share a common inlet (Figure 6-1c). A micro-filter structure is designed near the common inlet to remove the potential debris. In a typical experiment, the polystyrene particle translocation time was in the range of 8±2.7 ms (Figure 6-2). To resolve the single particle translocation event, each channel should have a minimum sampling frequency higher than the Nyquist frequency (250 Hz). We used a switching

frequency f_s of 200 kHz for the eight-channel implementation. The equivalent single-channel sampling frequency is 25 kHz, sufficient for resolving the single particle translocation. In fact, the channel multiplexity can be scaled up to 800 if we work at the minimal Nyquist frequency. Note that this TDMA principle could also be extended to microfluidic deformability sensors, in which single-molecule translocation is usually much faster. For a typical dwell time as short as ~100 µs (Figure 4-2 in Chapter 4), the same 200 kHz switching frequency is sufficient to resolve ten channels.

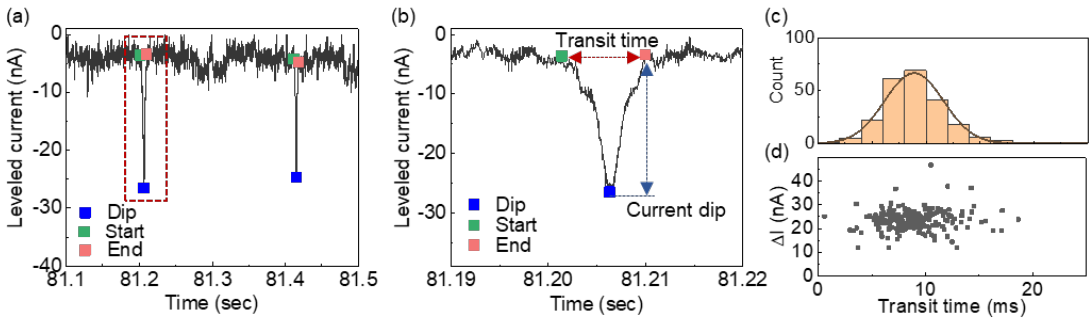

Figure 6-2: Time trace for the 10 µm beads. (a) Representative ionic current dips (b) Enlarged the view of the current dip (red box from Figure 6-2a). The pulse has a transit time of ~8 ms and a current dip of 22 nA. (c) Histogram of transit time for 10 µm beads. The distribution shows a mean transit time of 8 ± 2.7 ms (N = 227).

6.4. TDMA integration

6.4.1. Microfluidic device fabrication

An eight-channel microfluidic device was designed using CAD software (Figure 6-3). The photomask was printed on transparent film (CAD/Art Services, Inc.). The casting mold was fabricated on a 4-inch silicon wafer using SU-8 2025 (MicroChem) through a standard lithography

process. The mold height of ~35 µm was confirmed with a profilometer. The width and length of the micropore were optimized to ~18 µm and ~20 µm respectively. The microfluidic device was fabricated using polydimethylsiloxane (PDMS) (Dow Corning). A 10:1 w/w mixture of base and curing agent was cast onto the SU-8 wafer mold, degassed, and cured at 80°C for an hour. After demolding the patterned PDMS, inlet and outlets were punched using a stainless needle (ϕ = 0.75 mm). The resulting PDMS stamps and glass slides (100 µm thickness, ted-Pella) were treated with oxygen plasma and in contact to form irreversibly covalent bonding between two materials.

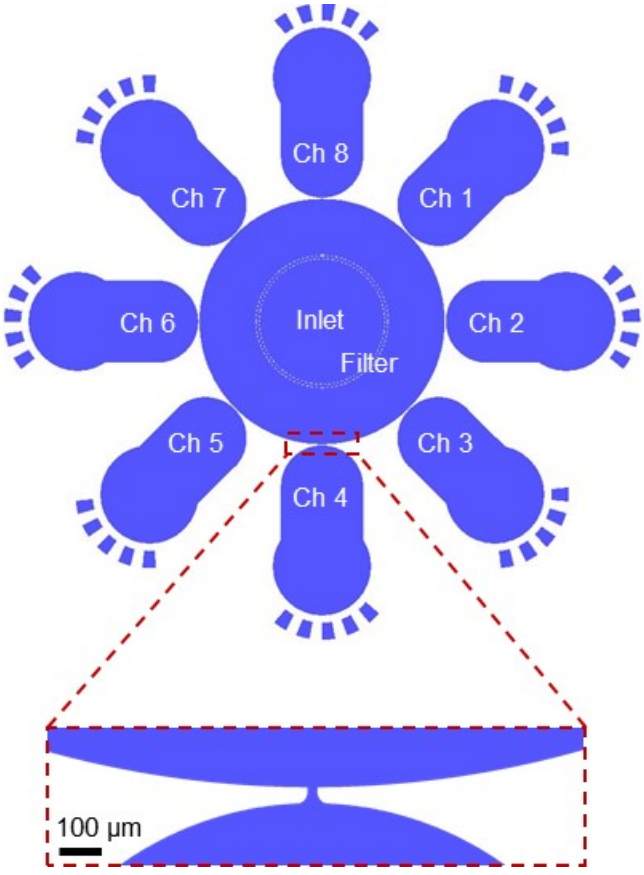

Figure 6-3: 8-channel microfluidic device layout. The enlarged view showed the resistive pulse sensing unit, which has micropore with width, length, and height of 18 µm, 20 µm, and 35 µm, respectively. The customized tygon tubes with Ag/AgCl electrodes embedded were inserted into

common inlet and outlets on the microfluidic devices. The outlets were grounded, while the inlet was biased at a constant voltage (400 mV).

6.4.2. TDMA hardware

The TDMA hardware circuit was implemented on a custom printed circuit board (PCB) (OSH Park), which includes trans-impedance amplifiers (TL072, Texas Instruments), analog multiplexer (ADG406, Analog Devices), and counter (dual negative-edge-triggered JK flip-flop: 74LS73, Texas Instruments; 2-input AND gate: DM7408, Fairchild Semiconductor™) (Figure 6-4). Eight sensing units from the microfluidic device were connected to trans-impedance amplifiers. A feedback resistor (R= 1 MΩ with 5% tolerance) was used to set the gain. The amplifier outputs were connected as inputs to the multiplexer. The multiplexer channels were periodically selected by a $\log_2(N)$ bit synchronous counter. The sampling frequency for each TDMA frame was synchronized to the multiplexer switching frequency. The analog voltage output from multiplexer was sampled at 200 kHz with 16-bit DAQ card (NI PCIe-6351, National Instruments) and stored through a data acquisition software (LabVIEW, National Instruments). The recorded data were demultiplexed using MATLAB (MathWorks) program. All electronic components and microfluidic device were placed in customized Faraday cage to shield the environment noise.

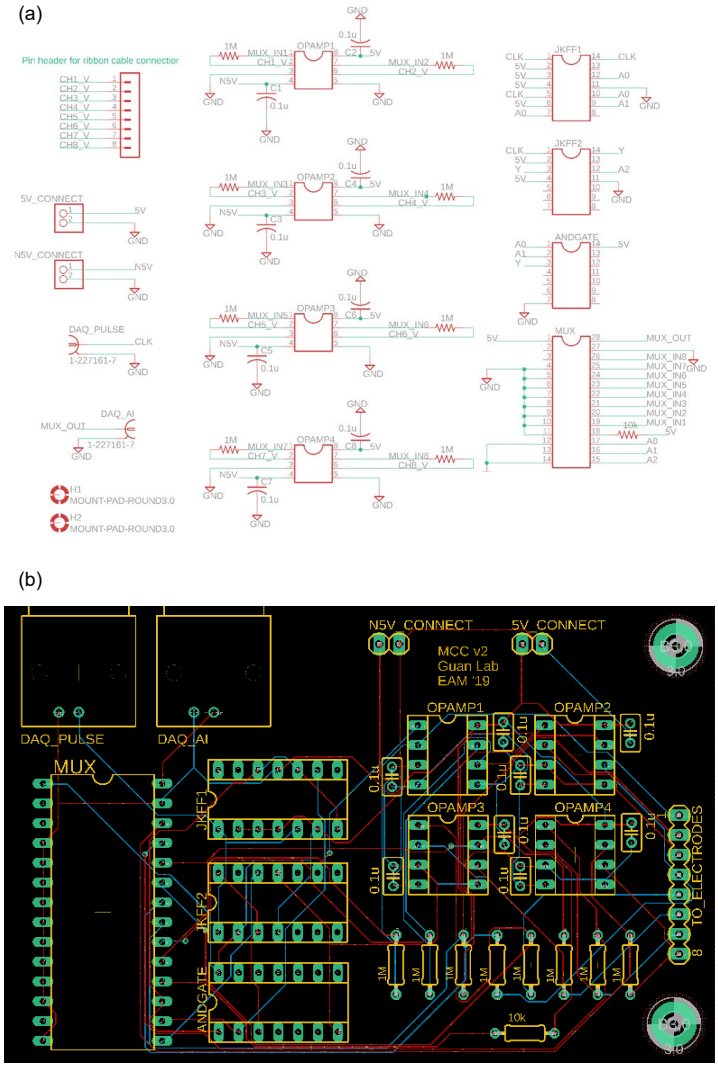

Figure 6-4: TDMA hardware design. (a) Electronic schematic diagram. The system includes trans-impedance amplifier circuits, multiplexers, and counter circuits. DAQ provides the bias voltage for ionic current measurement and a clock signal for the 3-bit counter. External DC power source was used to provide the supply voltage for op-amps, multiplexer, JK flip-flop, and AND gate. (b) PCB layout. The PCB has dimensions of 95×62 mm and is shielded by the Faraday cage to reduce the environmental noise.

6.5. Validation of the microfluidic TDMA principle

6.5.1. Validation of 8-channel resistive pulse sensing

To validate the 8-channel microfluidic resistive pulse sensor and the TDMA scheme, we tested polystyrene particles (coefficient variance <10%, Polyscience) of 10 μm diameter at a concentration of ~2.4×10^5 particles/ml. The polystyrene particles were mixed with 1x PBS buffer (1X, pH 7.4) with 0.05% Tween-20 (TEKnova) to avoid particle aggregation. Prior to sample loading, the microfluidic channels were prefilled with electrolyte (1x PBS with 0.05% Tween-20) for electrical measurement. The prepared sample was introduced into the inlet of the microfluidic device with a flow rate of 200 μl/hr using a syringe pump (Harvard Apparatus PHD 2000). The signal from each of the eight channels was sequentially switched at 200 kHz into one single output by the TDMA hardware. The digitalized combined signal was then demultiplexed to reconstruct the time trace signal for each channel. Figure 6-5a shows the demultiplexed current time traces for all eight channels. Apparent ionic current dips, corresponding to individual particle translocation events, could be easily observed from all channels. These current dips were uniform in magnitude due to the introduced monodisperse particles.

One of the concerns in TDMA resistive pulse sensing is the interference due to the signal leakage in analog switching networks. The current dips in Figure 6-5a appear in random sequence, implying that each channel can independently analyze the particles without crosstalk among channels. To quantify the channel-to-channel crosstalk, we performed the cross-correlation analysis of ionic current profiles among eight sensing channels and extracted the Pearson correlation coefficient. Figure 6-5b shows the heatmap of the correlation between channels. The inter-channel correlation is quite small (with coefficient ranging from -0.25 to 0.32), confirming the signal integrity in each channel. Interestingly, the correlation seems alternating between the positive and negative value

for channels separated by odd and even numbers, which is likely due to the characteristics of the switching networks.

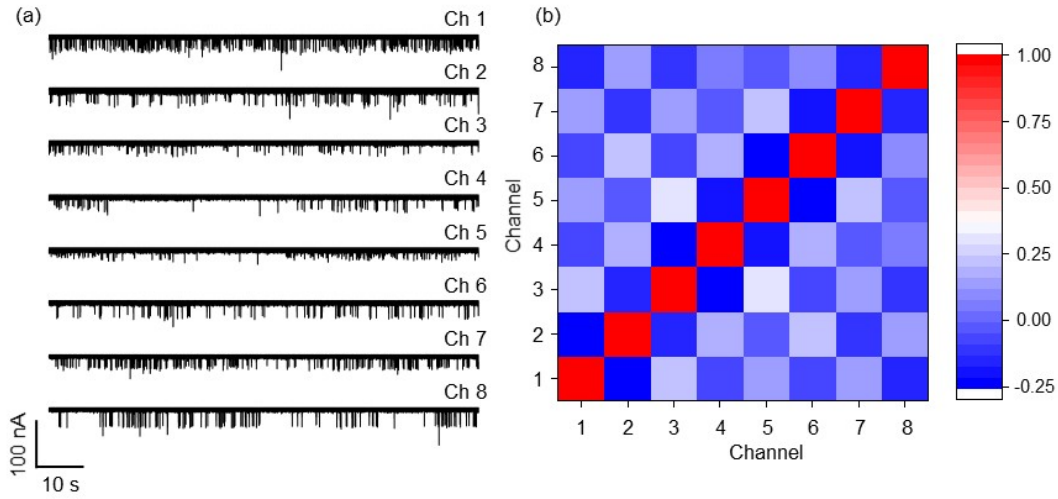

Figure 6-5: Validation of TDMA resistive pulse sensor. (a) Reconstructed current time trace for each of the eight channels. (b) Cross-correlation among different sensing channels.

6.5.2. Analyzing particle size and concentration

To further validate the multiplexed sensing, we analyzed the particle size and concentration from obtained resistive pulses during particle translocation events. As a particle sizing model, Gregg and Steidley's expression was suitable for the case when sphere diameter is approaching to the orifice diameter. The expression was derived from the following relation,

$$R = \rho \int \frac{dz}{A(z)} \qquad (1)$$

where R is the resistance of the tube, and A(z) is the cross-sectional area of the tube where the area does not contain the sphere. The tube is centered on the z-axis; thus, particles flow toward the z-

direction. The current density across the orifice cross-section is assumed to be uniform. To incorporate the varying *A(z)*, $A(z) = \pi {D_o}^2/4$ for empty orifice and $A(z) = \frac{\pi}{4}\left({D_o}^2 - {d_s}^2 + 4z^2\right)$ for the sphere containing orifice were substituted into the (*Do*: diameter of orifice, d_s: diameter of the sphere). Since the model was derived from Eq. (1), a uniform current density is desired across the cross-section of the orifice for optimal estimation (*e.g.*, particle size comparable to the orifice diameter). Based on this rationale, we chose Gregg and Steidleye's model since our polystyrene bead diameter is similar to the sensing pore diameter.

The relative resistance changes (*ΔR/R*) caused by particle translocation at a sensing pore is described by the following particle sizing equation [158],

$$\frac{\Delta R}{R} = \frac{D}{L}\left[\frac{\arcsin(d/D)}{\sqrt{1-(d/D)^2}} - \frac{d}{D}\right] \qquad (2)$$

where *d* is particle diameter, *D* and *L* are cylindrical orifice diameter and length, respectively. For the rectangular micropore, we substitute $D = (4\times W\times H/\pi)^{1/2}$, where *W* and *H* are a sensing pore width and a height, respectively. *ΔR/R* was extracted from the data using MATLAB (MathWorks), and particle diameters were obtained by Eq. (2). Note this particle sizing model does not take into consideration the correction factor [158] and thus can lead to uncertainty in size determination.

To calculate the particle concentration, total particle counts from the eight sensing units were divided by the total introduced sample volume. The total particle counts were extracted by counting the resistive pulses using the peak-detection algorithm in MATLAB (Figure 6-6). The total introduced sample volume was obtained from the multiplying volume flow rate by the elapsed time.

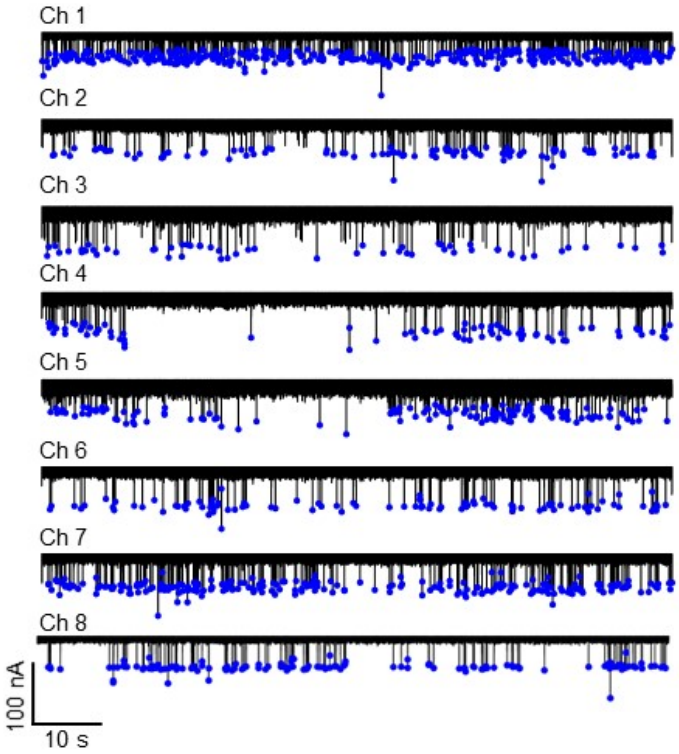

Figure 6-6: Validation of custom-built peak detection algorithm. The algorithm continuously finds the local minimum value and signal baseline. The current dip was calculated by subtracting the local minimum value from the signal baseline. Minimum peak values for individual resistive pulses were marked by blue circles.

To test the multiplexed TDMA resistive pulse sensor for particle sizing, we extracted the relative resistance changes ($\Delta R/R$) from the detected resistive peaks in Figure 6-5a. To determine the particle size, we applied the particle sizing model using Eq. (2). Figure 6-7a shows the particle diameter distribution in each channel, together with a combined distribution from all channels. The combined distribution follows a Gaussian distribution with a mean value of ~9.5±0.54 μm. The calculated particle diameter is comparable, yet smaller than the actual particle size (10 μm). The under-estimation of the particle diameter may come from the fact that the particle sizing model assumes particles pass through the centerline of the pore [159]. Motion displacement from the center axis could cause the underestimation. It was also observed that the mean particle diameter

varies among eight individual channels (Figure 6-7a). This is likely due to the channel-to-channel size variation during the device fabrication and during the experiments (*e.g.*, adsorption of small debris near the pore region). Strategies to improve each of these issues could help to narrow the size distribution.

Since each current dip event represents a single particle and the particle arriving events follow the Poisson process (Figure 6-8), the particle concentration at 95% confidence interval was calculated as $(n \pm 1.96(n)^{1/2})/(vT)$, where n is the total number of particles counted from all 8 channels, T is the total elapsed time, and v is the volume flow rate. The relative uncertainty of inferring the concentration is proportional to $n^{-1/2}$. Figure 6-7b shows the calculated concentration as a function of total counted particles. After counting about 1000 particles, the calculated concentration converges to that of the input sample (2.4×10^5 particles/ml) with little uncertainty. The standard deviation is mainly because particle arriving dynamics to the individual microconstrictions follows the non-homogenous Poisson process (see Section 6.6 for details). To minimize the deviation, symmetric flow streamlines from an inlet to multiple outlets through all constictions are required.

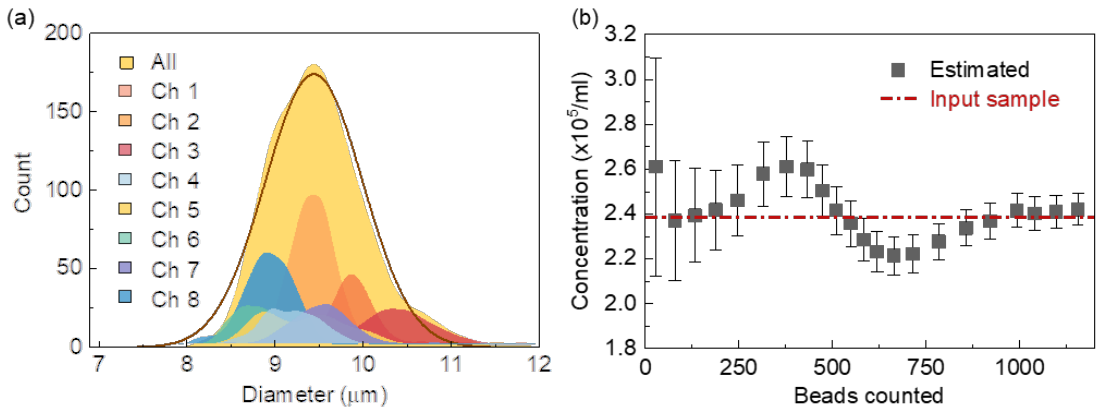

Figure 6-7: Particle size and concentration measurement. (a) Histograms of the calculated particle diameters from each individual sensing channel (N_{Ch1}:131, N_{Ch2}: 309, N_{Ch3}:104, N_{Ch4}: 97, N_{Ch5}:124, N_{Ch6}: 94, N_{Ch7}:102, N_{Ch8}: 223). Distribution of the entire particle diameter data set was plotted with

Gaussian-fit (N_{All}: 1184). (b) Calculated concentration as a function of the counted particles. The error bars correspond to the Poisson noise. The actual polystyrene particle concentration (~2.4×10^5 particles/ml) is indicated by the red dashed line.

6.6. Probing the particle arriving dynamics

A quick eyeball on the current time traces in Figure 6-5a reveals that the particle translocation frequency varies among different channels. To probe the particle arriving dynamics, we examined the event inter-arrival time distribution for each channel. As shown in Figure 6-8a**,** the inter-arrival time distribution shows a remarkable exponential distribution for each channel, indicating a Poisson process [160]. Each channel was fitted with an exponential distribution, $P(t) = \lambda e^{-\lambda t}$, where λ is the expected particle translocation rate. As shown in Figure 6-8a**,** the particle arriving rates among different channels ranges from 0.79 s^{-1} to 3.12 s^{-1}, implying the introduced particles prefer certain channels. This is likely because the effective dimension for each sensing pore is not perfectly identical due to variations in the fabrication and the potential adsorption during the experiment. This creates asymmetric streamlines that lead the particles into preferred channels.

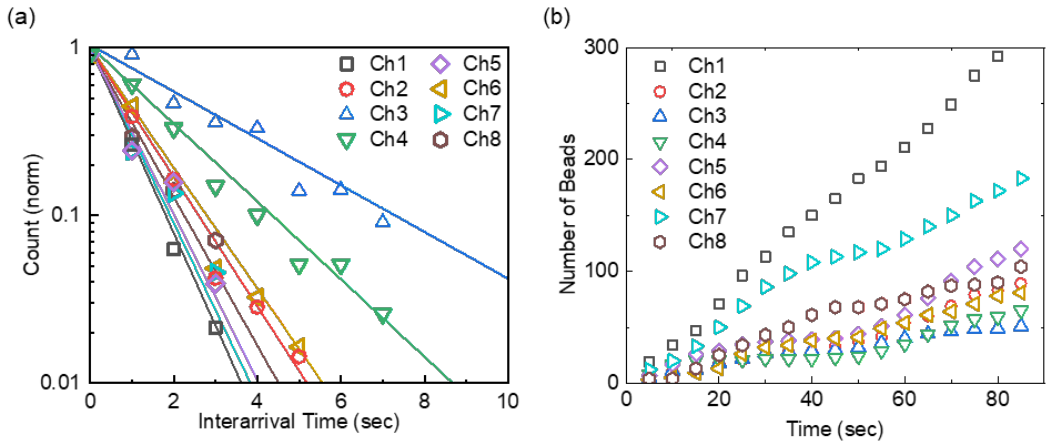

Figure 6-8: Particle translocation dynamics. (a) The normalized distribution of bead interarrival time in different channels, with exponential fits to the distributions (λ_{ch1}: 3.12 s^{-1}, λ_{ch2}: 0.98 s^{-1}, λ_{ch3}: 0.79 s^{-1}, λ_{ch4}: 0.83 s^{-1}, λ_{ch5} 1.21 s^{-1}, λ_{ch6}: 0.88 s^{-1}, λ_{ch7}: 1.88 s^{-1}, and λ_{ch8}: 1.13 s^{-1}). (b) Cumulative counted particle numbers versus the elapsed time.

To further examine whether the observed Poisson process is homogenous or nonhomogeneous, we plotted the accumulative particle number versus the elapsed time. As shown in Figure 6-8b**,** the slope of the curve (*i.e.,* the translocation rate) is different among channels, consistent with what we observed from Figure 6-8a**.** However, the slope of the curve for each channel shows a clear time-dependence. This indicates the translocation rate for sub-processes indeed varies. Therefore, the particle translocation process of our experiment is a nonhomogeneous Poisson process.

6.7. Analyzing a mixed population

To test the microfluidic multiplexed TDMA resistive pulse sensor for analyzing a mixed population, we prepared a mixed sample containing 10 μm and 15 μm polystyrene particles (coefficient variance <10%, Polyscience) with concentrations of ~2.4×10^5 ml^{-1} and ~0.8×10^5 ml^{-1}, respectively. Figure 6-9a shows the demultiplexed current time traces for all eight channels, and Figure 6-9b shows an enlarged section from channel 4 (red boxed area). As expected, we observed two distinct levels of current dips corresponding to the two size populations. Other channels also show similar two population characteristics. Using the particle sizing model Eq. (2) and combing events from all channels, the particle sizes were calculated, and their distribution is shown in Figure 6-9c**.** The particle size distribution shows evident two populations with a mean value of 9.31 ± 0.40 μm (10 μm particle population) and 12.46 ± 0.48 μm (15 μm particle population), respectively. The underestimation for each population is likely due to the same reason, as we saw in Figure 6-7a**.** The particle numbers counted for each population is 1233 and 355, the ratio of which (~3.47) is close

to that of the input concentration value (~3), confirming the discriminative ability between these two populations.

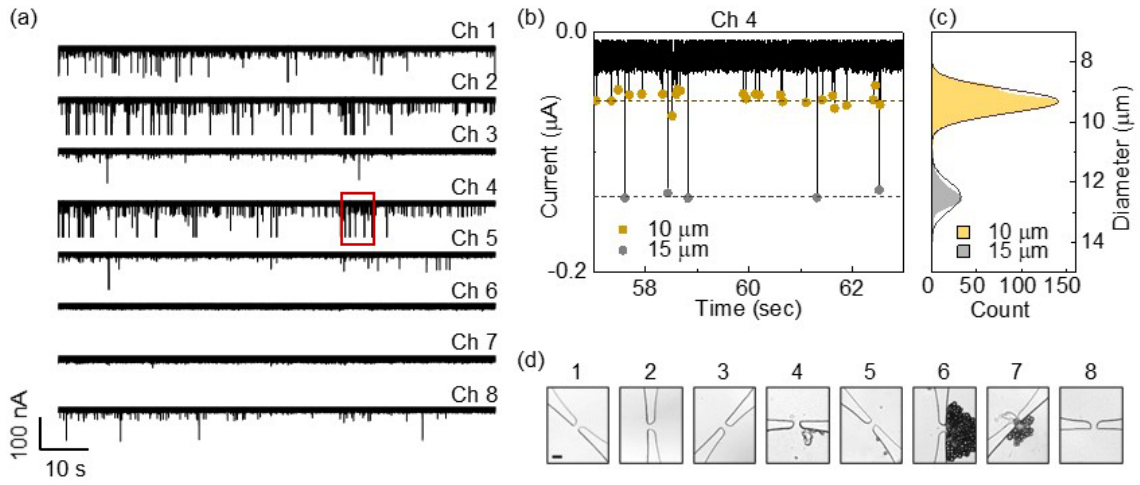

Figure 6-9: Discriminating particles of different sizes. (a) Reconstructed current time trace for each of the eight channels. (b) Enlarged view of ionic current in channel 4 (red) showing representative pulses from a mixture of 10 μm and 15 μm diameter particles. (c) Distribution of the particle size, with Gaussian-fit. A clear two population was observed. ($N_{10\mu m}$: 1233 and $N_{15\mu m}$: 355). (d) Microscope images showing the pore-clogging in channels 6 and 7 (Scale bar: 20 μm).

6.8. Robustness against pore-clogging

While we did not see any clogging issue when testing the 10 μm sized particles (Figure 6-5a), a clear feature observed in Figure 6-9a when testing the 15 μm sized particles is that two out of eight channels (channel 6 and 7) show no particle translocation events. We examined the sensing pores using a microscope after the experiment. It was found that channel 6 and 7 were indeed clogged by particle jamming at the pore (Figure 6-9d). This is not surprising since the pore cross-section is of dimension 18 μm×20 μm×35 μm (W×L×H). When 15 μm sized particles were introduced, the chance for clogging becomes much higher. Such irreversible clogging is a well-known issue for

single-channel resistive pulse sensors that limits its flexibility in real-world applications[153, 154]. In contrast, the TDMA multichannel resistive pulse sensor allows the analysis to continue even when some of the pores are clogged (Figure 6-9c).

6.9. Summary

By introducing the time-division multiple access technique in the telecommunication field into the microfluidic field, we developed and demonstrated the multiplexed microfluidic resistive pulse sensor, which can be adapted for multiplexed gametocyte deformability sensing. The microfluidic TDMA resistive pulse sensing technology allows each channel to transmit its temporal signal in rapid succession to a single electrical outlet, using a defined time slot with a defined order, which can then be used to recover the signal from each channel by a simple demultiplexing algorithm. With the prototyped TDMA instrumentation and the eight-channel microfluidic device, we validated the multiplexed microfluidic TDMA principle. Besides, the availability of multiple sensing pores provides a robust mechanism to fight against the clogging issue, allowing the analysis to continue, which is otherwise not possible in single-channel devices. While the TDMA resistive pulse sensing technology is validated in microfluidic devices in this study, we expect this proof-of-concept could be well extended to future development of high-throughput deformability-activated cell sorting.

Chapter 7 Conclusion and Perspectives

7.1. Conclusions

This dissertation presents novel microfluidic methods to achieve molecular and cellular detection of malaria for elimination. The demand for screening of asymptomatic infections and surveillance of transmission has been steadily increased. Besides, the effort of understanding the underlying mechanism of malaria pathophysiology is greatly helpful for researches in drug development. To this end, advanced translational technologies such as microfluidic lab-on-a-chip are of high importance to bring practical malaria elimination strategy to the field. Despite the extensive technological efforts, following two aspects have not been fully resolved yet:

(1) There is an unmet need for existing diagnostic devices that fulfill Affordable, Sensitive, Specific, User-friendly, Rapid and robust, Equipment-free, and Deliverable to end-users (ASSURED) criteria.
(2) There is a lack of tools to investigate the degree of illness and to understand the underlying mechanism of malaria transmission.

The thesis suggests novel technological solutions to tackle such demands with the following approaches: (1) lab-on-a-disc nucleic acid testing and (2) cell-based detection using microfluidic cell mechanotyping.

In the effort to deliver a highly sensitive diagnostic system in the field, we developed a "sample-to-answer" nucleic acid testing platform. The unprecedently integrated system facilitates streamlined parasite DNA extraction, purification, and real-time detection on a single reagent

compact disc. For the automated sample process, energy-efficient magnetic interaction was implemented to move the nucleic acid bearing magnetic beads to the desired liquid chambers in the reagent disc without fluid motion. We demonstrated that the device could deliver molecular answers from a small volume of the raw blood sample with a detection limit of ~0.5 parasites/μl in 40 minutes. This level of sensitivity is sufficient for identifying asymptomatic parasite carriers in the field.

The technological effort to improve the scalability and throughput of the field-deployable nucleic acid testing is accomplished by the development of a multiplexed nucleic acid testing platform. The system performs the entire DNA sample preparation for four samples and subsequent LAMP-based nucleic acid tests in parallel with minimal user intervention. We demonstrated the system's ability to identify two malaria species (*P. falciparum* and *P. vivax*), which are the majority of fatal infections in malaria elimination-phase countries. This technological advancement enables high-throughput, sensitive, and species-specific malaria detection for mass screening and surveillance of transmission as well as epidemiological studies to understand species prevalence and co-infection patterns.

As an effort to investigate the life cycle and malaria pathophysiology, novel microfluidic cell mechanotyping was suggested. We explored the label-free mechanical biomarker (*i.e.*, cell deformability) using a cell deformability sensor. It was found that cell deformability is an excellent indicator to determine the red blood cell states in parasite-invasion. Using this mechanical biomarker, we demonstrated the ability of parasitemia quantification and parasite stage differentiation in the asexual cycle. The microfluidic platform offers numerous benefits, such as rapid data collection (~500 cell/sec), label-free, and secure sample handling in a cell-friendly liquid environment. These benefits allow a wide range of engineering applications (*e.g.*, multiplexed cell detection and hydrodynamic cell sorting) that can be used for cell mechanotyping research.

Upon the development of a cell deformability sensor, a further effort was made to collect cells of interest based on their mechanical properties. The seamless integration of transit-time-based deformability sensor and hydrodynamic sorting onto a single microfluidic chip enables the single-cell-resolved real-time deformability-activated sorting in a continuous flow. The active sorting allows the comparison experiment that requires a sorting condition to be varied within the same device. Besides, the individual cell's quantitative deformability information is accessible. We analyzed the factors affecting the sorting dynamics (*i.e.*, sample flow rate, sorting flow pressure, and system relaxation time) with modeling and experimentally evaluated the sorting performance (*i.e.*, throughput, purity, and efficiency). We found that the device throughput is determined by the summation of sensing, buffering, and sorting time. This DACS system has potential usage in detecting and enriching a rare population of mature gametocytes in the bloodstream.

Regarding the constriction-based cell deformability sensor, we realized the need for developing a multichannel system that enables both fast data collection and high throughput analysis. However, the scalability of the channel numbers is limited by the cost because each fluidic channel would require an independent measuring unit. In the effort to rectify this limitation, the time-division multiple access (TDMA) technique in the telecommunication field was combined with the microfluidics resistive pulse sensing. Through time-sharing, TDMA allows multiple sensing units to monitor cell translocation event with a single-ended data acquisition. This scalable technique would serve as a building block for large-scale integration of future multiplexed deformability sensor and high-throughput deformability-activated cell sorting.

In summary, the significant contributions of this thesis are as follows:

(1) We provided an unprecedently integrated sample-to-answer mobile nucleic acid testing device for highly sensitive detection of asymptomatic carriers in the resource-limited area.

(2) We improved throughput and scalability of the mobile nucleic acid testing device that can perform four species-specific nucleic acid tests in parallel on a single test disc.

(3) We experimentally realized that cell deformability is a promising label-free biomarker for rapid parasitemia measurement and parasite stage determination.

(4) We demonstrated a first-of-its-kind, single-cell-resolved, cytometry-like deformability-activated cell sorting in continuous flow on a single microfluidic chip.

(5) We provided a novel microfluidic TDMA resistive pulse sensing technique for scalable and high-throughput cell mechanotyping.

7.2. Future perspectives

Several important aspects should be addressed in the future research.

In response to the lack of highly sensitive field-deployable point-of-care diagnostics, we successfully developed a sample-to-answer nucleic acid testing device. The system offers the benefits of a rapid diagnostic test (RDT) (*i.e.*, fast, low-cost, minimal training, and minimal sample handling) and lab-based nucleic acid testing (NAT) (*i.e.*, high sensitivity and specificity). Therefore, the system is particularly useful for screening potential carriers who may be highly contagious and seek private self-testing at home before visiting public hospitals. The integrated isothermal amplification assay and automation of magnetic bead-based sample handling by programmable magnetic interaction on a microfluidic chip can be easily extended for many other infectious virus such as HIV, Zika, and COVID-19.

Second, we have evaluated the technical performance of the device with a mimicked malaria-infected sample (*e.g.*, malaria cultured red blood cells mixed with whole blood and parasite DNA spiked whole blood sample). However, the measure of diagnostic accuracy has not been carefully studied yet. This often involves the assessment of diagnostic performance (*e.g.*, receiver-operating characteristics, detection threshold, and diagnostic sensitivity and specificity), which is conducted by the comparison of the diagnostic results from the proposed device and a reference standard technique such as PCR using clinical samples. The proof-of-concept ultracompact and self-sustainable nucleic acid testing device is ready to be deployed in the field for evaluating diagnostic performance.

On the microfluidic cell mechanotyping, there exists exciting technological advancements and real-world applications that have not been explored.

First, all constriction-based cell deformability characterization is only valid under the assumption of identical cell size. However, the non-uniformity of the cell size distribution is typical for biological samples, limiting the reliable and comparable deformability measurements. To decouple the size factor from cell deformability measurement, we can consider independent cell size and deformability measurement using two-stage micro-constrictions as two measurement units [161].

Second, physical measures of cell mechanotyping such as cell compressibility, elastic modulus, stiffness, and deformability are new to clinicians and biologists, who are more familiar with FACS-based molecular assays. Combining capabilities for measuring deformability and fluorescence will provide multi-dimensional information, addressing the specificity issues, and accelerate the adoption of deformability sensor [124]. Such a hybrid setup will be useful where correlational studies between molecular properties and mechanics of specific target cells are required, such as drug screening.

Third, it is essential to improve the throughput of the deformability-activated cell sorting system for rapid cell enrichment. It was found that the minimum resolvable cell spacing determines the sorting throughput. Various hydrodynamic spacing and ordering techniques (*e.g.*, single-cell dispensing [162] and inertial microfluidics [163, 164]) can enhance the sorting throughput. Multiplexed deformability-activated cell sorting system using TDMA resistive pulse sensing method can also be considered as scalable approaches.

Fourth, the thesis successfully demonstrated the deformability-activated cell sorting with synthesized hydrogel beads as deformable model cells. It would be a more promising technology if the device can sort the actual biological cells, such as gametocyte. Deformability-based sorting validation using gametocyte would be particularly useful for testing the efficacy of a transmission-blocking drug [132].

Overall, microfluidic lab-on-a-chip diagnostic technology has a bright future. A combination of multidisciplinary knowledge such as electronics, microfluidics, optics, and biochemistry maximize the benefits for ideal biomedical sensing systems in terms of sensitivity, specificity, accessibility, turnaround time, and cost. Microfluidic molecular and cellular detection strategies presented in this dissertation guide advanced translational technologies that are clinically useful for malaria diagnosis and treatment in the elimination-phase setting.

Bibliography

[1] M. Islam, R. Mezencev, B. McFarland, H. Brink, B. Campbell, B. Tasadduq, E. K. Waller, W. Lam, A. Alexeev, and T. Sulchek, "Microfluidic cell sorting by stiffness to examine heterogenic responses of cancer cells to chemotherapy," *Cell Death Dis,* vol. 9, no. 2, p. 239, Feb 14 2018

[2] N. K. Gill, C. Ly, K. D. Nyberg, L. Lee, D. Qi, B. Tofig, M. Reis-Sobreiro, O. Dorigo, J. Rao, R. Wiedemeyer, B. Karlan, K. Lawrenson, M. R. Freeman, R. Damoiseaux, and A. C. Rowat, "A scalable filtration method for high throughput screening based on cell deformability," *Lab Chip,* vol. 19, no. 2, pp. 343-357, Jan 15 2019

[3] Y. N. Cheng, X. Y. Ye, Z. S. Ma, S. Xie, and W. H. Wang, "High-throughput and clogging-free microfluidic filtration platform for on-chip cell separation from undiluted whole blood," *Biomicrofluidics,* vol. 10, no. 1, Jan 2016

[4] M. Islam, H. Brink, S. Blanche, C. DiPrete, T. Bongiorno, N. Stone, A. Liu, A. Philip, G. H. Wang, W. Lam, A. Alexeev, E. K. Waller, and T. Sulchek, "Microfluidic Sorting of Cells by Viability Based on Differences in Cell Stiffness," *Scientific reports,* vol. 7, May 17 2017

[5] G. H. Wang, W. B. Mao, R. Byler, K. Patel, C. Henegar, A. Alexeev, and T. Sulchek, "Stiffness Dependent Separation of Cells in a Microfluidic Device," *Plos One,* vol. 8, no. 10, Oct 16 2013

[6] D. Holmes, G. Whyte, J. Bailey, N. Vergara-Irigaray, A. Ekpenyong, J. Guck, and T. Duke, "Separation of blood cells with differing deformability using deterministic lateral displacement," *Interface Focus,* vol. 4, no. 6, Dec 6 2014

[7] S. C. Hur, N. K. Henderson-MacLennan, E. R. B. McCabe, and D. Di Carlo, "Deformability-based cell classification and enrichment using inertial microfluidics," *Lab Chip,* vol. 11, no. 5, pp. 912-920, 2011

[8] W. Lee, P. Tseng, and D. D. Carlo, *Microtechnology for cell manipulation and sorting*. New York, NY: Springer Berlin Heidelberg, 2017, p. 14.

[9] Y. H. Chang, C. J. Huang, and G. B. Lee, "A tunable microfluidic-based filter modulated by pneumatic pressure for separation of blood cells," *Microfluid Nanofluid,* vol. 12, no. 1-4, pp. 85-94, Jan 2012

[10] S. B. Huang, M. H. Wu, and G. B. Lee, "A tunable micro filter modulated by pneumatic pressure for cell separation," *Sensors and Actuators B-Chemical,* vol. 142, no. 1, pp. 389-399, Oct 12 2009

[11] W. Beattie, X. Qin, L. Wang, and H. S. Ma, "Clog-free cell filtration using resettable cell traps," *Lab Chip,* vol. 14, no. 15, pp. 2657-2665, Aug 7 2014

[12] X. Qin, S. Park, S. P. Duffy, K. Matthews, R. R. Ang, T. Todenhofer, H. Abdi, A. Azad, J. Bazov, K. N. Chi, P. C. Black, and H. S. Ma, "Size and deformability based separation of circulating tumor cells from castrate resistant prostate cancer patients using resettable cell traps," *Lab Chip,* vol. 15, no. 10, pp. 2278-2286, 2015

[13] Q. Guo, S. P. Duffy, K. Matthews, E. Islamzada, and H. S. Ma, "Deformability based Cell Sorting using Microfluidic Ratchets Enabling Phenotypic Separation of Leukocytes Directly from Whole Blood," *Scientific reports,* vol. 7, Jul 26 2017

[14] Q. Guo, S. P. Duffy, K. Matthews, X. Y. Deng, A. T. Santoso, E. Islamzada, and H. S. Ma, "Deformability based sorting of red blood cells improves diagnostic sensitivity for malaria caused by Plasmodium falciparum," *Lab Chip,* vol. 16, no. 4, pp. 645-654, 2016

[15] E. S. Park, C. Jin, Q. Guo, R. R. Ang, S. P. Duffy, K. Matthews, A. Azad, H. Abdi, T. Todenhofer, J. Bazov, K. N. Chi, P. C. Black, and H. S. Ma, "Continuous Flow Deformability-Based Separation of Circulating Tumor Cells Using Microfluidic Ratchets," *Small,* vol. 12, no. 14, pp. 1909-1919, Apr 13 2016

[16] E. Islamzada, K. Matthews, Q. Guo, A. T. Santoso, S. P. Duffy, M. D. Scott, and H. Ma, "Deformability based sorting of stored red blood cells reveals donor-dependent aging curves," *Lab Chip,* vol. 20, no. 2, pp. 226-235, Jan 21 2020

[17] C. Faigle, F. Lautenschlager, G. Whyte, P. Homewood, E. Martin-Badosa, and J. Guck, "A monolithic glass chip for active single-cell sorting based on mechanical phenotyping," *Lab on a Chip,* vol. 15, no. 5, pp. 1267-1275, 2015

[18] A. A. Nawaz, M. Urbanska, M. Herbig, M. Notzel, M. Krater, P. Rosendahl, C. Herold, N. Toepfner, M. Kubankova, R. Goswami, S. Abuhattum, F. Reichel, P. Muller, A. Taubenberger, S. Girardo, A. Jacobi, and J. Guck, "Intelligent image-based deformation-assisted cell sorting with molecular specificity," *Nat Methods,* vol. 17, no. 6, pp. 595-599, Jun 2020

[19] G. Choi, R. Nouri, L. Zarzar, and W. Guan, "Microfluidic deformability-activated sorting of single particles," *Microsystems & Nanoengineering,* vol. 6, no. 1, pp. 1-9, 2020

[20] WHO, "World Malaria Report 2016," *World Malaria Report 2016,* pp. 1-255, 2016

[21] N. Kolluri, C. M. Klapperich, and M. Cabodi, "Towards lab-on-a-chip diagnostics for malaria elimination," *Lab Chip,* vol. 18, no. 1, pp. 75-94, Jan 7 2018

[22] M. Aingaran, R. Zhang, S. K. Law, Z. L. Peng, A. Undisz, E. Meyer, M. Diez-Silva, T. A. Burke, T. Spielmann, C. T. Lim, S. Suresh, M. Dao, and M. Marti, "TY Host cell deformability is linked to transmission in the human malaria parasite Plasmodium falciparum," *Cell Microbiol,* vol. 14, no. 7, pp. 983-993, Jul 2012

[23] C. P. Nixon, "Plasmodium falciparum gametocyte transit through the cutaneous microvasculature: A new target for malaria transmission blocking vaccines?," *Hum Vacc Immunother,* vol. 12, no. 12, pp. 3189-3195, 2016

[24] H. C. Slater, A. Ross, A. L. Ouedraogo, L. J. White, C. Nguon, P. G. T. Walker, P. Ngor, R. Aguas, S. P. Silal, A. M. Dondorp, P. La Barre, R. Burton, R. W. Sauerwein, C. Drakeley, T. A. Smith, T. Bousema, and A. C. Ghani, "Assessing the impact of next-generation rapid diagnostic tests on Plasmodium falciparum malaria elimination strategies," *Nature,* vol. 528, no. 7580, pp. S94-S101, Dec 3 2015

[25] C. Wongsrichanalai, M. J. Barcus, S. Muth, A. Sutamihardja, and W. H. Wernsdorfer, "A review of malaria diagnostic tools: Microscopy and rapid diagnostic test (RDT)," *American Journal of Tropical Medicine and Hygiene,* vol. 77, no. 6, pp. 119-127, Dec 2007

[26] A. Moody, "Rapid diagnostic tests for malaria parasites," *Clin Microbiol Rev,* vol. 15, no. 1, pp. 66-78, Jan 2002

[27] S. S. Modak, C. A. Barber, E. Geva, W. R. Abrams, D. Malamud, and Y. S. Ongagna, "Rapid Point-of-Care Isothermal Amplification Assay for the Detection of Malaria without Nucleic Acid Purification," *Infectious diseases,* vol. 9, pp. 1-9, 2016

[28] H. Hopkins, I. J. Gonzalez, S. D. Polley, P. Angutoko, J. Ategeka, C. Asiimwe, B. Agaba, D. J. Kyabayinze, C. J. Sutherland, M. D. Perkins, and D. Bell, "Highly Sensitive Detection of Malaria Parasitemia in a Malaria-Endemic Setting: Performance of a New Loop-Mediated Isothermal Amplification Kit in a Remote Clinic in Uganda," *J Infect Dis,* vol. 208, no. 4, pp. 645-652, Aug 15 2013

[29] B. Aydin-Schmidt, W. P. Xu, I. J. Gonzalez, S. D. Polley, D. Bell, D. Shakely, M. I. Msellem, A. Bjorkman, and A. Martensson, "Loop Mediated Isothermal Amplification (LAMP) Accurately Detects Malaria DNA from Filter Paper Blood Samples of Low Density Parasitaemias," *Plos One,* vol. 9, no. 8, p. e103905, Aug 8 2014

[30] T. Leslie, A. Mikhail, I. Mayan, M. Anwar, S. Bakhtash, M. Nader, C. Chandler, C. J. M. Whitty, and M. Rowland, "Overdiagnosis and mistreatment of malaria among febrile patients at primary healthcare level in Afghanistan: observational study," *Brit Med J,* vol. 345, p. e4389., Jul 24 2012

[31] L. Wu, L. L. van den Hoogen, H. Slater, P. G. T. Walker, A. C. Ghani, C. J. Drakeley, and L. C. Okell, "Comparison of diagnostics for the detection of asymptomatic Plasmodium falciparum infections to inform control and elimination strategies," *Nature,* vol. 528, no. 7580, pp. S86-S93, Dec 3 2015

[32] C. W. Pirnstill and G. L. Cote, "Malaria Diagnosis Using a Mobile Phone Polarized Microscope," *Sci Rep-Uk,* vol. 5, p. 13368, Aug 25 2015

[33] G. Snounou, S. Viriyakosol, X. P. Zhu, W. Jarra, L. Pinheiro, V. E. Dorosario, S. Thaithong, and K. N. Brown, "High-Sensitivity of Detection of Human Malaria Parasites by the Use of Nested Polymerase Chain-Reaction," *Mol Biochem Parasit,* vol. 61, no. 2, pp. 315-320, Oct 1993

[34] E. T. Han, R. Watanabe, J. Sattabongkot, B. Khuntirat, J. Sirichaisinthop, H. Iriko, L. Jin, S. Takeo, and T. Tsuboi, "Detection of four Plasmodium species by genus- and species-specific loop-mediated isothermal amplification for clinical diagnosis," *J Clin Microbiol,* vol. 45, no. 8, pp. 2521-8, Aug 2007

[35] V. Reddy, V. Ravi, A. Desai, M. Parida, A. M. Powers, and B. W. Johnson, "Utility of IgM ELISA, TaqMan real-time PCR, reverse transcription PCR, and RT-LAMP assay for the diagnosis of Chikungunya fever," *Journal of medical virology,* vol. 84, no. 11, pp. 1771-8, Nov 2012

[36] U. Morris, M. Khamis, B. Aydin-Schmidt, A. K. Abass, M. I. Msellem, M. H. Nassor, I. J. Gonzalez, A. Martensson, A. S. Ali, A. Bjorkman, and J. Cook, "Field deployment of loop-mediated isothermal amplification for centralized mass-screening of asymptomatic malaria in Zanzibar: a pre-elimination setting," *Malaria J,* vol. 14, pp. 1-6, May 17 2015

[37] B. Greenwood and T. Mutabingwa, "Malaria in 2002," *Nature,* vol. 415, no. 6872, pp. 670-672, Feb 7 2002

[38] S. Kersting, V. Rausch, F. F. Bier, and M. von Nickisch-Rosenegk, "Rapid detection of Plasmodium falciparum with isothermal recombinase polymerase amplification and lateral flow analysis," *Malaria J,* vol. 13, p. 99, Mar 15 2014

[39] M. S. Cordray and R. R. Richards-Kortum, "A paper and plastic device for the combined isothermal amplification and lateral flow detection of Plasmodium DNA," *Malaria J,* vol. 14, p. 472, Nov 26 2015

[40] Y. Li, N. Kumar, A. Gopalakrishnan, C. Ginocchio, R. Manji, M. Bythrow, B. Lemieux, and H. M. Kong, "Detection and Species Identification of Malaria Parasites by Isothermal, tHDA Amplification Directly from Human Blood without Sample Preparation," *J Mol Diagn,* vol. 15, no. 5, pp. 634-641, Sep 2013

[41] E. T. Han, R. Watanabe, J. Sattabongkot, B. Khuntirat, J. Sirichaisinthop, H. Iriko, L. Jin, S. Takeo, and T. Tsuboi, "Detection of four Plasmodium species by genus- and species-specific loop-mediated isothermal amplification for clinical diagnosis," *J Clin Microbiol,* vol. 45, no. 8, pp. 2521-2528, Aug 2007

[42] S. D. Polley, Y. Mori, J. Watson, M. D. Perkins, I. J. Gonzalez, T. Notomi, P. L. Chiodini, and C. J. Sutherland, "Mitochondrial DNA Targets Increase Sensitivity of Malaria

Detection Using Loop-Mediated Isothermal Amplification," *J Clin Microbiol,* vol. 48, no. 8, pp. 2866-2871, Aug 2010

[43] M. Safavieh, M. K. Kanakasabapathy, F. Tarlan, M. U. Ahmed, M. Zourob, W. Asghar, and H. Shafiee, "Emerging Loop-Mediated Isothermal Amplification-Based Microchip and Microdevice Technologies for Nucleic Acid Detection," *Acs Biomater-Sci Eng,* vol. 2, no. 3, pp. 278-294, Mar 2016

[44] E. C. Oriero, J. P. van Geertruyden, D. C. Nwakanma, U. D'Alessandro, and J. Jacobs, "Novel techniques and future directions in molecular diagnosis of malaria in resource-limited settings," *Expert Rev Mol Diagn,* vol. 15, no. 11, pp. 1419-1426, Nov 2 2015

[45] R. Abdul-Ghani, "Towards rapid genotyping of resistant malaria parasites: could loop-mediated isothermal amplification be the solution?," *Malar J,* vol. 13, p. 237, 2014

[46] K. Goyal, H. Kaur, A. Sehgal, and R. Sehgal, "RealAmp Loop-Mediated Isothermal Amplification as a Point-of-Care Test for Diagnosis of Malaria: Neither Too Close nor Too Far," *J Infect Dis,* vol. 211, no. 10, p. 1686, May 15 2015

[47] U. Morris, M. Khamis, B. Aydin-Schmidt, A. K. Abass, M. I. Msellem, M. H. Nassor, I. J. Gonzalez, A. Martensson, A. S. Ali, A. Bjorkman, and J. Cook, "Field deployment of loop-mediated isothermal amplification for centralized mass-screening of asymptomatic malaria in Zanzibar: a pre-elimination setting," *Malaria journal,* vol. 14, p. 205, 2015

[48] M. S. Hsiang, B. Greenhouse, and P. J. Rosenthal, "Point of care testing for malaria using LAMP, loop mediated isothermal amplification," *J Infect Dis,* vol. 210, no. 8, pp. 1167-9, Oct 15 2014

[49] J. C. Patel, N. W. Lucchi, P. Srivastava, J. T. Lin, R. Sug-Aram, S. Aruncharus, P. K. Bharti, M. M. Shukla, K. Congpuong, W. Satimai, N. Singh, V. Udhayakumar, and S. R. Meshnick, "Field evaluation of a real-time fluorescence loop-mediated isothermal amplification assay, RealAmp, for the diagnosis of malaria in Thailand and India," *J Infect Dis,* vol. 210, no. 8, pp. 1180-7, Oct 15 2014

[50] E. T. Han, "Loop-mediated isothermal amplification test for the molecular diagnosis of malaria," *Expert Rev Mol Diagn,* vol. 13, no. 2, pp. 205-18, Mar 2013

[51] R. Singh, D. Savargaonkar, R. Bhatt, and N. Valecha, "Rapid detection of Plasmodium vivax in saliva and blood using loop mediated isothermal amplification (LAMP) assay," *The Journal of infection,* vol. 67, no. 3, pp. 245-7, Sep 2013

[52] R. Surabattula, M. P. Vejandla, P. C. Mallepaddi, K. Faulstich, and R. Polavarapu, "Simple, rapid, inexpensive platform for the diagnosis of malaria by loop mediated isothermal amplification (LAMP)," *Experimental parasitology,* vol. 134, no. 3, pp. 333-40, Jul 2013

[53] J. Sirichaisinthop, S. Buates, R. Watanabe, E. T. Han, W. Suktawonjaroenpon, S. Krasaesub, S. Takeo, T. Tsuboi, and J. Sattabongkot, "Evaluation of loop-mediated isothermal amplification (LAMP) for malaria diagnosis in a field setting," *Am J Trop Med Hyg,* vol. 85, no. 4, pp. 594-6, Oct 2011

[54] J. Sattabongkot, T. Tsuboi, E. T. Han, S. Bantuchai, and S. Buates, "Loop-mediated isothermal amplification assay for rapid diagnosis of malaria infections in an area of endemicity in Thailand," *J Clin Microbiol,* vol. 52, no. 5, pp. 1471-7, May 2014

[55] N. Tomita, Y. Mori, H. Kanda, and T. Notomi, "Loop-mediated isothermal amplification (LAMP) of gene sequences and simple visual detection of products," *Nat Protoc,* vol. 3, no. 5, pp. 877-882, 2008

[56] M. Goto, E. Honda, A. Ogura, A. Nomoto, and K. I. Hanaki, "Colorimetric detection of loop-mediated isothermal amplification reaction by using hydroxy naphthol blue," *Biotechniques,* vol. 46, no. 3, pp. 167-172, Mar 2009

[57] T. Notomi, Y. Mori, N. Tomita, and H. Kanda, "Loop-mediated isothermal amplification (LAMP): principle, features, and future prospects," *J Microbiol,* vol. 53, no. 1, pp. 1-5, Jan 2015

[58] S. Britton, Q. Cheng, and J. S. McCarthy, "Novel molecular diagnostic tools for malaria elimination: a review of options from the point of view of high-throughput and applicability in resource limited settings," *Malaria J,* vol. 15, p. 88, Feb 16 2016

[59] J. Kim, M. Johnson, P. Hill, and B. K. Gale, "Microfluidic sample preparation: cell lysis and nucleic acid purification," *Integr Biol,* vol. 1, no. 10, pp. 574-586, 2009

[60] F. B. Myers, R. H. Henrikson, J. Bone, and L. P. Lee, "A Handheld Point-of-Care Genomic Diagnostic System," *Plos One,* vol. 8, no. 8, p. e70266, Aug 1 2013

[61] S. C. Liao, J. Peng, M. G. Mauk, S. Awasthi, J. Z. Song, H. Friedman, H. H. Bau, and C. C. Liu, "Smart cup: A minimally-instrumented, smartphone-based point-of-care molecular diagnostic device," *Sensor Actuat B-Chem,* vol. 229, pp. 232-238, Jun 28 2016

[62] C. C. Liu, M. G. Mauk, R. Hart, M. Bonizzoni, G. Y. Yan, and H. H. Bau, "A Low-Cost Microfluidic Chip for Rapid Genotyping of Malaria-Transmitting Mosquitoes," *Plos One,* vol. 7, no. 8, p. e42222, Aug 3 2012

[63] S. Choi, "Powering point-of-care diagnostic devices," *Biotechnol Adv,* vol. 34, no. 3, pp. 321-330, May 2016

[64] G. Abel, "Current status and future prospects of point-of-care testing around the globe," *Expert Rev Mol Diagn,* vol. 15, no. 7, pp. 853-855, Jul 2015

[65] W. E. Jung, J. Han, J. W. Choi, and C. H. Ahn, "Point-of-care testing (POCT) diagnostic systems using microfluidic lab-on-a-chip technologies," *Microelectron Eng,* vol. 132, pp. 46-57, Jan 25 2015

[66] K. Yang, H. Peretz-Soroka, Y. Liu, and F. Lin, "Novel developments in mobile sensing based on the integration of microfluidic devices and smartphones," *Lab Chip,* vol. 16, no. 6, pp. 943-958, 2016

[67] J. Hu, X. Y. Cui, Y. Gong, X. Y. Xu, B. Gao, T. Wen, T. J. Lu, and F. Xu, "Portable microfluidic and smartphone-based devices for monitoring of cardiovascular diseases at the point of care," *Biotechnol Adv,* vol. 34, no. 3, pp. 305-320, May-Jun 2016

[68] S. D. Polley, Y. Mori, J. Watson, M. D. Perkins, I. J. Gonzalez, T. Notomi, P. L. Chiodini, and C. J. Sutherland, "Mitochondrial DNA targets increase sensitivity of malaria detection using loop-mediated isothermal amplification," *J Clin Microbiol,* vol. 48, no. 8, pp. 2866-71, Aug 2010

[69] G. Choi, D. Song, S. Shrestha, J. Miao, L. Cui, and W. Guan, "A field-deployable mobile molecular diagnostic system for malaria at the point of need," *Lab Chip,* vol. 16, no. 22, pp. 4341-4349, Nov 1 2016

[70] S. Britton, Q. Cheng, M. J. Grigg, C. B. Poole, C. Pasay, T. William, K. Fornace, N. M. Anstey, C. J. Sutherland, C. Drakeley, and J. S. McCarthy, "Sensitive Detection of Plasmodium vivax Using a High-Throughput, Colourimetric Loop Mediated Isothermal Amplification (HtLAMP) Platform: A Potential Novel Tool for Malaria Elimination," *Plos Neglect Trop D,* vol. 10, no. 2, p. e0004443, Feb 2016

[71] T. Notomi, H. Okayama, H. Masubuchi, T. Yonekawa, K. Watanabe, N. Amino, and T. Hase, "Loop-mediated isothermal amplification of DNA," *Nucleic Acids Res,* vol. 28, no. 12, p. E63, Jun 15 2000

[72] H. W. Chen and W. M. Ching, "Evaluation of the stability of lyophilized loop-mediated isothermal amplification reagents for the detection of Coxiella burnetii," *Heliyon,* vol. 3, no. 10, p. e00415, Oct 2017

[73] K. Y. Lien, C. J. Liu, Y. C. Lin, P. L. Kuo, and G. B. Lee, "Extraction of genomic DNA and detection of single nucleotide polymorphism genotyping utilizing an integrated

magnetic bead-based microfluidic platform," *Microfluid Nanofluid,* vol. 6, no. 4, pp. 539-555, Apr 2009

[74] T. Notomi, H. Okayama, H. Masubuchi, T. Yonekawa, K. Watanabe, N. Amino, and T. Hase, "Loop-mediated isothermal amplification of DNA," *Nucleic Acids Res,* vol. 28, no. 12, pp. e63-e63, Jun 15 2000

[75] A. M. Foudeh, T. F. Didar, T. Veres, and M. Tabrizian, "Microfluidic designs and techniques using lab-on-a-chip devices for pathogen detection for point-of-care diagnostics," *Lab Chip,* vol. 12, no. 18, pp. 3249-3266, 2012

[76] M. A. Lee, C. H. Tan, L. T. Aw, C. S. Tang, M. Singh, S. H. Lee, H. P. Chia, and E. P. H. Yap, "Real-time fluorescence-based PCR for detection of malaria parasites," *J Clin Microbiol,* vol. 40, no. 11, pp. 4343-4345, Nov 2002

[77] G. L. Long and J. D. Winefordner, "Limit of detection. A closer look at the IUPAC definition," *Anal. Chem.,* vol. 55, no. 7, pp. 712A–724A, 1983

[78] WHO, "World Malaria Report 2017," pp. 1-196, 2017

[79] N. Kolluri, C. M. Klapperich, and M. Cabodi, "Towards lab-on-a-chip diagnostics for malaria elimination," *Lab on a chip,* vol. 18, pp. 75-94, Nov 10 2018

[80] H. Hopkins, I. J. Gonzalez, S. D. Polley, P. Angutoko, J. Ategeka, C. Asiimwe, B. Agaba, D. J. Kyabayinze, C. J. Sutherland, M. D. Perkins, and D. Bell, "Highly sensitive detection of malaria parasitemia in a malaria-endemic setting: performance of a new loop-mediated isothermal amplification kit in a remote clinic in Uganda," *J Infect Dis,* vol. 208, no. 4, pp. 645-52, Aug 15 2013

[81] C. Katevatis, A. Fan, and C. M. Klapperich, "Low concentration DNA extraction and recovery using a silica solid phase," *Plos One,* vol. 12, no. 5, p. e0176848, May 5 2017

[82] B. Moonen, J. M. Cohen, R. W. Snow, L. Slutsker, C. Drakeley, D. L. Smith, R. R. Abeyasinghe, M. H. Rodriguez, R. Maharaj, M. Tanner, and G. Targett, "Malaria Elimination 3 Operational strategies to achieve and maintain malaria elimination," *Lancet,* vol. 376, no. 9752, pp. 1592-1603, Nov 6 2010

[83] D. Bell, A. E. Fleurent, M. C. Hegg, J. D. Boomgard, and C. C. McConnico, "Development of new malaria diagnostics: matching performance and need," *Malar J,* vol. 15, no. 1, p. 406, Aug 11 2016

[84] M. L. Wilson, "Laboratory diagnosis of malaria: conventional and rapid diagnostic methods," *Arch Pathol Lab Med,* vol. 137, no. 6, pp. 805-11, Jun 2013

[85] M. S. Cordray and R. R. Richards-Kortum, "Emerging nucleic acid-based tests for point-of-care detection of malaria," *Am J Trop Med Hyg,* vol. 87, no. 2, pp. 223-230, Aug 2012

[86] N. W. Lucchi, M. Gaye, M. A. Diallo, I. F. Goldman, D. Ljolje, A. B. Deme, A. Badiane, Y. D. Ndiaye, J. W. Barnwell, V. Udhayakumar, and D. Ndiaye, "Evaluation of the Illumigene Malaria LAMP: A Robust Molecular Diagnostic Tool for Malaria Parasites," *Scientific reports,* vol. 6, p. 36808, Nov 9 2016

[87] M. A. Dineva, L. MahiLum-Tapay, and H. Lee, "Sample preparation: a challenge in the development of point-of-care nucleic acid-based assays for resource-limited settings," *The Analyst,* vol. 132, no. 12, pp. 1193-9, Dec 2007

[88] M. Sema, A. Alemu, A. G. Bayih, S. Getie, G. Getnet, D. Guelig, R. Burton, P. LaBarre, and D. R. Pillai, "Evaluation of non-instrumented nucleic acid amplification by loop-mediated isothermal amplification (NINA-LAMP) for the diagnosis of malaria in Northwest Ethiopia," *Malar J,* vol. 14, p. 44, 2015

[89] A. W. Martinez, S. T. Phillips, G. M. Whitesides, and E. Carrilho, "Diagnostics for the Developing World: Microfluidic Paper-Based Analytical Devices," *Anal Chem,* vol. 82, no. 1, pp. 3-10, Jan 1 2010

[90] L. X. Kong, K. Parate, K. Abi-Samra, and M. Madou, "Multifunctional wax valves for liquid handling and incubation on a microfluidic CD," *Microfluid Nanofluid,* vol. 18, no. 5-6, pp. 1031-1037, May 2015

[91] M. Madou, J. Zoval, G. Y. Jia, H. Kido, J. Kim, and N. Kim, "Lab on a CD," *Annual Review of Biomedical Engineering,* vol. 8, pp. 601-628, 2006

[92] J. M. Park, Y. K. Cho, B. S. Lee, J. G. Lee, and C. Ko, "Multifunctional microvalves control by optical illumination on nanoheaters and its application in centrifugal microfluidic devices," *Lab Chip,* vol. 7, no. 5, pp. 557-564, 2007

[93] R. Gorkin, J. Park, J. Siegrist, M. Amasia, B. S. Lee, J. M. Park, J. Kim, H. Kim, M. Madou, and Y. K. Cho, "Centrifugal microfluidics for biomedical applications," *Lab Chip,* vol. 10, no. 14, pp. 1758-1773, 2010

[94] R. Burger, P. Reith, V. Akujobi, and J. Ducree, "Rotationally controlled magneto-hydrodynamic particle handling for bead-based microfluidic assays," *Microfluid Nanofluid,* vol. 13, no. 4, pp. 675-681, Oct 2012

[95] L. C. Gao and T. J. McCarthy, "Contact angle hysteresis explained," *Langmuir,* vol. 22, no. 14, pp. 6234-6237, Jul 4 2006

[96] D. Oner and T. J. McCarthy, "Ultrahydrophobic surfaces. Effects of topography length scales on wettability," *Langmuir,* vol. 16, no. 20, pp. 7777-7782, Oct 3 2000

[97] T. H. Kim, J. Park, C. J. Kim, and Y. K. Cho, "Fully Integrated Lab-on-a-Disc for Nucleic Acid Analysis of Food-Borne Pathogens," *Analytical chemistry,* vol. 86, no. 8, pp. 3841-3848, Apr 15 2014

[98] L. X. Kong, A. Perebikovsky, J. Moebius, L. Kulinsky, and M. Madou, "Lab-on-a-CD: A Fully Integrated Molecular Diagnostic System," *Jala-J Lab Autom,* vol. 21, no. 3, pp. 323-355, Jun 2016

[99] L. Dormond, K. Jaton, S. de Valliere, B. Genton, and G. Greub, "Malaria real-time PCR: correlation with clinical presentation," *New Microbes New Infect,* vol. 5, pp. 10-2, May 2015

[100] W. C. Lee, H. Shi, Z. Y. Poon, L. M. Nyan, T. Kaushik, G. V. Shivashankar, J. K. Y. Chan, C. T. Lim, J. Han, and K. J. Van Vliet, "Multivariate biophysical markers predictive of mesenchymal stromal cell multipotency," *P Natl Acad Sci USA,* vol. 111, no. 42, pp. E4409-E4418, Oct 21 2014

[101] D. Di Carlo, "A Mechanical Biomarker of Cell State in Medicine," *Jala-J Lab Autom,* vol. 17, no. 1, pp. 32-42, Feb 2012

[102] D. H. Kim, P. K. Wong, J. Park, A. Levchenko, and Y. Sun, "Microengineered Platforms for Cell Mechanobiology," *Annu Rev Biomed Eng,* vol. 11, pp. 203-233, 2009

[103] M. Musielak, "Red blood cell-deformability measurement: Review of techniques," *Clin Hemorheol Micro,* vol. 42, no. 1, pp. 47-64, 2009

[104] E. M. Darling and D. Di Carlo, "High-Throughput Assessment of Cellular Mechanical Properties," *Annu Rev Biomed Eng,* vol. 17, pp. 35-62, 2015

[105] W. W. Xu, R. Mezencev, B. Kim, L. J. Wang, J. McDonald, and T. Sulchek, "Cell Stiffness Is a Biomarker of the Metastatic Potential of Ovarian Cancer Cells," *Plos One,* vol. 7, no. 10, p. e46609, Oct 4 2012

[106] J. D. Pajerowski, K. N. Dahl, F. L. Zhong, P. J. Sammak, and D. E. Discher, "Physical plasticity of the nucleus in stem cell differentiation," *P Natl Acad Sci USA,* vol. 104, no. 40, pp. 15619-15624, Oct 2 2007

[107] I. Sraj, C. D. Eggleton, R. Jimenez, E. Hoover, J. Squier, J. Chichester, and D. W. M. Marr, "Cell deformation cytometry using diode-bar optical stretchers," *J Biomed Opt,* vol. 15, no. 4, p. 047010, Jul-Aug 2010

[108] S. E. Cross, Y. S. Jin, J. Rao, and J. K. Gimzewski, "Nanomechanical analysis of cells from cancer patients," *Nat. Nanotechnol.,* vol. 2, no. 12, pp. 780-783, Dec 2007

[109] J. Guck, S. Schinkinger, B. Lincoln, F. Wottawah, S. Ebert, M. Romeyke, D. Lenz, H. M. Erickson, R. Ananthakrishnan, D. Mitchell, J. Kas, S. Ulvick, and C. Bilby, "Optical deformability as an inherent cell marker for testing malignant transformation and metastatic competence," *Biophys. J.,* vol. 88, no. 5, pp. 3689-3698, May 2005

[110] A. E. Bianco, F. L. Battye, and G. V. Brown, "Plasmodium-Falciparum - Rapid Quantification of Parasitemia in Fixed Malaria Cultures by Flow-Cytometry," *Experimental parasitology,* vol. 62, no. 2, pp. 275-282, Oct 1986

[111] T. F. Kong, W. J. Ye, W. K. Peng, H. W. Hou, Marcos, P. R. Preiser, N. T. Nguyen, and J. Han, "Enhancing malaria diagnosis through microfluidic cell enrichment and magnetic resonance relaxometry detection," *Sci Rep-Uk,* vol. 5, Jun 17 2015

[112] W. R. Prescott, R. G. Jordan, M. P. Grobusch, V. M. Chinchilli, I. Kleinschmidt, J. Borovsky, M. Plaskow, M. Torrez, M. Mico, and C. Schwabe, "Performance of a malaria microscopy image analysis slide reading device," *Malar J,* vol. 11, p. 155, May 06 2012

[113] A. K. Bei, T. M. DeSimone, A. S. Badiane, A. D. Ahouidi, T. Dieye, D. Ndiaye, O. Sarr, O. Ndir, S. Mboup, and M. T. Duraisingh, "A flow cytometry-based assay for measuring invasion of red blood cells by Plasmodium falciparum," *Am J Hematol,* vol. 85, no. 4, pp. 234-237, Apr 2010

[114] H. W. Hou, A. A. S. Bhagat, A. G. L. Chong, P. Mao, K. S. W. Tan, J. Y. Han, and C. T. Lim, "Deformability based cell margination-A simple microfluidic design for malaria-infected erythrocyte separation," *Lab Chip,* vol. 10, no. 19, pp. 2605-2613, 2010

[115] D. R. Gossett, H. T. K. Tse, S. A. Lee, Y. Ying, A. G. Lindgren, O. O. Yang, J. Y. Rao, A. T. Clark, and D. Di Carlo, "Hydrodynamic stretching of single cells for large population mechanical phenotyping," *Proceedings of the National Academy of Sciences of the United States of America,* vol. 109, no. 20, pp. 7630-7635, May 15 2012

[116] O. Otto, P. Rosendahl, A. Mietke, S. Golfier, C. Herold, D. Klaue, S. Girardo, S. Pagliara, A. Ekpenyong, A. Jacobi, M. Wobus, N. Topfner, U. F. Keyser, J. Mansfeld, E. Fischer-Friedrich, and J. Guck, "Real-time deformability cytometry: on-the-fly cell mechanical phenotyping," *Nature Methods,* vol. 12, no. 3, pp. 199-+, Mar 2015

[117] V. Faustino, D. Pinho, T. Yaginuma, R. C. Calhelha, I. C. F. R. Ferreira, and R. Lima, "Extensional flow-based microfluidic device: deformability assessment of red blood cells in contact with tumor cells," *Biochip J,* vol. 8, no. 1, pp. 42-47, Mar 20 2014

[118] Y. Zheng, E. Shojaei-Baghini, A. Azad, C. Wang, and Y. Sun, "High-throughput biophysical measurement of human red blood cells," *Lab Chip,* vol. 12, no. 14, pp. 2560-2567, 2012

[119] E. Du, S. Ha, M. Diez-Silva, M. Dao, S. Suresh, and A. P. Chandrakasan, "Electric impedance microflow cytometry for characterization of cell disease states," *Lab Chip,* vol. 13, no. 19, pp. 3903-3909, 2013

[120] Q. Guo, S. J. Reiling, P. Rohrbach, and H. S. Ma, "Microfluidic biomechanical assay for red blood cells parasitized by Plasmodium falciparum," *Lab Chip,* vol. 12, no. 6, pp. 1143-1150, 2012

[121] W. J. Zhang, K. Kai, D. S. Choi, T. Iwamoto, Y. H. Nguyen, H. L. Wong, M. D. Landis, N. T. Ueno, J. Chang, and L. D. Qin, "Microfluidics separation reveals the stem-cell-like deformability of tumor-initiating cells," *P Natl Acad Sci USA,* vol. 109, no. 46, pp. 18707-18712, Nov 13 2012

[122] M. J. Rosenbluth, W. A. Lam, and D. A. Fletcher, "Analyzing cell mechanics in hematologic diseases with microfluidic biophysical flow cytometry," *Lab Chip,* vol. 8, no. 7, pp. 1062-1070, 2008

[123] J. S. Dudani, D. R. Gossett, H. T. K. Tse, and D. Di Carlo, "Pinched-flow hydrodynamic stretching of single-cells," *Lab Chip,* vol. 13, no. 18, pp. 3728-3734, 2013

[124] P. Rosendahl, K. Plak, A. Jacobi, M. Kraeter, N. Toepfner, O. Otto, C. Herold, M. Winzi, M. Herbig, Y. Ge, S. Girardo, K. Wagner, B. Baum, and J. Guck, "Real-time fluorescence and deformability cytometry," *Nat Methods,* vol. 15, no. 5, pp. 355-358, May 2018

[125] Y. X. Deng, S. P. Davis, F. Yang, K. S. Paulsen, M. Kumar, R. S. DeVaux, X. H. Wang, D. S. Conklin, A. Oberai, J. I. Herschkowitz, and A. J. Chung, "Inertial Microfluidic Cell Stretcher (iMCS): Fully Automated, High-Throughput, and Near Real-Time Cell Mechanotyping," *Small,* vol. 13, no. 28, p. 1700705, Jul 26 2017

[126] S. Byun, S. Son, D. Amodei, N. Cermak, J. Shaw, J. H. Kang, V. C. Hecht, M. M. Winslow, T. Jacks, P. Mallick, and S. R. Manalis, "Characterizing deformability and surface friction of cancer cells," *Proc Natl Acad Sci U S A,* vol. 110, no. 19, pp. 7580-5, May 7 2013

[127] X. Yang, Z. Chen, J. Miao, L. Cui, and W. Guan, "High-throughput and label-free parasitemia quantification and stage differentiation for malaria-infected red blood cells," *Biosensors & bioelectronics,* vol. 98, pp. 408-414, Dec 15 2017

[128] H. W. Hou, Q. Li, G. Lee, A. Kumar, C. Ong, and C. T. Lim, "Deformability study of breast cancer cells using microfluidics," *Biomed Microdevices,* vol. 11, no. 3, pp. 557-564, 2009

[129] K. D. Nyberg, M. B. Scott, S. L. Bruce, A. B. Gopinath, D. Bikos, T. G. Mason, J. W. Kim, H. S. Choi, and A. C. Rowat, "The physical origins of transit time measurements for rapid, single cell mechanotyping," *Lab Chip,* vol. 16, no. 17, pp. 3330-3339, 2016

[130] A. F. Cowman and B. S. Crabb, "Invasion of red blood cells by malaria parasites," *Cell,* vol. 124, no. 4, pp. 755-766, Feb 24 2006

[131] J. Bradley, W. Stone, D. F. Da, I. Morlais, A. Dicko, A. Cohuet, W. M. Guelbeogo, A. Mahamar, S. Nsango, H. M. Soumare, H. Diawara, K. Lanke, W. Graumans, R. Siebelink-Stoter, M. van de Vegte-Bolmer, I. Chen, A. Tiono, B. P. Goncalves, R. Gosling, R. W. Sauerwein, C. Drakeley, T. S. Churcher, and T. Bousema, "Predicting the likelihood and intensity of mosquito infection from sex specific Plasmodium falciparum gametocyte density," *Elife,* vol. 7, May 31 2018

[132] L. Grignard, B. P. Goncalves, A. M. Early, R. F. Daniels, A. B. Tiono, W. M. Guelbeogo, A. Ouedraogo, E. M. van Veen, K. Lanke, A. Diarra, I. Nebie, S. B. Sirima, G. A. Targett, S. K. Volkman, D. E. Neafsey, D. F. Wirth, T. Bousema, and C. Drakeley, "Transmission of molecularly undetectable circulating parasite clones leads to high infection complexity in mosquitoes post feeding," *Int J Parasitol,* vol. 48, no. 8, pp. 671-677, Jul 2018

[133] N. B. Henry, S. S. Serme, G. Siciliano, S. Sombie, A. Diarra, N. Sagnon, A. S. Traore, S. B. Sirima, I. Soulama, and P. Alano, "Biology of Plasmodium falciparum gametocyte sex ratio and implications in malaria parasite transmission," *Malar J,* vol. 18, no. 1, p. 70, Mar 12 2019

[134] M. Tibúrcio, M. Niang, G. Deplaine, S. Perrot, E. Bischoff, P. A. Ndour, F. Silvestrini, A. Khattab, G. Milon, and P. H. David, "A switch in infected erythrocyte deformability at the maturation and blood circulation of Plasmodium falciparum transmission stages," *Blood, The Journal of the American Society of Hematology,* vol. 119, no. 24, pp. e172-e180, 2012

[135] M. Aingaran, R. Zhang, S. K. Law, Z. Peng, A. Undisz, E. Meyer, M. Diez‐Silva, T. A. Burke, T. Spielmann, and C. T. Lim, "Host cell deformability is linked to transmission in the human malaria parasite Plasmodium falciparum," *Cell Microbiol,* vol. 14, no. 7, pp. 983-993, 2012

[136] M. Yamada, M. Nakashima, and M. Seki, "Pinched flow fractionation: Continuous size separation of particles utilizing a laminar flow profile in a pinched microchannel," *Anal Chem,* vol. 76, no. 18, pp. 5465-5471, Sep 15 2004

[137] M. Podenphant, N. Ashley, K. Koprowska, K. U. Mir, M. Zalkovskij, B. Bilenberg, W. Bodmer, A. Kristensen, and R. Marie, "Separation of cancer cells from white blood cells by pinched flow fractionation," *Lab Chip,* vol. 15, no. 24, pp. 4598-4606, 2015

[138] H. Wang, Z. Z. Liu, D. M. Shin, Z. G. Chen, Y. Cho, Y. J. Kim, and A. Han, "A continuous-flow acoustofluidic cytometer for single-cell mechanotyping," *Lab Chip,* vol. 19, no. 3, pp. 387-393, Feb 7 2019

[139] J. McGrath, M. Jimenez, and H. Bridle, "Deterministic lateral displacement for particle separation: a review," *Lab Chip,* vol. 14, no. 21, pp. 4139-4158, 2014

[140] Z. Liu, Y. Lee, J. Jang, Y. Li, X. Han, K. Yokoi, M. Ferrari, L. Zhou, and L. Qin, "Microfluidic cytometric analysis of cancer cell transportability and invasiveness," *Scientific Report,* vol. 5, p. 14272, Sep 25 2015

[141] X. N. Yang, Z. F. Chen, J. Miao, L. W. Cui, and W. H. Guan, "High-throughput and label-free parasitemia quantification and stage differentiation for malaria-infected red blood cells," *Biosensors & bioelectronics,* vol. 98, pp. 408-414, Dec 15 2017

[142] Y. Zheng, J. Nguyen, C. Wang, and Y. Sun, "Electrical measurement of red blood cell deformability on a microfluidic device," *Lab Chip,* vol. 13, no. 16, pp. 3275-3283, 2013

[143] A. Adamo, A. Sharei, L. Adamo, B. Lee, S. Mao, and K. F. Jensen, "Microfluidics-Based Assessment of Cell Deformability," *Anal. Chem.,* vol. 84, no. 15, pp. 6438-6443, Aug 7 2012

[144] Y. Zhou, D. H. Yang, Y. N. Zhou, B. L. Khoo, J. Han, and Y. Ai, "Characterizing Deformability and Electrical Impedance of Cancer Cells in a Microfluidic Device," *Anal. Chem.,* vol. 90, no. 1, pp. 912-919, Jan 2 2018

[145] C. W. Shields, C. D. Reyes, and G. P. Lopez, "Microfluidic cell sorting: a review of the advances in the separation of cells from debulking to rare cell isolation," *Lab Chip,* vol. 15, no. 5, pp. 1230-1249, 2015

[146] C. H. Chen, S. H. Cho, F. Tsai, A. Erten, and Y. H. Lo, "Microfluidic cell sorter with integrated piezoelectric actuator," *Biomed Microdevices,* vol. 11, no. 6, pp. 1223-1231, Dec 2009

[147] J. Seo and L. P. Lee, "Effects on wettability by surfactant accumulation/depletion in bulk polydimethylsiloxane (PDMS)," *Sensors and Actuators. B: Chemical,* vol. 119, no. 1, pp. 192-198, Nov 24 2006

[148] V. Doyeux, T. Podgorski, S. Peponas, M. Ismail, and G. Coupier, "Spheres in the vicinity of a bifurcation: elucidating the Zweifach-Fung effect," *J Fluid Mech,* vol. 674, pp. 359-388, May 2011

[149] K. D. Nyberg, K. H. Hu, S. H. Kleinman, D. B. Khismatullin, M. J. Butte, and A. C. Rowat, "Quantitative Deformability Cytometry: Rapid, Calibrated Measurements of Cell Mechanical Properties," *Biophysical Journal,* vol. 113, no. 7, pp. 1574-1584, Oct 2017

[150] F. R. Kersey, T. J. Merkel, J. L. Perry, M. E. Napier, and J. M. DeSimone, "Effect of Aspect Ratio and Deformability on Nanoparticle Extravasation through Nanopores," *Langmuir,* vol. 28, no. 23, pp. 8773-8781, Jun 12 2012

[151] P. J. Flory, *Principles of polymer chemistry* (The George Fisher Baker non-resident lectureship in chemistry at Cornell University). Ithaca,: Cornell Univ. Press, 1953, p. 672.

[152] T. J. Merkel, S. W. Jones, K. P. Herlihy, F. R. Kersey, A. R. Shields, M. Napier, J. C. Luft, H. L. Wu, W. C. Zamboni, A. Z. Wang, J. E. Bear, and J. M. DeSimone, "Using mechanobiological mimicry of red blood cells to extend circulation times of hydrogel microparticles," *P Natl Acad Sci USA,* vol. 108, no. 2, pp. 586-591, Jan 11 2011

[153] S. L. N. Maas, J. de Vrij, E. J. van der Vlist, B. Geragousian, L. van Bloois, E. Mastrobattista, R. M. Schiffelers, M. H. M. Wauben, M. L. D. Broekman, and E. N. M. Nolte-'t Hoen, "Possibilities and limitations of current technologies for quantification of biological extracellular vesicles and synthetic mimics," *J Control Release,* vol. 200, pp. 87-96, Feb 28 2015

[154] R. M. M. Smeets, U. F. Keyser, N. H. Dekker, and C. Dekker, "Noise in solid-state nanopores," *Proceedings of the National Academy of Sciences of the United States of America,* vol. 105, no. 2, pp. 417-421, Jan 15 2008

[155] A. V. Jagtiani, J. Carletta, and J. Zhe, "A microfluidic multichannel resistive pulse sensor using frequency division multiplexing for high throughput counting of micro particles," *Journal of Micromechanics and Microengineering,* vol. 21, no. 6, p. 065004, 2011/04/21 2011

[156] R. Liu, N. Wang, F. Kamili, and A. F. Sarioglu, "Microfluidic CODES: a scalable multiplexed electronic sensor for orthogonal detection of particles in microfluidic channels," *Lab Chip,* vol. 16, no. 8, pp. 1350-1357, Apr 21 2016

[157] L. H. Ozarow, S. Shamai, and A. D. Wyner, "Information-Theoretic Considerations for Cellular Mobile Radio," *Ieee T Veh Technol,* vol. 43, no. 2, pp. 359-378, May 1994

[158] R. W. Deblois and C. P. Bean, "Counting and Sizing of Submicron Particles by the Resistive Pulse Technique," *Rev Sci Instrum,* vol. 41, no. 7, pp. 909-916, 1970

[159] E. C. Gregg and K. D. Steidley, "Electrical Counting and Sizing of Mammalian Cells in Suspension," *Biophys. J.,* vol. 5, no. 4, pp. 393-405, 1965

[160] A. Meller and D. Branton, "Single molecule measurements of DNA transport through a nanopore," *Electrophoresis,* vol. 23, no. 16, pp. 2583-2591, 2002

[161] Y. Zheng, J. Nguyen, C. Wang, and Y. Sun, "Electrical measurement of red blood cell deformability on a microfluidic device," *Lab Chip,* vol. 13, no. 16, pp. 3275-83, Aug 21 2013

[162] R. H. Cole, S. Y. Tang, C. A. Siltanen, P. Shahi, J. Q. Zhang, S. Poust, Z. J. Gartner, and A. R. Abate, "Printed droplet microfluidics for on demand dispensing of picoliter droplets and cells," *Proc Natl Acad Sci U S A,* vol. 114, no. 33, pp. 8728-8733, Aug 15 2017

[163] R. Ramji, M. Wang, A. A. S. Bhagat, D. Tan Shao Weng, N. V. Thakor, C. Teck Lim, and C.-H. Chen, "Single cell kinase signaling assay using pinched flow coupled droplet microfluidics," *Biomicrofluidics,* vol. 8, no. 3, p. 034104, 2014

[164] Y. Deng, S. P. Davis, F. Yang, K. S. Paulsen, M. Kumar, R. Sinnott DeVaux, X. Wang, D. S. Conklin, A. Oberai, J. I. Herschkowitz, and A. J. Chung, "Inertial Microfluidic Cell Stretcher (iMCS): Fully Automated, High-Throughput, and Near Real-Time Cell Mechanotyping," *Small,* vol. 13, no. 28, Jul 2017

VITA

Gihoon Choi

Education

- Ph.D. candidate in Electrical Engineering
  The Pennsylvania State University, University Park, Pennsylvania, USA
- Master in Electrical and Computer Engineering
  The State University of New York at Binghamton, Binghamton, USA
- Bachelor in Electrical Engineering
  The State University of New York at Binghamton, Binghamton, USA

Selected Journal Publication (6 of 12)

- **G. Choi**, R. Nouri, L. Zarzar, and W. Guan, "Microfluidic Deformability Activated Sorting of Single Particles," Microsystems & Nanoengineering, 6, 11, 2020
- Z. Tang, **G. Choi**, R. Nouri, and W. Guan, "Nanopore digital counting of LAMP amplicons for nucleic acid testing," Nano Letters, 19 (11), pp. 7927-7934, 2019
- **G. Choi**, E. Murphy, and W. Guan, "Microfluidic time-division multiplexing accessing (TDMA) resistive pulse sensor for particle analysis," ACS Sensors, 4, pp. 1957-1963, 2019
- W. Zhang, Y. Hu, **G. Choi**, S. Lang, M. Liu, and W. Guan, "Microfluidic multiple cross-correlated Coulter counter for improved particle size analysis," Sensors and Actuators B: Chemical, 296, 126615, 2019
- **G. Choi**, T. Prince, J. Miao, L. Cui, and W. Guan, "Sample-to-answer palm-sized nucleic acid testing device towards low-cost malaria mass screening," Biosensors and Bioelectronics, 115, 83, 2018
- **G. Choi**, D. Song, S. Shrestha, J. Miao, L. Cui, and W. Guan, "A field-deployable mobile molecular diagnostic system for malaria at the point of need," Lab Chip, 16, pp. 4341, 2016

Selected Conference Presentation (3 of 11)

- **G. Choi**, E. Murphy, and W. Guan, "Time-division multiplexed resistive pulse sensor on a microfluidic chip," IEEE Sensors, Oct. 27-30, 2019, Montreal, Canada
- **G. Choi**, R. Nouri, and W. Guan, "Microfluidic Deformability-activated Cell Sorting (DACS). BMES Annual Meeting," Oct. 16-19, 2019, Philadelphia, USA
- **G. Choi** and W. Guan, "Non-centrifugal microfluidic nucleic acid testing on lab-on-a-disc," Transducers 2019, Jun. 23-27, 2019, Berlin, Germany (Outstanding Oral Paper Award Finalist)

Award

- Outstanding Paper Award Finalist in Oral Category (Transducers 2019)
- Outstanding MS Researcher Award (2015)